Title	Studies on Synthesis of Metal Nanoparticles by Ionic Liquid-Sputtering Method Aiming on Preparation of High-Performance Electrocatalyst
Author(s)	吉井, 一記
Citation	大阪大学, 2014, 博士論文
Version Type	VoR
URL	https://doi.org/10.18910/34424
rights	
Note	

Doctoral Dissertation

Studies on Synthesis of Metal Nanoparticles by Ionic Liquid-Sputtering Method Aiming on Preparation of High-Performance Electrocatalyst

Kazuki Yoshii

January 2014

Department of Applied Chemistry

Graduate School of Engineering

Osaka University

Preface

The studies presented in this thesis were carried out under the guidance of Professor Dr. Susumu Kuwabata at Department of Applied Chemistry, Graduate School of Engineering, Osaka University during 2009-2014.

The object of this thesis is to develop the novel preparation method of metal nanoparticles being usable as electrocatalyst by ionic liquid-sputtering method. Nanomaterials using ionic liquid have been gained much attention in the field of not only electrochemical science but also various scientific and industrial fields. The author hopes sincerely that the findings obtained in the studies would contribute to progress science and technology in the field of ionic liquid and nanomaterials.

Kazuki Yoshii

Kazuki Yoshii

Department of Applied Chemistry,

Graduate School of Engineering,

Osaka University

Suita, Osaka, Japan

March, 2014

Contents

General Introduction

Metal nanoparticles with small diameters have received great attention over past few decades because of their distinctive characteristics including large surface area, specific catalytic activities, and quantum size effect.[1–6] Especially, the catalytic activity of metal nanoparticles which depends on their particle size and shape has been widely investigated.[7–11] Au nanoparticles have been studied as an oxidation catalyst for carbon monoxide or alcohols.[12–15] It is also well known that Pt nanoparticles have the electrocatalytic activity toward alcohol oxidation and oxygen reduction reaction.[16–20] Although these are applied for various organic reactions and energy devices, the efficient utilization of these novel metals is strongly required due to the exhaustion of resources.

Metal nanoparticles can be prepared by two distinct ways, that is, by chemical synthesis in solution phase (wet process) or by subdivision of bulk metals with physical techniques (dry process).[10] In the case of the wet process, the reduction of the corresponding metal precursor is conducted by appropriate reducing agent in the presence of additional stabilizing agent. As a result, byproducts, unreacted materials and stabilizing agent remain in the prepared suspension. On the other hand, metal sputtering or gas phase processes are employed as a dry process for the synthesis of metal nanoparticles. Although the advantage of the dry process is the production of a large quantity of nanoparticles, the synthesis of isolated nanoparticles and their size control is very difficult to achieve.

Recently, metal nanoparticle preparations using room-temperature ionic liquids (RTILs) have been widely investigated as a novel strategy because it works not only as a reaction medium but also as a stabilizing agent, allowing homogeneous dispersion of the produced nanoparticles.[21–29] RTIL, which is a liquid salt at room-temperature, has been gained much attention in the various scientific and industrial fields, such as energy technology, surface finishing, organic and inorganic synthesis, gas separation and vacuum technologies.[30–41] Multiplicity of the RTIL-related science and technology should be due to the RTIL’s peculiar physicochemical properties including relatively high ionic conductivity, favorable thermal and chemical stability, wide electrochemical window, flame retardation, and extremely low vapor pressure. The potential of using RTILs as a solvent as well as a stabilizing agent for metal nanoparticle preparation is only recognized in the early 2000s.[42,43] Ir nanoparticles were prepared by chemical reduction method[42] and Ge nanoparticles were produced by electrochemical reduction method.[43] Just a few years later, various metal nanoparticles were prepared using RTILs. Furthermore, the extremely low vapor pressure of RTILs has made it possible to handle them under high vacuum condition such as X-ray photoemission[44] and electron microscope technology.[45–47] As a metal nanoparticle preparation strategy combined with RTIL and vacuum technology, Torimoto, Kuwabata, and their coworkers have reported that magnetron sputtering onto RTIL directly can produce metal nanoparticles highly dispersed in RTIL.[48] This method, which is called ionic liquid-sputtering method, has enabled the synthesis of a variety of metal or metal oxide nanoparticles.[49–65] It has been also reported that Au and Pt nanoparticles prepared by this method showed electrocatalytic activity toward oxygen reduction reaction.[51,53] However, rudimentary knowledge and application of ionic liquid-sputtering method are not enough and further advancement is expected.

The present work

The author studied the preparation of Pt and Au nanoparticles by ionic liquid-sputtering method. The effect of RTIL species on the size of the resulting nanoparticles was demonstrated. In addition, Pt nanoparticles prepared by this method was applied for the electrocatalyst by immobilizing them onto carbon substrate and their electrocatalytic activity and durability were investigated.

This thesis consists of three chapters as follows:

Chapter 1 deals with the preparation of Pt and Au nanoparticles by the ionic liquid-sputtering method. To reveal the effect of RTIL species on the size of the resulting nanoparticles, more than 20 kinds of RTILs including phosphonium cation-based RTIL were applied to prepare metal nanoparticles by this method. In the process, the physicochemical properties of novel tri-n-butylalkylphosphonium cation-based RTILs were also investigated.

Chapter 2 introduces the application of Pt nanoparticles prepared by this method to electrocatalyst for oxygen reduction reaction. It is found that Pt nanoparticles were easily immobilized on surfaces of glassy carbon plates and single-walled carbon nanotubes (SWCNTs) by heating treatment. The immobilization mechanism of Pt nanoparticles on SWCNT was revealed by the results of XPS analysis.

In chapter 3, the durability of the Pt-supported carbon material as the electrocatalyst, which was evaluated by the potential cycle test, is described. The electrocatalyst prepared using RTIL in this study showed higher durability compared with the commercially available Pt-supported carbon catalyst.

Chapter 1

Preparation of Pt and Au Nanoparticles by Ionic Liquid-Sputtering Method

1-1. Introduction

Various kinds of metal or metal oxide nanoparticles were prepared by ionic liquid-sputtering method so far.[49–65] But the used RTILs are limited to ammonium, pyrrolidinium, and imidazolium cation-based RTILs. The phosphonium cation is well known as one of the promising cation components in RTIL.[66,67] It should be a significant issue for improvement in value of this method to investigate whether phosphonium cation-based RTIL is applicable to the ionic liquid-sputtering method.

The advantage of phosphonium cation-based RTILs is that various phosphorus salts with ordinary anions are commercially available and are produced in large quantity.[67] Once phosphorus salts with halide anions such as Cl^- and Br^- showed a melting point above room temperature,[41] but now we can prepare many phosphonium cation-based RTILs by the combination with phosphonium cations and a wide variety of polyatomic anions, e.g., bis(trifluoromethylsulfonyl)amide ($[Tf_2N]^-$), tetrafluoroborate ($[BF_4]^-$), dicyanamide ($[N(CN)_2]^-$) and fluorohydrogenate ($[(FH)_nF]^-$ ($1 \leq n \leq 3$)).[66–81] This RTIL system also has interesting features like other RTIL systems. For example, the combination of tetra-*n*-butylphosphonium ($[P_{4,\ 4,\ 4,\ 4}]^+$) and amino acid-based anion generates chirality-induced RTILs,[70] and the mixture of tetra-*n*-butylphosphonium hydroxide and benzimidazole can produce both hydroxide ion and proton conductive RTILs by controlling the mixing ratio.[71] Some phosphonium cation-based RTILs can form an ionic plastic crystal phase that is expected to be a next generation electrolyte.[72,73]

A number of researches about metal nanoparticle preparation in various RTILs by reduction of metal precursors were conducted, so far.[21–28] In those cases, it was demonstrated that the size of metal nanoparticles are dependent of the volume of anion volume of RTIL.[82] On the other hand, the factors determining the size of nanoparticles in ionic liquid-sputtering method was investigated by few research groups.[60–62,64] Nishikawa *et al.* reported that temperature of metal target, applied voltage and temperature of the capture medium have strong influence to determine the size.[62] Dupont *et al.* reported that the size and size distribution of Au nanoparticles depend on various experimental parameters, such as the RTIL structural organization and in particular on the surface composition.[64]

In chapter 1, preparation of Pt and Au nanoparticles by ionic liquid-sputtering method using more than 20 kinds of RTILs including phosphonium cation-based RTIL has been demonstrated to unveil the effect of RTIL species on the size of the resulting nanoparticles. The obtained particle sizes were discussed from the viewpoints of their physicochemical properties. In the process, the physicochemical properties of novel tri-*n*-butylalkylphosphonium cation-based RTILs were also investigated.

1-2. Experimental section

1-2-1. Preparation of RTILs

N,*N*,*N*-trimethyl-*N*-propylammonium bis(trifluoromethanesulfonyl)amide ($[N_{1,1,1,3}][Tf_2N]$), *N*,*N*,*N*-triethyl-*N*-pentylammonium bis(trifluoromethanesulfonyl)amide ($[N_{2,2,2,5}][Tf_2N]$), *N*-methyl-*N*-propylpyrrolidinium bis(trifluoromethanesulfonyl)amide ($[Pyr_{1,3}][Tf_2N]$), *N*-butyl-*N*-methylpyrrolidinium bis(trifluoromethanesulfonyl)amide ($[Pyr_{1,4}][Tf_2N]$), 1-ethyl-3methylimidazolium bis(trifluoromethanesulfonyl)amide ($[C_1C_2Im][Tf_2N]$), 1-butyl-3methylimidazolium bis(trifluoromethanesulfonyl)amide ($[C_1C_4Im][Tf_2N]$), 1-allyl-3-ethylimidazolium bis(trifluoromethanesulfonyl)amide ($[C_2C_{allyl}Im][Tf_2N]$) and

1-butyl-3methylimidazolium hexafluorophosphate ($[C_1C_4Im][PF_6]$) were purchased from Kanto Chemical Co., Inc. 1-Butyl-3methylimidazolium trifluoromethanesulfonate ($[C_1C_4Im][TfO]$) was purchased from IoLiTec (Ionic Liquid Technologies GmbH & Co.) *N*-methyl-*N*-methoxymethylpyridinium bis(trifluoromethanesulfonyl)amide ($[Pyr_{1,1O1}][Tf_2N]$) was provided by Otsuka Chemical Co., Ltd. Tri-*n*-butylmethylphosphonium dimethylphosphate ($[P_{4,4,4,1}][DMP]$), tri-*n*-butyloctylphosphonium bis (trifluoromethylsulfonyl)amide ($[P_{4,4,4,8}][Tf_2N]$), tri-*n*-butyloctylphosphonium trifluoromethanesulfonate ($[P_{4,4,4,8}][TfO]$), tri-*n*-butyloctylphosphonium trifluoroacetate ($[P_{4,4,4,8}][CF_3COO]$), and tri-*n*-butyloctylphosphonium tosylate ($[P_{4,4,4,8}][TS]$) were provided by Prof. Katsuhiko Tsunashima at Department of Material Science, Wakayama National College of Technology.

N,*N*,*N*-tributyl-*N*-methylammonium bis(trifluoromethanesulfonyl)amide ($[N_{4,4,4,1}][Tf_2N]$), *N*-methyl-*N*-octylpyrrolidinium bis(trifluoromethanesulfonyl)amide ($[Pyr_{1,8}][Tf_2N]$), 1-hexyl-3methylimidazolium bis(trifluoromethanesulfonyl)amide ($[C_1C_6Im][Tf_2N]$), 1-methyl-3-octyllimidazolium bis(trifluoromethanesulfonyl)amide ($[C_1C_8Im][Tf_2N]$), 1-decyl-3methylimidazolium bis(trifluoromethanesulfonyl)amide ($[C_1C_{10}Im][Tf_2N]$), 1-dodecyl-3methylimidazolium bis(trifluoromethanesulfonyl)amide ($[C_1C_{12}Im][Tf_2N]$) , 1-hexyl-2,3-dimethylimidazolium bis(trifluoromethanesulfonyl)amide ($[C_6dimeIm][Tf_2N]$), 1-butyl-3methylimidazolium bis(perfluoroethanesulfonyl)amide ($[C_1C_4Im][BETI]$), tri-*n*-butyl(2-hydroxymethyl)phosphonium bis (trifluoromethylsulfonyl)amide ($[P_{4,4,4,2OH}][Tf_2N]$), tetra-*n*-butylphosphonium *O*,*O*′-diethylphosphorodithioate ($[P_{4,4,4,4}][DEPDT]$), and tri-*n*-butyldodecylphosphonium 3,4-bis(methoxycarbonyl)benzenesulfonate ($[P_{4,4,4,12}][MCBS]$) were prepared by two common synthetic processes. The first process is a straightforward quaternization between corresponding pyrrolidine, imidazole or phosphine and alkyl halide to synthesize a quaternary onium halide. The second process is an anion-exchange reaction between resulting onium halide and target anion. To be more specific, for example, $[P_{4,\ 4,\ 4,\ 2OH}][Tf_2N]$ was synthesized by the following procedures. The quaternization reaction between tri-*n*-butylphosphine (Nippon Chemical Industrial Co., Ltd., ultrapure grade) and 1-bromoethanol (Tokyo Chemical Industry Co., Ltd.) was carried out at 353 K under nitrogen atmosphere. Tri-*n*-butylphosphine was used as received. The obtained tri-*n*-butyl(2-hydroxymethyl)phosphonium bromide ($[P_{4,\ 4,\ 4,\ 2OH}]Br$) was rinsed with *n*-hexane to remove unreacted tri-*n*-butylphosphine and 1-bromoethanol. The $[P_{4,\ 4,\ 4,\ 2OH}]Br$ dried under vacuum and $Li[Tf_2N]$ were mixed thoroughly in ultrapure water at ambient temperature to yield the $[P_{4,\ 4,\ 4,\ 2OH}][Tf_2N]$ by the anion exchange reaction, and then the crude $[P_{4,\ 4,\ 4,\ 2OH}][Tf_2N]$ was extracted by toluene and purified by rinsing with ultrapure water several times until no residual bromide anion was detected with the use of 0.1 M $AgNO_3$ aqueous solution. $[C_1C_6Im][Tf_2N]$, $[C_1C_8Im][Tf_2N]$, $[C_1C_{10}Im][Tf_2N]$, $[C_1C_{12}Im][Tf_2N]$ $[C_6dimeIm][Tf_2N]$, $[P_{4,4,4,4}][DEPDT]$ and $[P_{4,4,4,12}][MCBS]$ were also prepared by the similar way previously described. In the case of $[N_{4,4,4,1}][Tf_2N]$ and $[C_1C_4Im][BETI]$, onium halides, i.e. *N*,*N*,*N*-tributyl-*N*-methylammonium chloride (>98.0%, Sigma-Aldrich) and 1-butyl-3methylimidazolium chloride (ultrapure grade, Kanto Chemical Co., Inc), were purchased and purified by recrystallization prior to use, followed by anion-exchange reaction as described above. All the RTILs employed in this study were dried at 373 K under vacuum condition (ca. 0.67 Pa) for 12 hrs and were stored in argon gas-filled glove box prior to their characterization and experiments. Water content of RTILs except for $[P_{4,\ 4,\ 4,\ 4}][DEPDT]$, determined by Karl-Fischer titration, was below 40 ppm. That of $[P_{4,\ 4,\ 4,\ 4}][DEPDT]$ could not be estimated due to an unexpected reaction with Karl-Fischer solution. Cation and anion structure used in this chapter is depicted in Figure 1-1.

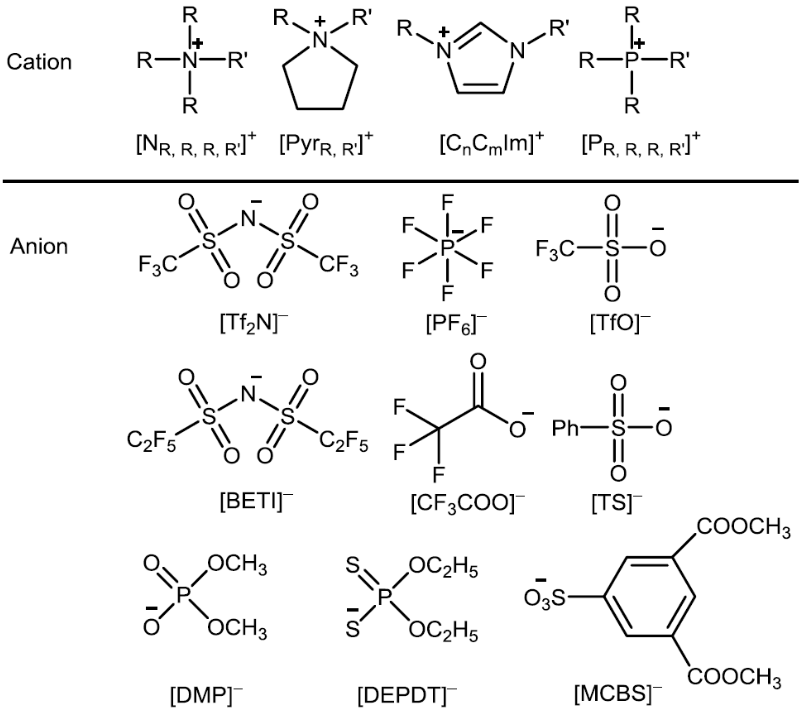

Figure1-1. Chemical structures of cation and anion components used in this study.

1-2-2. NMR Characterization and Elemental Analysis Data

NMR characterization and elemental analysis was conducted for four phosphonium cation-based RTILs as described below.

Tri-*n*-butylmethylphosphonium dimethylphosphate ([P$_{4,\ 4,\ 4,\ 1}$][DMP]), $(C_4H_9)_3(CH_3)P\text{-}PO_2(OCH_3)_2$; ^{1}H NMR (599.85 MHz in CDCl$_3$), δ 0.93-1.01 (t, 9H, $P^+CH_2(CH_2)_2C\mathit{H_3}$); 1.47-1.59 (m, 12H, $P^+CH_2(C\mathit{H_2})_2CH_3$); 2.04-2.10 (d, 3H, $P^+C\mathit{H_3}$); 2.34-2.44 (m, 6H, $P^+C\mathit{H_2}(CH_2)_2CH_3$); 3.54-3.61 (d, 6H, $PO_2(OC\mathit{H_3})_2^-$) ppm. ^{13}C NMR (150.85 MHz in CDCl$_3$), δ 3.9-4.4 (d, $P^+\mathit{C}H_3$); 13.37 (s, $P^+CH_2(CH_2)_2\mathit{C}H_3$); 19.4-19.9 (d, $P^+\mathit{C}H_2(CH_2)_2CH_3$); 23.4-23.9 (various d, $P^+CH_2(\mathit{C}H_2)_2CH_3$); 52.1-52.3 (d, $PO_2(O\mathit{C}H_3)_2^-$) ppm. ^{31}P NMR (242.82 MHz in CDCl$_3$), δ 2.02 (s, $\mathit{P}O_2(OCH_3)_2^-$); 31.81 (s, $(C_4H_9)_3(CH_3)\mathit{P}^+$) ppm. Elemental analysis calcd (%) for $C_{15}H_{36}O_4P_2$: C 52.62, H 10.60; found: C 52.47, H 11.06.

Tri-*n*-butyl(2-hydroxymethyl)phosphonium bis(trifluoromethylsulfonyl)amide ([P$_{4,\ 4,\ 4,}$

$_{2OH}$][Tf$_2$N]), $(C_4H_9)_3(C_2H_4OH)P\text{-}N(SO_2CF_3)_2$; ^{1}H NMR (599.85 MHz in CDCl$_3$), δ 0.92-1.00 (t, 9H, $P^+CH_2(CH_2)_2CH_3$); 1.45-1.57 (m, 12H, $P^+CH_2(CH_2)_2CH_3$); 2.13-2.19 (m, 6H, $P^+CH_2(CH_2)_2CH_3$); 2.39-2.45 (m, 2H, $P^+CH_2CH_2OH$); 3.27-3.33 (br, 1H, $P^+CH_2CH_2OH$); 3.97-4.05 (d, 2H, $P^+CH_2CH_2OH$) ppm. ^{13}C NMR (150.85 MHz in CDCl$_3$), δ 13.14 (s, $P^+CH_2(CH_2)_2CH_3$); 19.00-19.50 (various d, $P^+CH_2(CH_2)_2CH_3$, $P^+CH_2CH_2OH$); 55.40-55.55 (d, $P^+CH_2CH_2OH$); 119.74 (q, $N(SO_2CF_3)_2^-$) ppm. ^{19}F (564.40 MHz in CDCl$_3$), δ −80.48 (s, $N(SO_2CF_3)_2^-$) ppm. ^{31}P NMR (242.82 MHz in CDCl$_3$), δ 33.02 (s, $P^+CH_2(CH_2)_2CH_3$) ppm. Elemental analysis calcd (%) for $C_{16}H_{32}F_6NO_5PS_2$: C 36.43, H 6.11, N 2.66; found: C 36.63, H 6.25, N 2.66.

Tetra-*n*-butylphosphonium *O,O'*-diethylphosphorodithioate ([P$_{4,\ 4,\ 4,\ 4}$][DEPDT]), $(C_4H_9)_4P\text{-}PS_2(OC_2H_5)_2$; ^{1}H NMR (599.85 MHz in CDCl$_3$), δ 0.96-1.01 (t, 9H, $P^+CH_2(CH_2)_2CH_3$); 1.26-1.31 (t, 6H, $PS_2(OCH_2CH_3)_2^-$); 1.53-1.60 (m, 16H, $P^+CH_2(CH_2)_2CH_3$); 2.41-2.48 (m, 8H, $P^+CH_2(CH_2)_2CH_3$); 4.03-4.09 (m, 4H, $PS_2(OCH_2CH_3)_2^-$) ppm. ^{13}C NMR (150.85 MHz in CDCl$_3$), δ 13.45 (s, $P^+CH_2(CH_2)_2CH_3$); 16.17-16.30 (d, $P^+CH_2(CH_2)_2CH_3$); 18.77-19.33 (d, $PS_2(OCH_2CH_3)_2^-$); 23.74-24.03 (m, $P^+CH_2(CH_2)_2CH_3$); 60.97-61.14 (d, $PS_2(OCH_2CH_3)_2^-$) ppm. ^{31}P NMR (242.82 MHz in CDCl$_3$), δ 32.41 (s, $(C_4H_9)_4P^+$); 112.29 (s, $PS_2(OCH_2CH_3)_2^-$) ppm. Elemental analysis calcd (%) for $C_{20}H_{46}O_2P_2S_2$: C 54.02, H 10.43; found: C 53.93, H 10.53.

Tri-*n*-butyldodecylphosphonium 3,4-bis(methoxycarbonyl)benzenesulfonate ([P$_{4,\ 4,\ 4,\ 12}$][MCBS]), $(C_4H_9)_3(C_{12}H_{25})P\text{-}C_6H_3(COOCH_3)_2(SO_3)$; ^{1}H NMR (599.85 MHz in CDCl$_3$), δ 0.86-0.90 (t, 3H, $P^+CH_2CH_2(CH_2)_8CH_2CH_3$); 0.92-0.99 (t, 9H, $P^+CH_2(CH_2)_2CH_3$); 1.21-1.33 (m, 16H, $P^+CH_2CH_2(CH_2)_8CH_2CH_3$); 1.40-1.58 (m, 16H, $P^+CH_2CH_2(CH_2)_8CH_2CH_3$, $P^+CH_2(CH_2)_2CH_3$); 2.25-2.37 (m, 8H, $P^+CH_2CH_2(CH_2)_8CH_2CH_3$, $P^+CH_2(CH_2)_2CH_3$); 3.92 (s, 6H, $C_6H_3(COOCH_3)_2(SO_3)^-$); 8.65 (s, 1H, $C_6H_3(COOCH_3)_2(SO_3)^-$); 8.76 (s, 2H, $C_6H_3(COOCH_3)_2(SO_3)^-$) ppm. ^{13}C NMR (150.85 MHz in CDCl$_3$), δ 13.37 (s, $P^+CH_2(CH_2)_2CH_3$); 14.06 (s, $P^+CH_2CH_2(CH_2)_8CH_2CH_3$); 18.43-19.11 (various d,

$\mathrm{P^{+}}\mathit{C}\mathrm{H_2(CH_2)_2CH_3}$, $\mathrm{P^{+}}\mathit{C}\mathrm{H_2CH_2(CH_2)_8CH_2CH_3}$); 21.65-24.11, 28.82-31.94 (various s, d, $\mathrm{P^{+}CH_2(}\mathit{C}\mathrm{H_2)_2CH_3}$, $\mathrm{P^{+}CH_2}\mathit{C}\mathrm{H_2(}\mathit{C}\mathrm{H_2)_8}\mathit{C}\mathrm{H_2CH_3}$); 52.17 (s, $\mathrm{C_6H_3(COO}\mathit{C}\mathrm{H_3)_2(SO_3)^{-}}$); 130.34, 131.13, 131.55 148.18 (s, $\mathit{C_6}\mathrm{H_3(COOCH_3)_2(SO_3)^{-}}$); 165.86 (s, $\mathrm{C_6H_3(}\mathit{C}\mathrm{OOCH_3)_2(SO_3)^{-}}$) ppm. ^{31}P NMR (242.82 MHz in $CDCl_3$), δ 32.64 (s, $\mathrm{(C_4H_9)_3(C_{12}H_{25})}\mathit{P}$) ppm. Elemental analysis calcd (%) for $C_{34}H_{61}O_7PS$: C 63.32, H 9.53; found: C 63.30, H 9.54.

1-2-3. Measurements of Physicochemical Properties

Thermogravimetry-differential thermal analysis (TG-DTA) was performed by a Bruker TG-DTA2000SA under nitrogen atmosphere at 10 K $\mathrm{min^{-1}}$. Differential scanning calorimetry (DSC) was conducted using a Bruker DSC 3100SA at 5 K $\mathrm{min^{-1}}$. These instruments were controlled with a Bruker MTC1000SA workstation utilizing a Bruker WS5003 software. Aluminum pan without and with aluminum top for TG-DTA and DSC, respectively, were employed, and the specimens for the thermal analysis were prepared in an argon gas-filled grove box (Vacuum Atmosphere Company NEXUS II system, H_2O and O_2 < 1 ppm). Density measurement was carried out with a 5 mL Pyrex® glass pycnometer that was calibrated by ultrapure water. Viscosity was measured with a Brookfield LVDV-II+ Pro programmable viscometer. The cone spindle was CPE-42 or CPE-52. Conductivity measurement was performed by a Horiba DS-51 digital conductivity meter with a glass conductivity cell after the cell calibration with 0.1 M KCl aqueous solution. All the analyses were conducted in an argon gas-filled grove box or by using air-tight cell to avoid contamination derived from the air.

1-2-4. Preparation of Pt and Au Nanoparticles

The soda glass (2.5 cm × 2.5 cm), on which RTIL (0.4 mL) was spread, was put in a Cressington108 auto SE sputter coater. A polycrystalline Pt or Au plate target (ϕ 5.7 cm, 99.98%) was placed on 4.5 cm above the glass plate. Sputter deposition onto RTIL was conducted with sputter current of 40 mA for 900 s in dry Ar (99.999%) atmosphere whose pressure did not exceed 7 ± 1 Pa. The sputtering was carried out by direct current (DC) mode at room temperature (298 ± 2 K).

1-2-5. Characterization of Pt and Au Nanoparticles

Particle sizes of Pt and Au nanoparticle were estimated by Hitachi H-7650 transmission electron microscope (TEM) operated at 100 kV. Before the TEM observation, the sample grid was prepared by dropping 5 μl of sputtered-RTIL onto a TEM grid (ø3.0 mm, copper, 400 mesh) and washing with acetonitrile.

1-3. Results and discussion

1-3-1. Physicochemical Properties of Tri-n-butylalkylphosphonium Cation-Based Room-Temperature Ionic Liquids

Four types of novel tri-*n*-butylalkylphosphonium-based RTILs studied in this section, [$P_{4, 4, 4, 1}$][DMP], [$P_{4, 4, 4, 2OH}$][Tf_2N], [$P_{4, 4, 4, 4}$][DEPDT] and [$P_{4, 4, 4, 12}$][MCBS], exhibited a liquid state at room temperature (293 K). I was able to handle them under open-air condition without any trouble although the RTILs slightly absorbed water derived from the air. [$P_{4, 4, 4, 2OH}$][Tf_2N], [$P_{4, 4, 4, 4}$][DEPDT] and [$P_{4, 4, 4, 12}$][MCBS] formed biphase with water like most phosphonium cation-based RTILs reported so far, but [$P_{4, 4, 4, 1}$][DMP] had a water-miscible nature. It is well-known that organic phosphorus salt, which consists of symmetric cation and halide anion, shows a melting point above room temperature, e.g., [$P_{4, 4, 4, 4}$]Br melts at 375.15 K.[83] But, the melting point of [$P_{4, 4, 4, 4}$][DEPDT] was greatly reduced due to the asymmetric structure and the large ion volume of the [DEPDT]$^-$. It suggests that the [DEPDT]$^-$ is a useful anion for RTILs with highly symmetric cation species.

Thermogravimetry-differential thermal analysis (TG-DTA) curves for the tri-*n*-butylalkylphosphonium-based RTILs under a nitrogen atmosphere are shown in Figure

1-2 and their thermal decomposition temperature determined at 5 and 10 % weight loss are given in Table 1-1 with the data on other phosphonium cation-based RTILs. Each RTIL investigated in this section showed a desirable thermal stability over 560 K. It is interesting to note that [$P_{4,4,4,12}$][MCBS] exhibited a fairly-high thermal stability among the phosphonium cation-based RTILs reported to date.[66–81] Usually phosphonium cation-based RTILs tend to indicate a good thermal stability relative to the ammonium cation-based ones with similar side chains.[75,76] The degradation pathway of phosphonium-based RTILs seems to be affected by anionic species rather than cationic one. While [$P_{4,4,4,2OH}$][Tf_2N] and [$P_{4,4,4,12}$][MCBS] showed a simple single-step degradation in Figure 1-2, the degradation for [$P_{4,4,4,1}$][DMP] and [$P_{4,4,4,4}$][DEPDT] proceeded by two steps. This two-step degradation behavior is consistent with a previous report on phosphonium cation-based RTILs with thermally-unstable anions.[69] Long-term thermal stability of RTIL that is an important parameter for high temperature applications is predicable from common TG data if the measurement condition is the same, i.e., RTIL with higher decomposition temperature usually shows a better long-term thermal stability.[84,85]

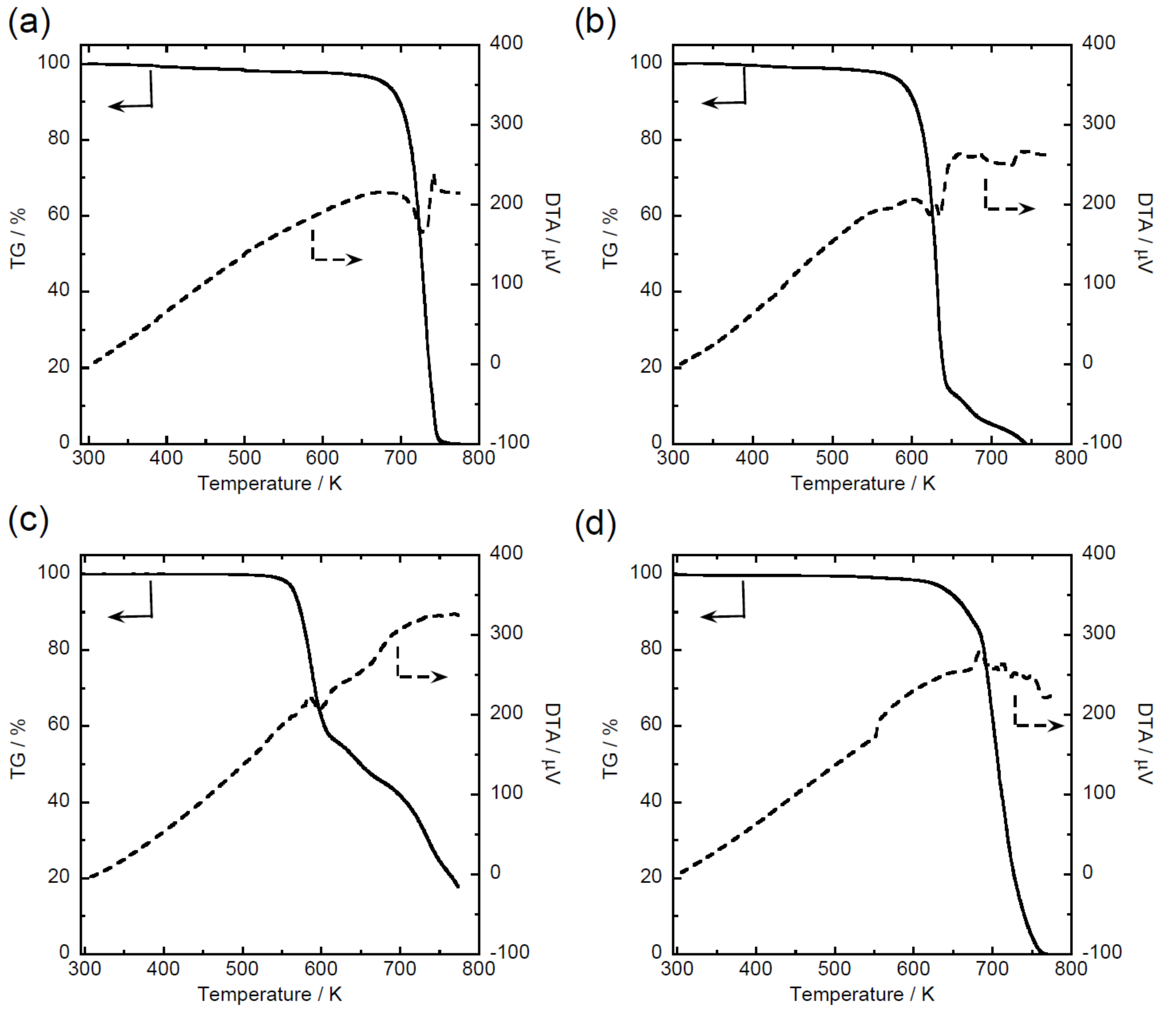

Figure 1-2. Results of thermogravimetry-differential thermal analysis measurement of the tri-*n*-butylalkylphosphonium cation-based RTILs. The samples were (a) [P$_{4,\ 4,\ 4,\ 1}$][DMP]; (b) [P$_{4,\ 4,\ 4,\ 2OH}$][Tf$_2$N]; (c) [P$_{4,\ 4,\ 4,\ 4}$][DEPDT]; (d) [P$_{4,\ 4,\ 4,\ 12}$][MCBS]. The measurements were conducted at 10 K min^{-1}.

Table 1-1. Physical and thermal properties of the tri-*n*-butylalkylphosphonium cation-based RTILs

RTILs	FW[a]	T_g[b] (K)	T_m[b] (K)	T_{dec}[c] (K)	ρ[d] (g cm^{-3})	η[e] (cP)	σ[f] (mS cm^{-1})	Ref.
$[P_{4,4,4,1}][Tf_2N]$	497.5	193	290	652	1.27	207	0.42	74
$[P_{4,4,4,1}][(CN)_2N]$	283.4	*[g]	279	651	0.96	167	1.2	77
$[P_{4,4,4,1}][(FH)_{2.3}F]$	282.3	169	249	*[g]	0.97	36	6.0	81
$[P_{4,4,4,1}][DMP]$	342.4	202	——	583, 562[h]	1.03[i]	439	0.18[i]	This work
$[P_{4,4,4,2OH}][Tf_2N]$	527.5	196	——	668, 646[h]	1.26[i]	242	0.48[i]	This work
$[P_{4,4,4,4}][(FH)_{2.3}F]$	324.4	——	239, 255	*[g]	0.95	47	3.7	81
$[P_{4,4,4,4}][DEPDT]$	444.7	206	——	574, 566[h]	1.01[i]	1107	0.083[i]	This work
$[P_{4,4,4,8}][Tf_2N]$	595.7	183	——	646	1.18	250	0.27	74
$[P_{4,4,4,8}][BF_4]$	402.3	191	——	672	1.02	1240	0.069	74
$[P_{4,4,4,8}][PF_6]$	460.5	*[g]	293	636	1.12	1720	0.047	74
$[P_{4,4,4,8}][OTf]$	464.7	193	——	681	1.08	778	0.087	74
$[P_{4,4,4,8}][CF_3COO]$	428.6	192	——	467	1.03	453	0.13	74
$[P_{4,4,4,8}][SCN]$	373.6	184	——	651	0.95	450	0.18	74
$[P_{4,4,4,8}][Tosyl]$	486.7	209	——	617	1.02	2435	0.021	74
$[P_{4,4,4,8}][(CN)_2N]$	381.6	180	——	653	0.95	245	0.45	77
$[P_{4,4,4,8}][(FH)_{2.3}F]$	380.6	174	——	*[g]	0.93	74	1.5	81
$[P_{4,4,4,12}][Tf_2N]$	651.8	187	284	656	1.13	303	0.18	74
$[P_{4,4,4,12}][BF_4]$	458.5	190	293	664	0.97	1310	0.047	74
$[P_{4,4,4,12}][MCBS]$	644.9	210	——	698, 678[h]	1.05[i]	16401	0.0042[i]	This work
$[P_{4,4,4,allyl}][Tf_2N]$	523.6	*[g]	302	692	1.26[i]	138[i]	0.64	78

a) Formula weight. b) Glass-transition or melting temperature. c) Thermal decomposition temperature at 10 % weight loss. d) Density at 298 K. e) Viscosity at 298 K. f) Conductivity at 298 K. g) No data. h) Thermal decomposition temperature at 10 % weight loss. i) The data were obtained at 303 K.

Differential scanning calorimetry (DSC) curves for the tri-*n*-butylalkylphosphonium-based RTILs are exhibited in Figure 1-3. All the RTILs could keep a liquid state over a wide range of temperature. [$P_{4,4,4,1}$][DMP] indicated a peculiar thermal phase transition behavior(Figure 1-3(a)). The crystallization was observed at 246 K after the glass transition at 202 K during the heating process from 173 K, and two endothermic peaks appeared at 279 and 290 K. These endothermic peaks should be assigned to solid-solid phase transition (279 K) and to melting (290 K). It is well-known that some RTILs have an ionic plastic crystal phase if both the cation and the anion in RTIL have spherical three-dimensional structure or similar configuration.[72,73,80,86–88] Several phosphonium cation-based RTILs also have such an ionic plastic crystal phase.[72,73,80] Timmermans proposed that the phase transition to the plastic crystal phase occurs by a low entropy change of fusion ($\Delta S_{fus} < 20$ J K^{-1} mol^{-1}).[89] In regard to the [$P_{4,4,4,1}$][DMP], the entropy changes (ΔS) of the endothermic peaks were 11.0 J K^{-1} mol^{-1} (enthalpy change, $\Delta H = 3077$ J mol^{-1}) and 17.7 J K^{-1} mol^{-1} ($\Delta H = 5135$ J mol^{-1}) at 279 K and 290 K, respectively. These results suggest that the plastic crystal phase exists within a range of 279 ~ 290 K. Analogous ionic plastic crystal phase in a narrow temperature range has already been reported.[90–92] [$P_{4,4,4,1}$][DMP] should be considered as a new example of RTIL with the plastic crystal phase. As to other three RTILs, [$P_{4,4,4,2OH}$][Tf_2N], [$P_{4,4,4,4}$][DEPDT] and [$P_{4,4,4,12}$][MCBS], only glass transition point appeared at 196, 206 and 210 K, respectively, during the heating process (Figure 1-3(b), (c) and (d)). Although [$P_{4,4,4,4}$][DEPDT] is composed of the cation having more spherical structure than the [$P_{4,4,4,1}$]$^+$ and the characteristic anion similar to [DMP]$^-$, ionic plastic crystal phase did not appear.

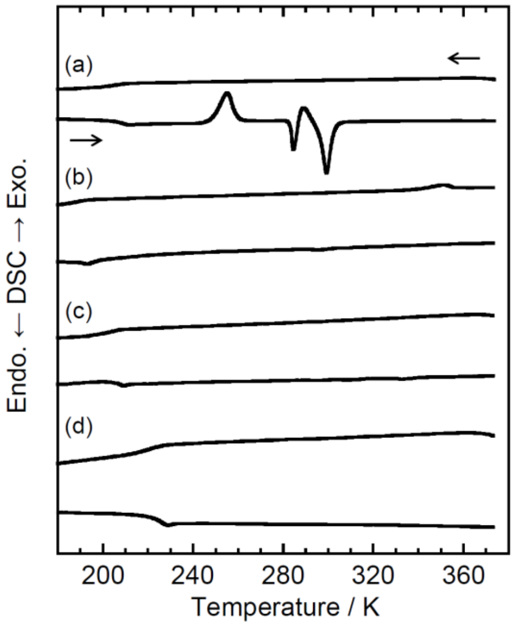

Figure 1-3. Differential scanning calorimetry curves of the tri-*n*-butylalkylphosphonium cation-based RTILs. The samples were (a) [$P_{4,\,4,\,4,\,1}$][DMP]; (b) [$P_{4,\,4,\,4,\,2OH}$][Tf_2N]; (c) [$P_{4,\,4,\,4,\,4}$][DEPDT]; (d) [$P_{4,\,4,\,4,\,12}$][MCBS]. The measurements were conducted at 5 K min^{-1}.

Figure 1-4 shows temperature dependence of the density, ρ (g cm^{-3}), of the tri-*n*-butylalkylphosphonium cation-based RTILs. A linear dependence with absolute temperature was obtained for all the RTILs. The density is expressed as a function of temperature:

$$\rho = a + bT \qquad (1)$$

where a, b and T are a density at 0 K (g cm^{-3}), a coefficient of volume expansion (g cm^{-3} K^{-1}), and an absolute temperature (K), respectively. The parameters fitted by the method of least squares are summarized in Table 1-2 along with the correlation coefficient, |*R*|, for the fitting. The density decreased in the following order: [$P_{4,\,4,\,4,\,2OH}$][Tf_2N], [$P_{4,\,4,\,4,\,12}$][MCBS], [$P_{4,\,4,\,4,\,1}$][DMP] and [$P_{4,\,4,\,4,\,4}$][DEPDT]. Optimized ionic volumes of the tri-*n*-butylalkylphosphonium cation-based RTILs calculated with B3LYP/6-31G+(d) level using Gaussian 09 program were 574.7 Å^3 ([$P_{4,\,4,\,4,\,2OH}$][Tf_2N]), 800.5 Å^3 ([$P_{4,\,4,\,4,\,12}$][MCBS]), 607.2 Å^3 ([$P_{4, 4, 4, 1}$][DMP]) and 487.1 Å^3 ([$P_{4, 4, 4, 4}$][DEPDT]).[93] These values were estimated from sum of the individually-calculated cation and anion volumes. It is reported that ionic volume in RTIL has a close relationship with physicochemical properties, which can be understood by lattice and solvation energies,[94,95] and provides useful information for prediction of physical properties, e.g., viscosity, conductivity and density.[96] With regard to the 1,3-dialkylimidazolium cation-based RTILs, the density ordinarily decreases with increasing their alkyl chain length. However, [$P_{4, 4, 4, 1}$][DMP] and [$P_{4, 4, 4, 4}$][DEPDT] showed smaller density values than [$P_{4, 4, 4, 12}$][MCBS] in spite of their smaller ionic volume. This result implies that the density for the RTILs is determined by both the volume of the ionic species and the local structure in RTIL that is provoked by electrostatic interaction and intermolecular electron repulsion.

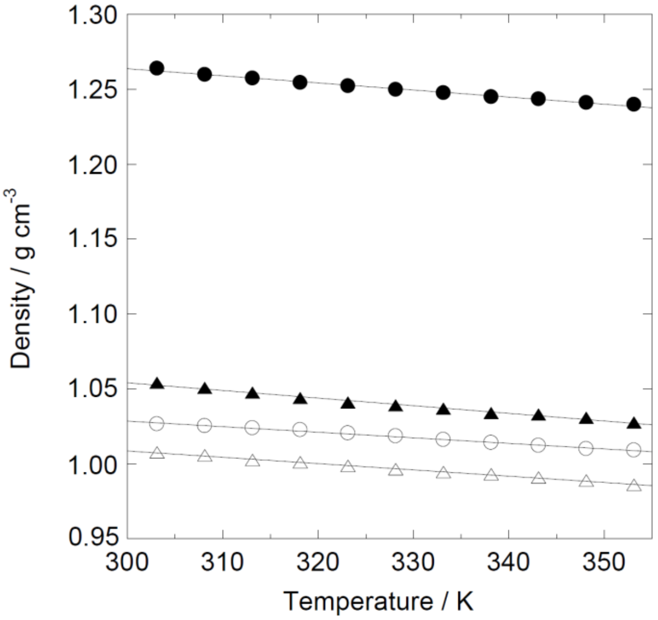

Figure 1-4. Temperature dependence of density of the tri-*n*-butylalkylphosphonium cation-based RTILs: (○) [$P_{4, 4, 4, 1}$][DMP]; (●) [$P_{4, 4, 4, 2OH}$][Tf_2N]; (△) [$P_{4, 4, 4, 4}$][DEPDT]; (▲) [$P_{4, 4, 4, 12}$][MCBS].

Table 1-2. Fitted parameters for the density of the tri-*n*-butylalkylphosphonium cation-based RTILs

RTILs	a (g cm^{-3})	b (g cm^{-3} K^{-1})	|R|
[$P_{4, 4, 4, 1}$][DMP]	1.14	-3.62×10^{-4}	0.9967
[$P_{4, 4, 4, 2OH}$][Tf_2N]	1.41	-4.74×10^{-4}	0.9947
[$P_{4, 4, 4, 4}$][DEPDT]	1.14	-4.24×10^{-4}	0.9985
[$P_{4, 4, 4, 12}$][MCBS]	1.21	-5.09×10^{-4}	0.9936

Temperature dependence of the absolute viscosity, η (cP (= mPa s)), for the four RTILs are indicated in Figure 1-5. [$P_{4, 4, 4, 12}$][MCBS] was a very viscous liquid (16401 cP s at 298 K) compared to other three RTILs. Given that several complexes with anion similar to the $[MCBS]^-$ can form three-dimensional framework structure through the hydrogen bonding among the ions,[97,98] there is a high possibility that analogous framework structure is formed in the [$P_{4, 4, 4, 12}$][MCBS]. The structure may cause the drastic increase of the viscosity. Arrhenius plots of each viscosity indicated in Figure 1-5 are convex downward curves. It is a typical behavior of the glass-forming RTIL. In this case, the plots can be fitted in the Vogel-Tamman-Fulcher (VTF) equation as expressed below and enable further useful investigation:[99]

$$\ln \eta = \frac{k_\eta}{T - T_0} + \frac{1}{2} \ln T - \ln A_\eta \qquad (2)$$

where k_η (K) is a constant related to Arrhenius activation energy for the viscous behavior, T_0 (K) is an ideal glass transition temperature, and A_η is a scaling factor. The fitted parameters are summarized in Table 1-3 along with the correlation coefficient, $|R|$.

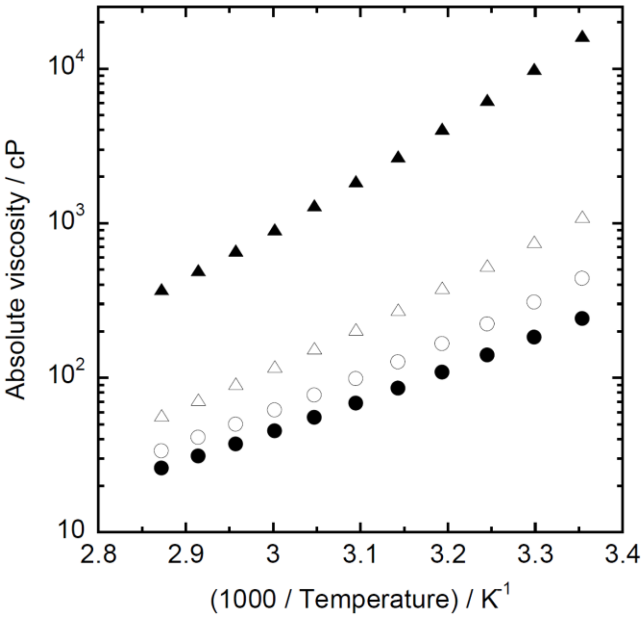

Figure 1-5. Arrhenius plots of absolute viscosity of the tri-*n*-butylalkylphosphonium cation-based RTILs: (○) [$P_{4, 4, 4, 1}$][DMP]; (●) [$P_{4, 4, 4, 2OH}$][Tf_2N]; (△) [$P_{4, 4, 4, 4}$][DEPDT]; (▲) [$P_{4, 4, 4, 12}$][MCBS].

Figure 1-6 shows temperature dependence of the ionic conductivity, σ (mS cm^{-1}), for the tri-*n*-butylalkylphosphonium-based RTILs. Generally ionic conductivity of RTIL depends on its absolute viscosity, because ion mobility is restricted by the viscosity. Arrhenius-type plots of the ionic conductivity exhibited a usual behavior; that is, the plots in each RTIL are convex upward curves and the values decreases with decreasing the temperature. As given in Table 1-1, the [$P_{4, 4, 4, 2OH}$][Tf_2N] showed a relatively-high conductivity among the RTILs consisting of tri-*n*-butylalkylphosphonium cation and fluoroanion except fluorohydrogenate anion because of the combination of appropriate cationic volume and flexible [Tf_2N]$^-$ anion. Interestingly the conductivity of the [$P_{4, 4, 4, 4}$][DEPDT] was about twice as much as that of the [$P_{4, 4, 4, 12}$][BF_4] having similar viscosity and molecular weight.[74] The experimental data of the ionic conductivity were converted to the equivalent conductivity, Λ (S cm^2 mol^{-1}), by using a following equation in order to fit the plot by the VTF equation and to discuss the activation energy of the equivalent conductivity.

$$\Lambda = \sigma M/\rho \qquad (3)$$

where M is a formula weight of phosphonium-based RTILs. The obtained values of Λ were fitted by Equation (4):

$$\ln \Lambda = -\frac{k_\Lambda}{T - T_0} - \frac{1}{2}\ln T + \ln A_\Lambda \qquad (4)$$

where k_Λ (K) is a constant related to Arrhenius activation energy for the conduction behavior, T_0 (K) is an ideal glass transition temperature, A_Λ is a scaling factor. The fitted parameters are summarized in Table 1-3 along with the correlation coefficient. The temperature-dependence activation energies for the absolute viscosity, $E_{a,\eta}$, and equivalent conductivity, $E_{a,\Lambda}$, can be calculated from the equation obtained by the partial differentiation on Equation (2) and (4) with respect to T as expressed below:[100,101]

$$E_{a,\eta} = -RT^2\left(\frac{\partial \ln \eta}{\partial T}\right) = \frac{Rk_\eta T^2}{(T - T_0)^2} - \frac{RT}{2} \qquad (5)$$

$$E_{a,\Lambda} = RT^2\left(\frac{\partial \ln \Lambda}{\partial T}\right) = \frac{Rk_\Lambda T^2}{(T - T_0)^2} - \frac{RT}{2} \qquad (6)$$

The resulting plots of $E_{a,\eta}$ and $E_{a,\Lambda}$ versus temperature are given in Figure 1-7. As other RTIL systems, those activation energies decreased with increasing temperature, and most values for the $E_{a,\eta}$ was larger than the $E_{a,\Lambda}$ at the same temperature.[102–104] However the differences between $E_{a,\eta}$ and $E_{a,\Lambda}$ were obviously larger than those for common RTILs especially at lower temperatures. Of the four tri-*n*-butylalkylphosphonium-based RTILs, [$P_{4,4,4,12}$][MCBS] exhibited the largest difference, suggesting that it has a unique ion-conductive mechanism. In fact, the framework structure that can contribute to effective ion conduction seems to be in the [$P_{4,4,4,12}$][MCBS] as already described in the discussion on the viscosity. The ion conduction would be controlled with the viscosity as well as the anomalous local structure in the tri-*n*-butylalkylphosphonium-based RTILs.

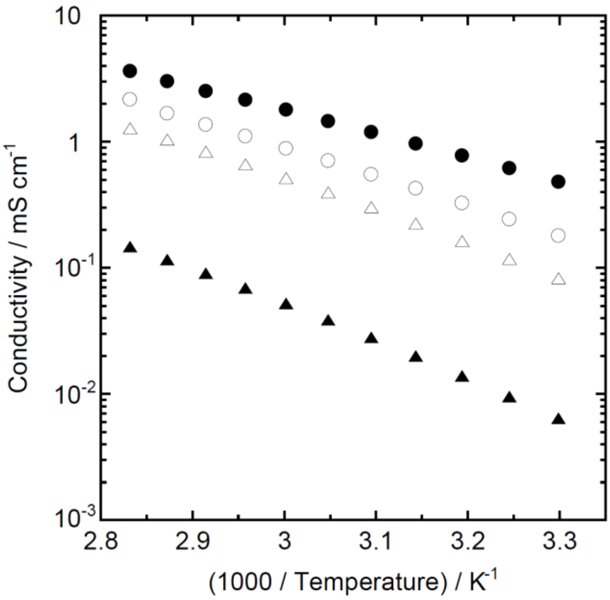

Figure 1-6. Arrhenius plots of conductivity of the tri-*n*-butylalkylphosphonium cation-based RTILs: (○) [$P_{4,\ 4,\ 4,\ 1}$][DMP]; (●) [$P_{4,\ 4,\ 4,\ 2OH}$][Tf_2N]; (△) [$P_{4,\ 4,\ 4,\ 4}$][DEPDT]; (▲) [$P_{4,\ 4,\ 4,\ 12}$][MCBS].

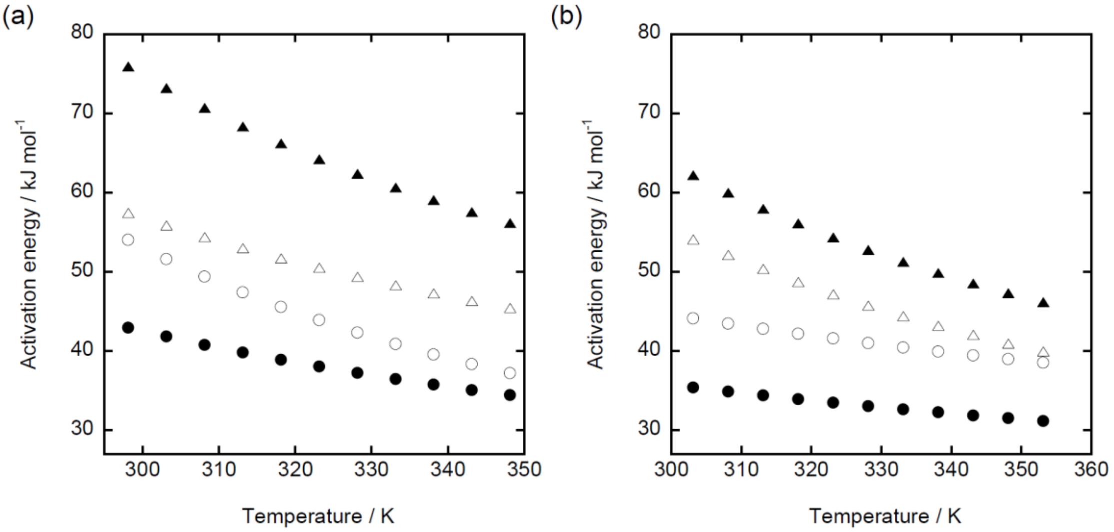

Figure 1-7. Temperature-dependence activation energies for (a) the absolute viscosity and (b) the equivalent conductivity for the tri-*n*-butylalkylphosphonium cation-based RTILs: (○) [$P_{4,\ 4,\ 4,\ 1}$][DMP]; (●) [$P_{4,\ 4,\ 4,\ 2OH}$][Tf_2N]; (△) [$P_{4,\ 4,\ 4,\ 4}$][DEPDT]; (▲) [$P_{4,\ 4,\ 4,\ 12}$][MCBS].

Table 1-3. Fitted parameters for the VTF equation of absolute viscosity and equivalent conductivity for the tri-*n*-butylalkylphosphonium cation-based RTILs

RTILs	Absolute viscosity (cP (= mPa s))				Equivalent conductivity (S $cm^2 mol^{-1}$)			
	T_0 / K	K_η / K	Ln A_η	|R|	T_0 / K	K_η / K	Ln A_η	|R|
$[P_{4, 4, 4, 1}]$[DMP]	171	1.19×10^3	6.10	0.9999	96	2.55×10^3	6.63	0.9998
$[P_{4, 4, 4, 2OH}][Tf_2N]$	129	1.71×10^3	7.46	0.9999	90	2.18×10^3	5.79	0.9999
$[P_{4, 4, 4, 4}]$[DEPDT]	124	2.29×10^3	9.00	0.9999	159	1.51×10^3	4.28	0.9999
$[P_{4, 4, 4, 12}]$[MCBS]	156	2.11×10^3	7.98	0.9999	158	1.75×10^3	3.66	0.9999

In order to investigate the correlation between conductivity and viscosity rigorously, I examined the dissociation behavior in the RTILs. It is able to be estimated in two ways. One is a recent analytical technique using a pulsed-field-gradient spin-echo (PGSE) NMR,[105] and another is a classical Walden plot method constructed from fluidic properties of RTIL, i.e., equivalent conductivity (S cm^2 mol^{-1}) and fluidity (reciprocal of absolute viscosity (cP^{-1}))[106]. Here I used the latter approach. In this approach, diluted KCl aqueous solution is regarded as an ideal dissociation state.[106] From the difference of Walden plots between the diluted KCl aqueous solution and RTIL, I can estimate the dissociation degree and speculate the ion conduction behavior in the RTILs. Also, I may apply "hole theory" to our physical data in order to discuss them more precisely.[107] But in this study, I employed the ideal KCl line to simplify the estimation and the speculation. Walden plot of the tri-*n*-butylalkylphosphonium-based RTILs in this study is shown in Figure 1-8 with that of other RTILs given in Table 1-1. Each plot was below the ideal line. The RTILs with $[(CN)_2N]^-$ and $[(FH)_{2.3}F]^-$ exhibited small deviations from the ideal line compared to other RTILs. The $[P_{4,4,4,2OH}][Tf_2N]$ and $[P_{4,4,4,4}]$[DEPDT] showed almost the same deviation from the ideal line, and it was similar to $[P_{4,4,4,1}][Tf_2N]$, $[P_{4,4,4,8}][Tf_2N]$, $[P_{4,4,4,8}]$[SCN], $[P_{4,4,4,12}][Tf_2N]$ and $[P_{4,4,4,allyl}][Tf_2N]$. I concluded that these RTILs have the similar dissociation degree and ion-conduction behavior. In other words, it suggests that the $[DEPDT]^-$ has a potential to be a useful anion in RTIL as an alternative to $[Tf_2N]^-$ that is one of the valuable anions. The dissociation degree of $[P_{4,4,4,12}]$[MCBS] seems to be slightly worse than the aforementioned seven RTILs but was close to $[P_{4,4,4,8}][CF_3COO]$, $[P_{4,4,4,8}][PF_6]$, $[P_{4,4,4,8}]$[OTf], $[P_{4,4,4,8}][BF_4]$, $[P_{4,4,4,8}]$[Tosyl] and $[P_{4,4,4,12}][BF_4]$. The $[P_{4,4,4,12}]$[MCBS] showed a relatively good dissociation degree while it has a very high-viscosity. It would be due to the anomalous framework structure in the $[P_{4,4,4,12}]$[MCBS] as stated already. As for the $[P_{4,4,4,1}]$[DMP], there was a considerable deviation. It is highly likely that the dissociation is insufficient and/or the associated ions exist in this RTIL system.

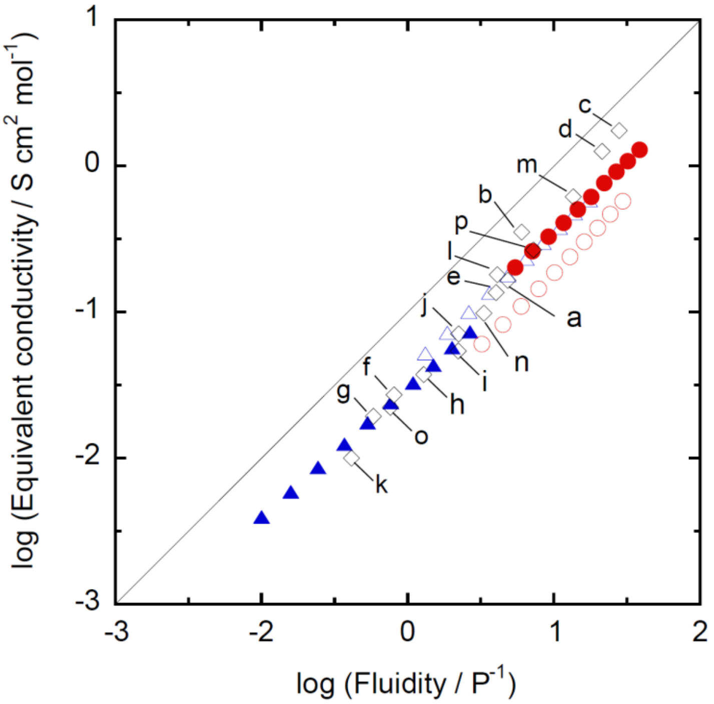

Figure 1-8. Walden plots of the phosphonium cation-based RTILs: (○) [P$_{4, 4, 4, 1}$][DMP]; (●) [P$_{4, 4, 4, 2OH}$][Tf$_2$N]; (△) [P$_{4, 4, 4, 4}$][DEPDT]; (▲) [P$_{4, 4, 4, 12}$][MCBS]; (a): [P$_{4, 4, 4, 1}$][Tf$_2$N]; (b): [P$_{4, 4, 4, 1}$][(CN)$_2$N]; (c): [P$_{4, 4, 4, 1}$][(FH)$_{2.3}$F]; (d): [P$_{4, 4, 4, 4}$][(FH)$_{2.3}$F]; (e): [P$_{4, 4, 4, 8}$][Tf$_2$N]; (f): [P$_{4, 4, 4, 8}$][BF$_4$]; (g): [P$_{4, 4, 4, 8}$][PF$_6$]; (h): [P$_{4, 4, 4, 8}$][OTf]; (i): [P$_{4, 4, 4, 8}$][CF$_3$COO]; (j): [P$_{4, 4, 4, 8}$][SCN]; (k): [P$_{4, 4, 4, 8}$][Tosyl]; (l): [P$_{4, 4, 4, 8}$][(CN)$_2$N]; (m): [P$_{4, 4, 4, 8}$][(FH)$_{2.3}$F]; (n): [P$_{4, 4, 4, 12}$][Tf$_2$N]; (o): [P$_{4, 4, 4, 12}$][BF$_4$]; (p): [P$_{4, 4, 4, allyl}$][Tf$_2$N]. The ideal line was constructed from the data for a diluted KCl aqueous solution.

1-3-2. The Component Effect of RTIL on the Size of Pt or Au Nanoparticles Prepared by Ionic Liquid-Sputtering Method

Although the structure effect of RTIL in ionic liquid-sputtering method has already reported in a few research groups,[60–62,64] there is no information about the dependence of cation structure in resulting metal nanoparticles. At first, to examine the effect, I prepared Pt and Au nanoparticles in RTILs having various onium cations and $[Tf_2N]^-$ as depicted in Figure 1-1. It is well known that $[Tf_2N]^-$ has relatively high thermal stability and reduces the melting point and viscosity for resulting RTIL.[30] The mean particle sizes of obtained Pt and Au nanoparticles were tabulated in Table 1-4 with the formula weight, viscosity, density, molar density and cation volume of each RTIL.[91,103,108–120] The presence of Pt and Au nanoparticles in RTIL could be confirmed by TEM observation except for Pt-sputtered $[C_1C_2Im][Tf_2N]$ and $[C_1C_4Im][Tf_2N]$. Typical TEM pictures of Pt and Au nanoparticles are shown in Figure 1-9. So far, a wide variety of metal nanoparticles were prepared by RTIL-sputtering method using ammonium, pyrrolidinium and imidazolium cation-based RTILs, but I firstly demonstrated applicability of phosphonium cation-based RTIL such as $[P_{4,4,4,2OH}][Tf_2N]$ and $[P_{4,4,4,8}][Tf_2N]$ to this method. In the case of $[C_1C_2Im][Tf_2N]$ and $[C_1C_4Im][Tf_2N]$, Au nanoparticles were observed clearly in contrast to Pt nanoparticles by TEM observation. And also, I confirmed the Pt atoms in Pt-sputtered $[C_1C_2Im][Tf_2N]$ and $[C_1C_4Im][Tf_2N]$ by inductively-coupled plasma atomic emission spectroscopy (ICP-AES), suggesting small Pt clusters (< 1 nm) were existed in the RTIL. These results indicate that the size of metal nanoparticles was determined by not only metal species but also cation structure of RTIL. The mean particle sizes of Au nanoparticles became lager than that of Pt nanoparticles for all RTILs listed in Table 1-4. Our research group has already proposed formation mechanism of metal nanoparticles in the RTIL-sputtering method.[36] Metal nanoparticle grows at gas-liquid interface and diffuses into RTIL with aggregation and stabilization at higher metal concentration. On the other hand, it is reported that the sputtering rate determined by the number of sputtering atoms per one incident ion into metal target depends on metal species and Au shows the higher sputtering rate compared with Pt.[121] That is, Au target can inject more metal atoms or clusters into RTIL than Pt target at the same sputtering condition. This invokes the change of metal concentration between Pt and Au at the gas-liquid interface and triggered the difference of the mean particle size of resulting metal nanoparticles.

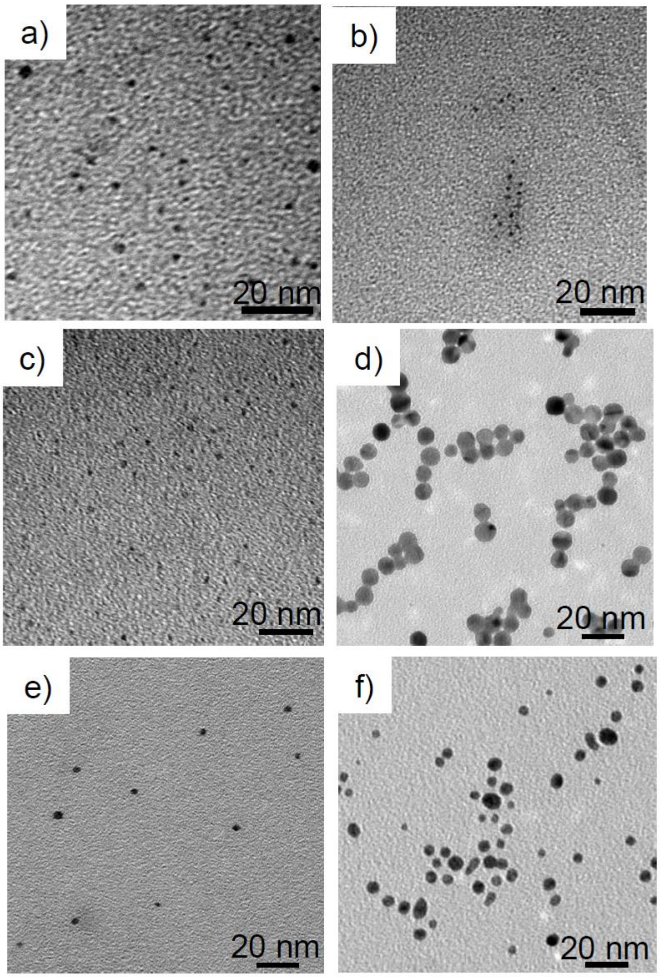

Figure 1-9. TEM pictures of Pt nanoparticles prepared in (a) $[N_{1,1,1,3}][Tf_2N]$, (b) $[Pyr_{1,4}][Tf_2N]$ and (c) $[C_1C_8Im][Tf_2N]$ and Au nanoparticles prepared in (d) $[N_{4,4,4,1}][Tf_2N]$, (e) $[Pyr_{1,3}][Tf_2N]$ and (f) $[C_1C_{10}Im][Tf_2N]$.

Table 1-4. Mean particle sizes of Pt and Au nanoparticles prepared in RTILs with $[Tf_2N]^-$ and physicochemical properties of RTILs

RTILs	FW a)	Mean particle size (nm) b)		Viscosity c) (cP)	Density c) (g cm^{-3})	Molar density d) (mmol cm^{-3})	Cation volume e) ($Å^3$)
		Pt	Au				
$[N_{1,1,1,3}][Tf_2N]$	382.3	2.4	3.3	72	1.44	3.77	159.6
$[N_{2,2,2,5}][Tf_2N]$	452.5	1.4	7.5	127	1.31	2.90	265.7
$[N_{4,4,4,1}][Tf_2N]$	480.5	1.7	8.2	551	1.26	2.62	318.9
$[Pyr_{1,3}][Tf_2N]$	408.4	1.7	3.3	61	1.45	3.55	196.7
$[Pyr_{1,4}][Tf_2N]$	422.4	1.4	3.1	70	1.41	3.34	210.9
$[Pyr_{1,8}][Tf_2N]$	478.5	1.2	6.6	156	1.19	2.49	319.2
$[Pyr_{1,1o1}][Tf_2N]$	410.4	1.6	5.4	40	1.48	3.61	178.3
$[C_1C_2Im][Tf_2N]$	391.3	* f)	3.6	33	1.52	3.88	160.3
$[C_1C_4Im][Tf_2N]$	419.4	* f)	3.0	50	1.45	3.41	207.3
$[C_1C_6Im][Tf_2N]$	447.5	1.2	3.9	70	1.37	3.06	252.7
$[C_1C_8Im][Tf_2N]$	475.1	1.5	3.9	87	1.38	2.91	286.1
$[C_1C_{10}Im][Tf_2N]$	503.5	1.4	4.7	120	1.27	2.52	351.8
$[C_1C_{12}Im][Tf_2N]$	531.2	1.3	4.5	151	1.28	2.41	393.6
$[C_2C_{Allyl}Im][Tf_2N]$	417.0	1.8	6.0	29	1.45	3.48	170.3
$[C_6dimeIm][Tf_2N]$	461.1	1.9	3.9	131	1.35	2.93	265.8
$[P_{4,4,4,8}][Tf_2N]$	595.7	1.9	2.9	250	1.18	1.98	535.5
$[P_{4,4,4,2OH}][Tf_2N]$	527.5	3.4	3.9	242	1.26	2.39	375.1

a) Formula weight. b) Estimated by TEM observation. c) The value at 298 K or 303 K. d) Calculated from the formula weight and density listed in this table. e) Calculated at the B3LYP/6-31+G(d) level. f) We couldn’t estimate the values by TEM observation, but we confirmed the Pt atoms by ICP-AES measurement.

The particle size was influenced by the cation structure of RTIL as described above. The physicochemical properties of RTIL are easily changed by exchanging cation component even if it has a same anion.[105] Figure 1-10 shows the mean particle sizes of Pt and Au nanoparticles with the viscosity of each RTIL. Unfortunately, the mean particle sizes of Pt nanoparticles were too small to evaluate the relativity with the viscosity. For example, the mean particle size in [$N_{4,4,4,1}$][Tf_2N] which has the highest viscosity listed in Table 1-4 was 1.7 nm. This value was comparable with the particle size prepared in other low-viscosity RTILs. In contrast, the tendency between their particle size and viscosity was found in Au nanoparticles for each RTIL. The Au nanoparticles obtained in ammonium, pyrrolidinium, and imidazolium cation-based RTIL showed the increase of their particle size with increase of the viscosity. Considering our proposed formation mechanism aforementioned above, diffusion of atoms and clusters in RTIL is thought to be largely controlled by the viscosity. Thus, it would appear that “high-viscosity” can delay the diffusion and promote the aggregation of atoms and clusters. In the case of the ammonium cation-based RTILs, however, the particle sizes in [$N_{2,2,2,5}$][Tf_2N] and [$N_{4,4,4,1}$][Tf_2N] were almost same regardless of the big difference in the viscosity. This result indicates that the control factor of particle size is so much complicated and not just the viscosity but the conformation of RTIL and how RTIL stabilize metal nanoparticles should be considered. In pyrrolidinium and imidazolium cation-based RTILs, the particle size increased approximately linearly against the viscosity except for [$C_2C_{allyl}Im$][Tf_2N] and [$Pyr_{1,1O1}$][Tf_2N]. It is unclear but I think that the charge localization at allyl group and oxygen atom in the cation structure of these RTILs affects the stable state of metal nanoparticle. As seen in the Au nanoparticle prepared in [$N_{2,2,2,5}$][Tf_2N] and [$C_1C_{10}Im$][Tf_2N], it is obvious that the cation structure strongly affected to the particle size even if the viscosity is almost same. Another possible control factor to determine the particle size in this method is the RTIL surface composition at the gas-liquid interface.[122] Results from sum frequency generation (SFG) vibrational spectroscopy studies show that the cation chain protrudes into the gas phase and the gauche defect decreases as the number of methylene group is increased.[123] This report may explain the tendency observed in Figure 1-10. Because of the decrease of the gauche defect, it becomes slightly difficult that the sputtered atoms and clusters penetrate inside the RTIL. Then, the residence time of those at the surface is increased and the particle size becomes bigger with the higher concentration of metal.

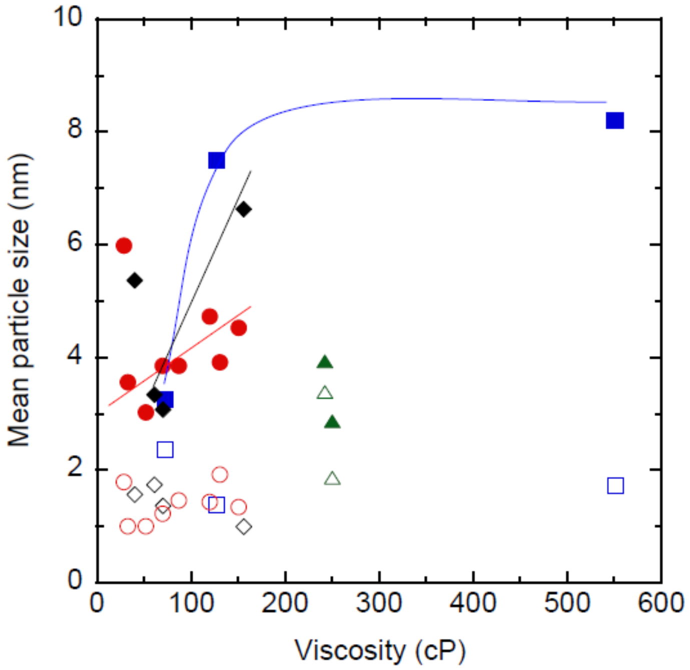

Figure 1-10. Relationship between the mean particle size of Pt (open mark) and Au (solid mark) nanoparticle and the viscosity of ILs with $[Tf_2N]^-$. (□, ■) ammonium cation; (◇, ◆) pyrrolidinium cation; (○, ●) imidazolium cation; (△, ▲) phosphonium type cation.

Figure 1-11 shows the plot of the molar density with the obtained particle sizes. As is the case with the plot against the viscosity, it was difficult to see the tendency for the particle size of Pt nanoparticles. On the other hand, the mean particle sizes of Au nanoparticles were decreased with increase of the density in ammonium, pyrrolidinium, and imidazolium cation-based RTIL. $[C_2C_{allyl}Im][Tf_2N]$ and $[Pyr_{1,1O1}][Tf_2N]$ also deviated from the line significantly. The molar density normally decreases with increasing alkyl chain length as to the 1,3-dialkylimidazolium cation-based RTILs.[124] I think that the molar density contributes to the stabilization of metal nanoparticles in RTIL. Since the constituent molecules exist thickly in the high-density RTILs, the nanoparticles are easily stabilized by high concentration stabilizing molecules compared to aggregate each other. Moreover, I tried to examine the correlativity of the particle size with the physicochemical properties such as conductivity, kinematic viscosity, Walden product, cationic volume and void volume calculated by cation and anion volume, but I could not obtain the result which is reasonable to consider the control factor of the particle size.

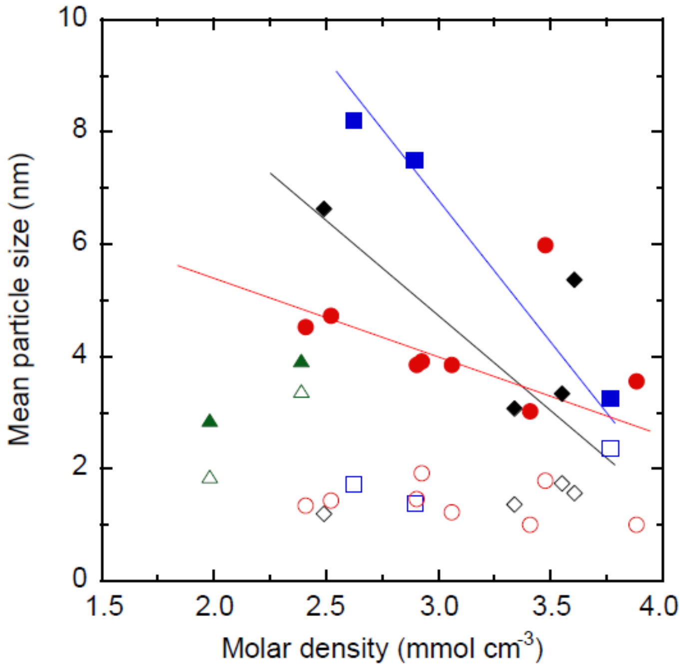

Figure 1-11. Relationship between the mean particle size of Pt (open mark) and Au (solid mark) nanoparticle and the molar density of ILs with $[Tf_2N]^-$. (□, ■) ammonium cation; (◇,◆) pyrrolidinium cation; (○, ●) imidazolium cation; (△, ▲) phosphonium type cation.

To investigate the influence of the anion species, Au nanoparticles were prepared in following RTILs: $[C_1C_4Im][Tf_2N]$, $[C_1C_4Im][PF_6]$, $[C_1C_4Im][TfO]$ and $[C_1C_4Im][BETI]$.

The TEM images of Au nanoparticles are shown in Figure 1-12 and the mean particle sizes are listed in Table 1-5 with the viscosity, density, molar density and calculated anion volume of each RTIL.[105] The corresponding nanoparticles in these RTILs had spherical shapes. And their mean particle size did not change drastically compared with changing the alkyl chain length of imidazolium cation. Dupont *et al.* reported that the particle size of Au nanoparticles in this method is affected by the fluorinated moieties on the RTIL surface.[64] They also reported that imidazolium cation plays a crucial role to stabilize Au nanoparticle prepared by reduction of precursor in RTIL.[125] The fluorinated moieties at the surface of these four RTILs in this study are comparable from the result of the angled-resolved X-ray photoelectron spectroscopy (ARXPS).[126,127] With the result and previous reports, the influence of anion species for the particle size is small using same cation component.

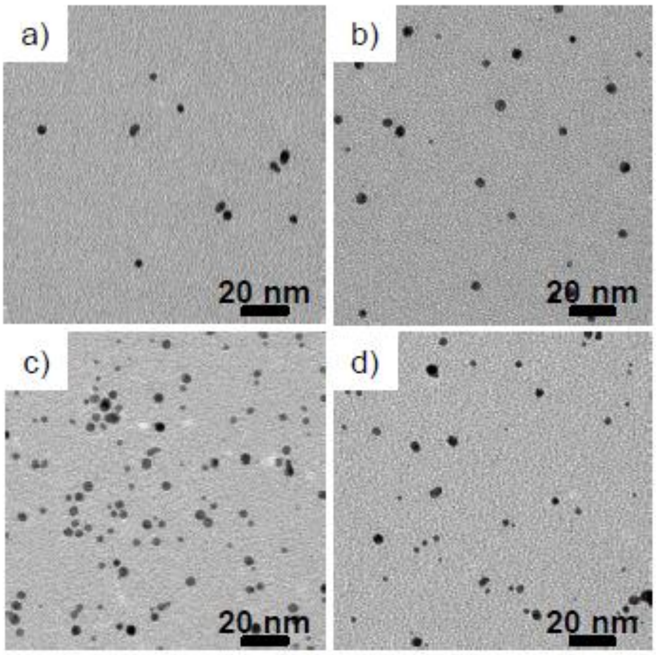

Figure 1-12. TEM pictures of Au nanoparticles prepared in (a) [C_1C_4Im][Tf_2N], (b) [C_1C_4Im][PF_6], (c) [C_1C_4Im][TfO] and (d) [C_1C_4Im][BETI].

Table 1-5. Mean particle sizes of Au nanoparticles prepared in [C_1C_4Im]-based RTILs and physicochemical properties of RTILs

RTILs	FW a)	Mean particle size b) (nm)	Viscosity c) (cP)	Density c) (g cm^{-3})	Molar density d) (mmol cm^{-3})	Cation volume e) ($Å^3$)
[C_1C_4Im][Tf_2N]	419.4	3.0	50	1.45	3.45	199.6
[C_1C_4Im][PF_6]	284.2	3.7	261	1.37	4.82	113.5
[C_1C_4Im][TfO]	288.3	3.4	84	1.30	4.51	122.3
[C_1C_4Im][BETI]	519.4	3.5	109	1.50	2.89	285.1

a) Formula weight. b) Estimated by TEM observation. c) The value at 298 K or 303 K. d) Calculated from the formula weight and density listed in this table. e) Calculated at the B3LYP/6-31+G(d) level.

Table 1-6. Mean particle sizes of Pt and Au nanoparticles prepared in phosphonium cation-based RTILs and physicochemical properties of RTILs

RTILs	FW a)	Mean particle size (nm) b)		Viscosity c) (cP)	Density c) (g cm^{-3})	Molar density d) (mmol cm^{-3})	Cation size e) ($Å^3$)	Anion volume e) ($Å^3$)
		Pt	Au					
[$P_{4,4,4,1}$][DMP]	342.4	4.2	4.63	530	1.03	3.01	346.8	140.3
[$P_{4,4,4,2OH}$][Tf_2N]	527.5	3.4	3.9	242	1.26	2.39	375.1	199.6
[$P_{4,4,4,4}$][DEPDT]	444.7	4.3	4.4	1078	1.01	2.27	389.9	217.3
[$P_{4,4,4,8}$][Tf_2N]	595.7	1.9	2.9	250	1.18	1.98	535.0	199.6
[$P_{4,4,4,8}$][TfO]	464.6	* f)	* f)	778	1.08	2.32	535.0	122.3
[$P_{4,4,4,8}$][CF_3COO]	428.6	2.3	1.4	453	1.03	2.40	535.0	100.6
[$P_{4,4,4,8}$][TS]	486.7	1.8	3.0	2435	1.02	2.10	535.0	192.8
[$P_{4,4,4,12}$][MCBS]	644.9	4.1	4.0	16401	1.05	1.63	567.7	265.5

a) Formula weight. b) Estimated by TEM observation. c) The value at 298 K or 303 K. d) Calculated from the formula weight and density listed in this table. e) Calculated at the B3LYP/6-31+G(d) level. f) We couldn’t estimate the values by TEM observation, but we confirmed the Pt atoms by ICP-AES measurement.

Aforementioned above, I elucidated that phosphonium cation-based RTIL with $[Tf_2N]^-$ can be applied to produce the metal nanoparticles in this method. To extend the knowledge, I prepared Au and Pt nanoparticles in wide variety of phosphonium cation-based RTILs. The obtained particle sizes and the physicochemical properties of RTILs are listed in Table 1-6 with $[P_{4,4,4,8}][Tf_2N]$ and $[P_{4,4,4,2OH}][Tf_2N]$.[74] The nanoparticles were newly confirmed by TEM observation in following RTILs: $[P_{4,4,4,1}]$[DMP], $[P_{4,4,4,4}]$[DEPDT], $[P_{4,4,4,8}][CF_3COO]$, $[P_{4,4,4,8}]$[TS]. In $[P_{4,4,4,8}]$[TfO], it was difficult to evaluate the particle size by TEM observation but the presence of metal atoms in RTIL was confirmed by ICP-AES same as Pt-sputtered $[C_1C_2Im][Tf_2N]$ and $[C_1C_4Im][Tf_2N]$. The correlativity of the particle size with the physicochemical properties of phosphonium cation-based RTIL was studied. But unfortunately, any tendency was not found. This reason is unclear but I believe that part of it is the higher dissociation degree of phosphonium cation-based RTILs compared to other nitrogen-containing onium cations. I plan to continue the investigation for the key control factor of particle size in phosphonium cation-based RTILs. Another interesting phenomenon was observed when the metal was sputtered onto $[P_{4,4,4,8}]$[MCBS] whose viscosity is 16401 cP. Au or Pt thin film was formed at the surface and small amount of metal nanoparticles were confirmed inside RTIL by TEM observation. This result implies that its high viscosity delays the diffusion of sputtered metal clusters into RTIL enough to form the film.

Considering results described above, I discuss the control factor of the particle size in ionic liquid-sputtering method. The particle size is not dominated by one physicochemical property and is affected by various factors. The proposed formation mechanism can divide into three phase as shown in Figure 1-13. As the first phase, the amount of sputtered metal atoms and clusters are dependent of the kind of metal target with different sputtering rate, resulting the metal concentration at RTIL surface are changed. Therefore, the difference of the particle size between Pt and Au is provoked at same sputtering condition. Indeed, this was regulated by controlling the sputtering conditions and the effects of sputtering condition in ionic liquid-sputtering method have already reported by Nishikawa *et al*. The second phase is growth at gas-liquid surface. At this phase, the population of alkyl chains is the key factor to determine the particle size. As increasing alkyl chains of cationic component, it exists densely at the RTIL surface and makes difficult for the sputtered metal atoms and clusters to penetrate inside RTIL. The last phase is the diffusion and the stabilization inside RTIL. The viscosity has an implication for the diffusion inevitably, which is evidenced by the thin metal film formed using very high-viscous RTIL. The stabilization process is affected by the molar density and the structure of cationic component. At present, this proposed mechanism is applicable to imidazolium, pyrrolidinium and ammonium cation-based RTILs. For the phosphonium cation-based RTIL, I have many unknowns about the control factor and have the plan to continue the investigation.

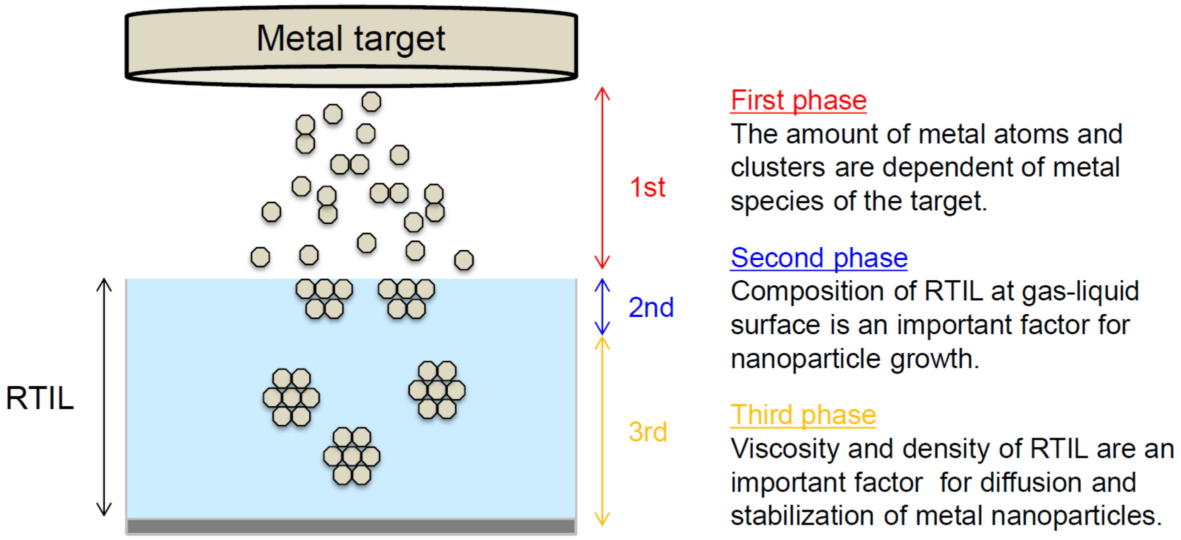

Figure 1-13. Schematic illustration of proposed formation mechanism of nanoaprticles by RTIL-sputtering method.

1-4. Conclusions

In this study, at first, I examined the physicochemical properties of the distinctive tri-*n*-butylalkylphosphonium-based RTILs. All the RTILs prepared in this investigation indicated a favorable thermal decomposition temperature exceeding 560 K. The $[P_{4,\,4,\,4,\,12}]$[MCBS] had a fairly-high thermal stability, and several unique physicochemical behaviors in the RTIL were revealed. The physicochemical behavior would be caused by the anomalous framework structure in the RTIL. The $[P_{4,\,4,\,4,\,1}]$[DMP] formed an ionic plastic crystal phase, but the $[P_{4,\,4,\,4,\,4}]$[DEPDT] with the ion structures similar to $[P_{4,\,4,\,4,\,1}]^+$ and $[DMP]^-$ was not the case. The $[P_{4,\,4,\,4,\,2OH}][Tf_2N]$ showed a relatively-high conductivity among the tri-*n*-butylalkylphosphonium-based RTILs with usual fluoroanion. There is no doubt that the anion structure in the phosphonium cation-based RTILs strongly affect the thermal stability and the phase transition properties. These results will be useful information if novel functional phosphonium-based RTIL system is designed.

Furthermore, focusing on the RTIL species, I investigated the control factors that affect the size of metal nanoparticle prepared by ionic liquid-sputtering method. I prepared Pt and Au nanoparticles in wide variety of RTIL and firstly demonstrated applicability of phosphonium cation-based RTIL to this method. The mean particle sizes of obtained Pt and Au nanoparticles were compared with their physicochemical properties. Although the particle size was too small to evaluate the correlativity in Pt-sputtered RTIL, the tendency with the viscosity and density was found at Au nanoparticle prepared in imidazolium, pyrrolidinium and ammonium cation-based RTILs with $[Tf_2N]^-$. And also, we examined the anion effect for the particle size using $[C_1C_4Im]^+$ and found that it is smaller than the cation effect. In the phosphonium cation-based RTILs, no tendency with the physicochemical properties was observed. There is no doubt that the control factor of the particle size is so complicated and affected by various factors. These results will be helpful information to prepare metal nanoparticles by ionic liquid-sputtering method.

Chapter 2

Preparation of Pt Nanoparticle-Supported Carbon Composite Materials and Their Application to Electrocatalyst

2-1. Introduction

Platinum possesses inherently a high catalytic activity for electrochemical oxygen reduction reaction (ORR). Further enhancement of Pt catalytic ability is one of the keys for practical application of polymer electrolyte fuel cell (PEFC) systems because abundance of Pt on the planet is finite. Various preparation processes on novel Pt catalysts have been reported.[16–20] There are some interesting articles reporting that RTIL-modified Pt or Au nanoparticles show a good catalytic activity toward O_2 reduction.[128–132] As already mentioned in the general introduction, our research group have succeeded to synthesize Pt nanoparticles having ca. 2 ~ 4 nm in diameter by the ionic liquid–sputtering method and to immobilize the prepared Pt nanoparticles on the surface of glassy carbon (GC) electrode for ORR.[53] Unfortunately, however, it did not include important information such as surface condition and detailed electrocatalytic activity of Pt-embedded GC electrode.

There is also no report about immobilization of metal nanoparticles prepared by this method on carbon nanotube (CNT) that is a promising supporting material for catalytically active nanoparticles due to favourable physicochemical properties and large surface area to volume ratio.[133] Regardless of metal nanoparticle preparation method, it is very difficult for us to immobilize metal nanoparticles on the CNT possessing a chemical inertness surface. Nevertheless, a couple of successful approaches to immobilize metal nanoparticle onto the

CNT surface have already been proposed. A commonly-used approach is a CNT oxidation method with a strong acid.[134] By this approach, aromatic rings on CNT are partially wrecked, and it offers active sites for metal nanoparticle immobilization, e.g., –COOH and –OSO_3H groups. Another popular approach is a wrapping method: CNT is covered with a functionalized polymer that works as an organic linker.[132,135] These conventional approaches often have an adverse impact on original electrical property and chemical stability of CNT owing to partial breakup of the π conjugation skeleton and reduction of contact points among the CNTs.

The aim of this chapter is, using the Pt nanoparticle-dispersed RTILs prepared by the ionic liquid–sputtering method, to examine the catalytic activity of Pt-embedded GC electrode and to establish a facile approach for fabrication of the Pt nanoparticle-immobilized SWCNT (Pt–IL-SWCNT) composite without any special pretreatment of the SWCNT.

2-2. Experimental section

2-2-1. Preparation of RTILs

N,*N*,*N*-trimethyl-*N*-propylammonium bis(trifluoromethanesulfonyl)amide ($[N_{1,1,1,3}][Tf_2N]$), *N*,*N*,*N*-triethyl-*N*-octylammonium bis(trifluoromethanesulfonyl)amide ($[N_{2,2,2,5}][Tf_2N]$), *N*-methyl-*N*-propylpyridinium bis(trifluoromethanesulfonyl)amide ($[Pyr_{1,3}][Tf_2N]$), *N*-butyl-*N*-methylpyridinium bis(trifluoromethanesulfonyl)amide ($[Pyr_{1,4}][Tf_2N]$), 1-ethyl-3methylimidazolium bis(trifluoromethanesulfonyl)amide ($[C_1C_2Im][Tf_2N]$), 1-allyl-3-ethylimidazolium bis(trifluoromethanesulfonyl)amide ($[C_2C_{Ally}Im][Tf_2N]$) were purchased from Kanto Chemical Co., Inc. *N*-methyl-*N*-methoxymethylpyridinium bis(trifluoromethanesulfonyl)amide ($[Pyr_{1,1O1}][Tf_2N]$) was provided by Otsuka Chemical Co., Ltd. These RTILs were purified with the method described in previous reports before use.[1-3] *N*,*N*,*N*-tributyl-*N*-methylammonium bis(trifluoromethanesulfonyl)amide ($[N_{4,4,4,1}][Tf_2N]$) and 1-hexyl-2,3-dimethylimidazolium bis(trifluoromethanesulfonyl)amide

([C_6dimeIm][Tf_2N]) were prepared by mixing exactly equal molar amounts of the purified organic chloride salts, *N*,*N*,*N*-tributyl-*N*-methylammonium chloride and 1-hexyl-2,3-dimethylimidazolium chloride, and Li[Tf_2N] in ultrapure water with dichloromethane. The solution was agitated at room temperature for 12 hrs. The dichloromethane phase containing RTIL was washed repeatedly with reverse osmosis (RO) water until the water phase was found to contain no chloride as determined by the addition of a few drops of a silver nitrate solution.

2-2-2. Preparation of Pt nanoparticles

A soda glass plate (2.5 × 2.5 cm), on which RTIL (0.4 mL) was spread, was set in a Cressington108 auto SE sputter coater. A Pt foil target (ø5.7 cm, 99.98 %) was placed on 4.5 cm above the glass plate. Sputter deposition onto RTIL was conducted with sputter current of 40 mA in dry Ar (99.999 %) atmosphere whose pressure did not exceed 7 ± 1 Pa. The sputtering was conducted by direct current (DC) mode at room temperature (298 ± 2 K).

2-2-3. Preparation of Pt nanoparticles-supported carbon materials

The Pt nanoparticle-embedded glassy carbon electrode (Pt-GCE) was prepared by the following procedures; (*i*) heat treatment of the Pt-sputtered RTIL on a glassy carbon (GC) plate (2.5 × 2.5 cm) at various temperatures under atmospheric conditions; (*ii*) immersing the glassy carbon plate with 1.67 M KOH iso-propanolic solution for 12 hrs or rinsing the plate with dry acetonitrile; (*iii*) drying the resulting electrode under vacuum for 30 minutes prior to use. The heat treatment was conducted with a Koyo Thermo Systems REX-C900. If iso-propanolic solution was employed for the (*ii*), the glassy carbon plate was rinsed with nitric acid solution and ultrapure water before the drying process.

The Pt nanoparticle-immobilized SWCNT (Pt-IL-SWCNT) was prepared by the following procedures; The SWCNT was purchased from Meijo Nano Carbon Co., Inc. SWCNT (1 mg) without further treatment was mixed with a 0.4 mL Pt-sputtered RTIL by pestling in a mortar, followed by ultrasonication for 30 min and agitation for 10 hrs. Further treatment was conducted with heating the mixture at 573 K for 5 hrs. The final product, Pt-modified SWCNT (Pt-IL-SWCNT), was obtained after washing the resultant composite by acetonitrile several times and drying it for 2 hrs in vacuo.

2-2-4. Characterization

Morphology of the obtained Pt nanoparticle and Pt-IL-SWCNT composite material was observed by a HITACHI H-7650 transmission electron microscope (TEM) with an acceleration voltage of 100 kV. Before the TEM observation, the sample grids were prepared by dropping the Pt sputtered-RTIL and the Pt–SWCNT dispersed isopropanol solution onto a TEM grid (ø3.0 mm, copper, 400 mesh) and a TEM microgrid (ø3.0 mm, copper, 167 mesh), respectively. The original TEM grids were coated with an amorphous carbon thin layer. Elemental analysis of the specimens was performed with an EDAX Genesis-XM2 energy dispersive X-ray spectrometer (EDX) mounted on the TEM. Morphology of Pt-GCE was observed by a Keyence VE-8800 scanning electron microscope (SEM). Surface condition analysis of the Pt-GCE was carried out by using a PerkinElmer Spectrum 100 FT-IR spectrometer with an attenuated total reflectance unit. The Pt content in the Pt–SWCNT was measured by a Shimadzu ICPS-7510 inductively coupled plasma atomic emission spectrometer (ICP-AES). The chemical state of the elements contained in the Pt–SWCNT was examined by a KRATOS AXIS-ULYRA HSA X-ray photoelectron spectroscopy.

2-2-5. Electrochemical experiments

Electrocatalytic activities for Pt-GCE toward O_2 reduction were examined with an ALS Model 660A potentiostat/galvanostat controlled with a desktop computer and a three-electrode cell. A Pt mesh was used as the counter electrode. The Ag/AgCl electrode immersed in a KCl-saturated solution was employed as the reference electrode. Active surface area of the Pt-GCE was determined with amount of adsorbed carbon monoxide (GL Sciences, 99.9 %) that was electrochemically estimated by reference to previous reports.[136,137] The resulting Pt-GCE was pretreated with multiple potential scans between 0.5 and +1.25 V (*vs.* RHE) under dry N_2 condition before oxygen reduction experiments in 0.5 M H_2SO_4 aqueous solution. The 0.5 M H_2SO_4 solution was deaerated with oxygen gas (99.999 %) for more than 30 minutes.

Electrocatalytic activities for a Pt-IL-SWCNT toward oxygen reduction were examined with a Hokuto Denko HZ-5000 potentiostat/galvanostat controlled with a desktop computer. The electrochemical experiments were conducted by using a three-electrode cell. A glassy carbon (GC) rotating ring-disk electrode (RRDE) (Pt ring: 0.1866 cm^2; GC disk: 0.2475 cm^2 (Pine Instruments)) was used as the working electrode. After preparation of Pt-IL-SWCNT (1 mg) dispersed in *i*-propanol solution (0.2 mL), the solution of 5 μL was applied to the GC disk of the RRDE, and the *i*-propanol solution was evaporated in air. Finally the GC disk was covered with a Nafion® *i*-propanolic solution of 5 μL to robustly fix the Pt-IL-SWCNT on the GC. A Pt mesh was used as the counter electrode. The Ag/AgCl double-junction electrode immersed in a KCl-saturated solution was employed as the reference electrode. All potential values are reported with respect to reverse hydrogen electrode (RHE). The prepared Pt–SWCNT working electrode was pretreated with multiple potential scans between 0.5 and +1.25 V (*vs.* RHE) in 0.1 M $HClO_4$ aqueous solution under dry N_2 condition before oxygen reduction experiments. Cyclic voltammograms were recorded at the Pt-IL-SWCNT modified RRDE electrode in 0.1 M $HClO_4$ aqueous solution saturated with N_2 or O_2 gas. Prior to the measurements, the solution was aerated with N_2 or O_2 more than 30 min. Hydrodynamic voltammetry was carried out under O_2 atmosphere. The scan rate was 10 mV s^{-1} and the rotating rate was 1200 rpm. The potential at the ring was maintained at 1.20

V (*vs.* RHE) so as to entirely oxidize hydrogen peroxide (H_2O_2) generated by an undesirable two-electron O_2 reduction reaction. H_2O_2 generation rate, x_{H2O2} (%), on the GC disk was calculated from the following formula[138]

$$x_{\mathrm{H_2O_2}} = \frac{200 I_{\mathrm{R}}/N}{I_{\mathrm{D}} + I_{\mathrm{R}}/N}$$

where I_{R} is the ring current, I_{D} is the disk current and N is the collection efficiency, here, the N value was 0.40. By this electrochemical analysis, I can estimate the percentage for the two-electron reaction involved in the electrochemical O_2 reduction reaction at each potential as x_{H2O2}.

2-3. Results and discussion

2-3-1. Preparation of Pt nanoparticles

Pt nanoparticles can be produced by ionic liquid-sputtering method onto trimethyl-*n*-propylammonium bis((trifluoromethyl)sulfonyl)amide, $[N_{1,1,1,3}][Tf_2N]$, without any stabilizing agents. This simple process can reproducibly yield Pt nanoparticles. Figure 2-1 depicts TEM images of Pt nanoparticles obtained by the Pt sputtering onto $[N_{1,1,1,3}][Tf_2N]$ at different sputtering times and their size distribution diagrams constructed from the TEM images. All the Pt nanoparticles have mean particle size of ca. 2.3 ~ 2.4 nm, and the particle size was of little relevance to the sputtering time. But the Pt concentration in the sputtered RTILs linearly increased with increasing the sputtering time. It is known that these Pt nanoparticles become slightly large after heat treatment exceeding 423 K.[53] The mean particle size (ca. 3.7 ± 0.1 nm) is substantially constant value independently of the heat temperature if the heat temperature is 423 ~ 573 K. 573 K was chosen as the maximum heat temperature to avoid pyrolysis of the RTIL. In this investigation, based on the report, heat treatment was carried out at 473 ~ 573 K so as to prepare a Pt nanoparticle-embedded glassy carbon electrode (Pt-GCE) because catalyst efficiency of Pt nanoparticle reaches the maximum at 4.0 nm in diameter.[139]

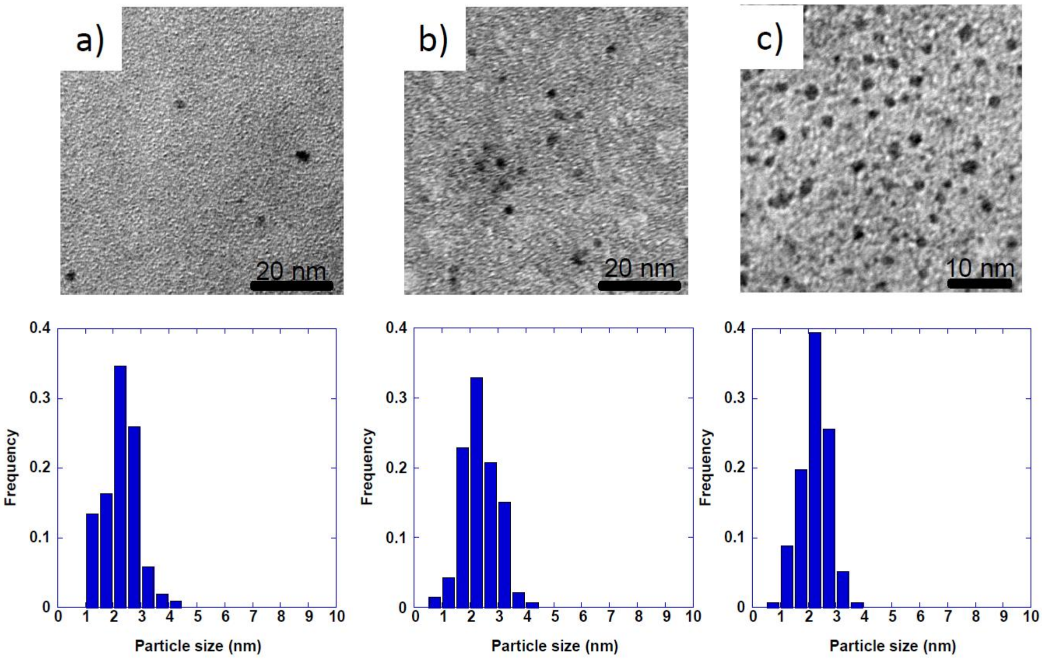

Figure 2-1. TEM images and their size distribution diagrams at different sputtering time. (a) 300 sec; (b) 900 sec; (c) 1800 sec.

2-3-2. ORR on Pt-GCEs

In our research group, it has been reported that Pt-GCE shows a favorable catalytic activity for ORR in 0.5 M H_2SO_4 aqueous solution.[53] But unfortunately it did not include important information on the surface condition of Pt nanoparticles on the Pt-GCE and on the catalytic ability of the Pt nanoparticles per unit area. The former was examined with infrared reflection absorption spectroscopy, and the latter was determined by a common electrochemical method. Figure 2-2a and b indicate infrared reflection spectra for pure $[N_{1,1,1,3}][Tf_2N]$ and Pt-GCE rinsed with 1.67 M KOH iso-propanolic solution. After rinsing the Pt-GCE, there was no peak related to the RTIL, i.e., bare Pt surface appeared.

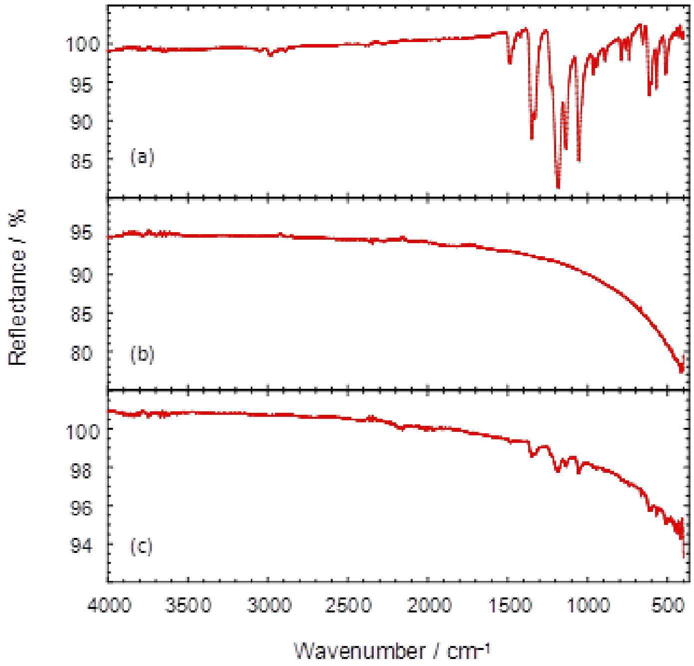

Figure 2-2. Reflective FT-IR spectra of Pt-GCE prepared at 573 K. (a) $[N_{1,1,1,3}][Tf_2N]$ on GC without heat treatment; (b) Pt-GCE rinsed with KOH iso-propanolic solution and nitric acid; (c) Pt-GCE rinsed with acetonitrile.

In order to determine active surface area of the Pt nanoparticles on the Pt-GCE, carbon monoxide, CO, stripping voltammetry was conducted. Steady state cyclic voltammograms recorded at CO-absorbed Pt-GCEs are shown in Fig. 2-3a~c. These Pt-GCEs were prepared at 473, 523, and 573 K. At first cycle, in all figures, an obvious oxidation wave corresponding to CO stripping appears at 0.8 ~ 0.9 V, and the wave completely disappears at second cycle. The CO stripping wave becomes large with increasing the heat temperature for the Pt-embedded process. The Pt areas at the heat temperature of 473, 523, and 573 K were 0.031, 0.100, and 0.200 cm^2-Pt, respectively. At second cycle, typical hydrogen adsorption and desorption peaks for Pt nanoparticle were observed in each cyclic voltammogram.[140] Catalytic activity of these Pt-GCEs was examined by cyclic voltammetry in O_2-saturated H_2SO_4 aqueous solution. In each case, a distinct reduction wave for ORR appeared (Fig. 2-4). What is interesting is that the catalytic activity per unit area was enhanced at lower heat treatment temperature. In fact, I expected an opposite result; that is, the catalytic activity per unit area increases as the Pt-embedded temperature increases because our previous result was that the reduction current for ORR increased at higher heat treatment temperature. To understand this unexpected result precisely, surface morphology of these electrodes was observed by SEM. Figure 2-5 exhibits typical SEM images at various Pt-embedded temperatures. Here, white color moiety should be Pt since Pt can release more secondary electrons than glassy carbon. SEM images obviously whiten as the Pt-embedded temperature increases, i.e., amount of embedded Pt nanoparticles increases with the temperature. Therefore, increment in apparent reduction current for ORR should be caused by increase in Pt nanoparticles embedded on the GC. However, as shown in Fig. 2-4, the catalytic activity per unit area for the ORR becomes small at higher Pt-embedded temperature. It is highly likely that effective Pt surface area decreases if the Pt-embedded temperature increases because a dense Pt nanoparticle layer is formed on GC at higher temperature (Fig. 2-5). At this moment, I cannot give the data on optimization of Pt-embedded condition to meet both higher current for the ORR and higher catalytic activity of the Pt nanoparticles per unit area.

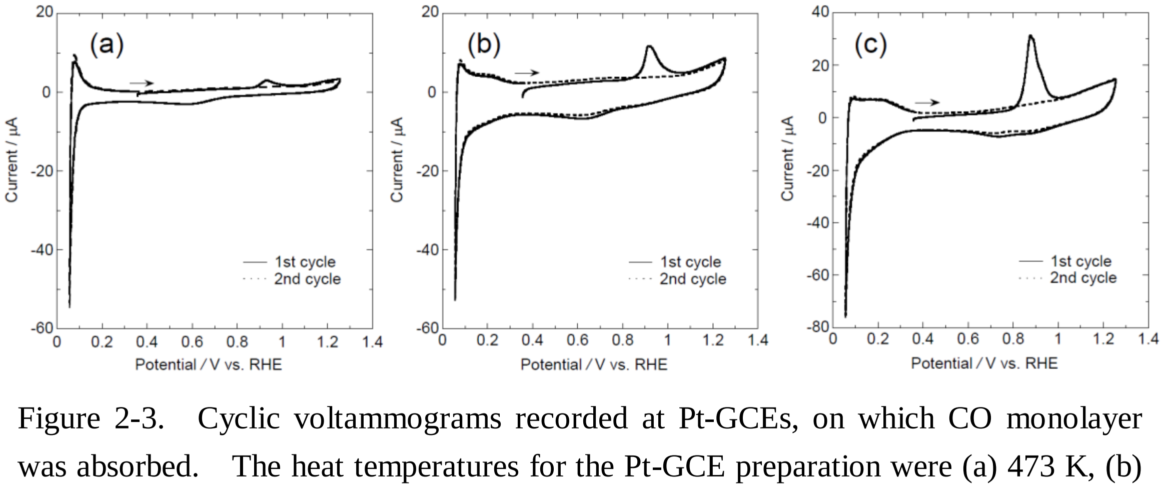

Figure 2-3. Cyclic voltammograms recorded at Pt-GCEs, on which CO monolayer was absorbed. The heat temperatures for the Pt-GCE preparation were (a) 473 K, (b) 523 K, and (c) 573 K. The electrolyte was 0.5 M H_2SO_4 aqueous solution at 298 K. The scan rate was 10 mV s^{-1}.

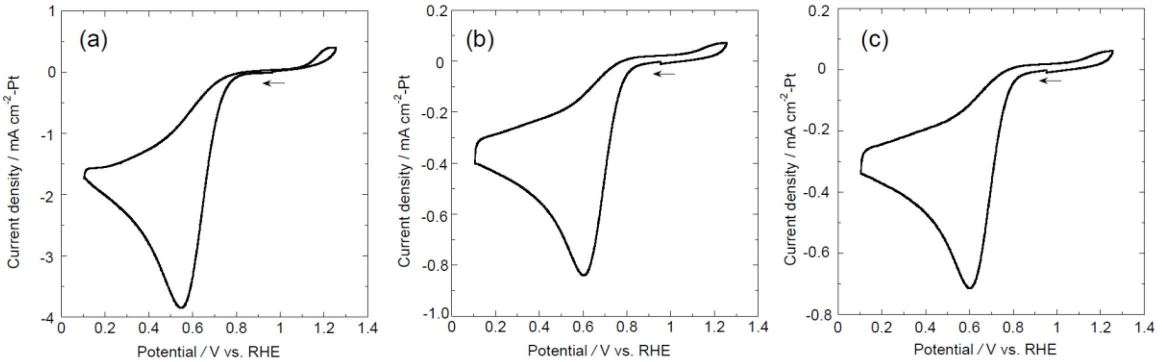

Figure 2-4. Cyclic voltammograms recorded at Pt-GCEs in O_2-saturated 0.5 M H_2SO_4 aqueous solution at 298 K. The heat temperatures for the Pt-GCE preparation were (a) 473 K, (b) 523 K, and (c) 573 K. The scan rate was 10 mV s^{-1}.

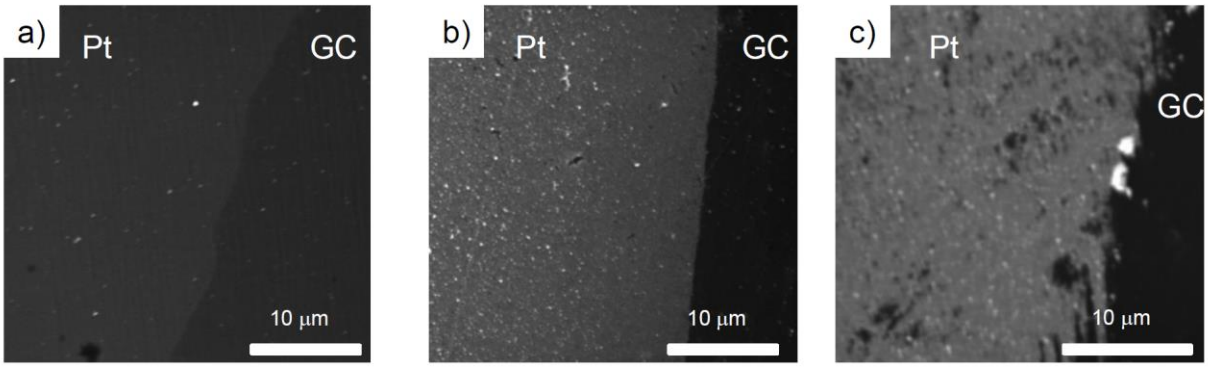

Figure 2-5. SEM images of Pt-GCEs prepared at (a) 473 K, (b) 523 K, and (c) 573 K. The Pt-GCEs were rinsed with KOH iso-propanolic solution and nitric acid.

2-3-3. ORR on RTIL-modified Pt-GCEs

Several research groups point out that RTIL improves a catalytic ability for ORR.[128–132] I have investigated ORR using a RTIL-modified Pt-GCE. The RTIL-modified Pt-GCE was prepared by rinsing Pt-GCE with dry acetonitrile, not 1.67 M KOH iso-propanolic solution. The surface state of the Pt-GCE was examined with infrared reflection absorption spectroscopy. As shown in Fig. 2-2(c), the Pt-GCE rinsed with dry acetonitrile indicated weak absorption related to the $[N_{1,1,1,3}][Tf_2N]$. I named it RTIL-modified Pt-GCE in this article. The surface area of the RTIL-modified Pt-GCE was estimated by using CO stripping voltammetry, like original Pt-GCE described above. Figure 2-6a indicates cyclic voltammograms recorded at the RTIL-modified Pt-GCE on which CO was absorbed. There is a no CO stripping wave, but is a reduction wave for hydrogen evolution. It implies that the RTIL-modified Pt-GCE is electrochemically active without CO poisoning. As expected, RTIL-modified Pt-GCE with CO poisoning reduced oxygen electrochemically (Fig. 2-6b). In fact, a number of groups report an effective interaction between RTIL and metal nanoparticles.[141–143] Probably the interaction prevents CO adsorption onto the Pt nanoparticles. Catalytic activity of the RTIL-modified Pt-GCE without CO poisoning toward ORR was investigated by cyclic voltammetry (Fig. 2-6c). This RTIL-modified electrode showed better catalytic ability than an original RTIL-modified Pt-GCE. The reason is not clear but the high activity would be due to the high oxygen solubility in the RTIL.[41] Using $[N_{1,1,1,3}][Tf_2N]$ as a solvent and a material, I succeeded to fabricate a novel electrode, which has both O_2 reduction catalytic ability and anti-CO poisoning nature.

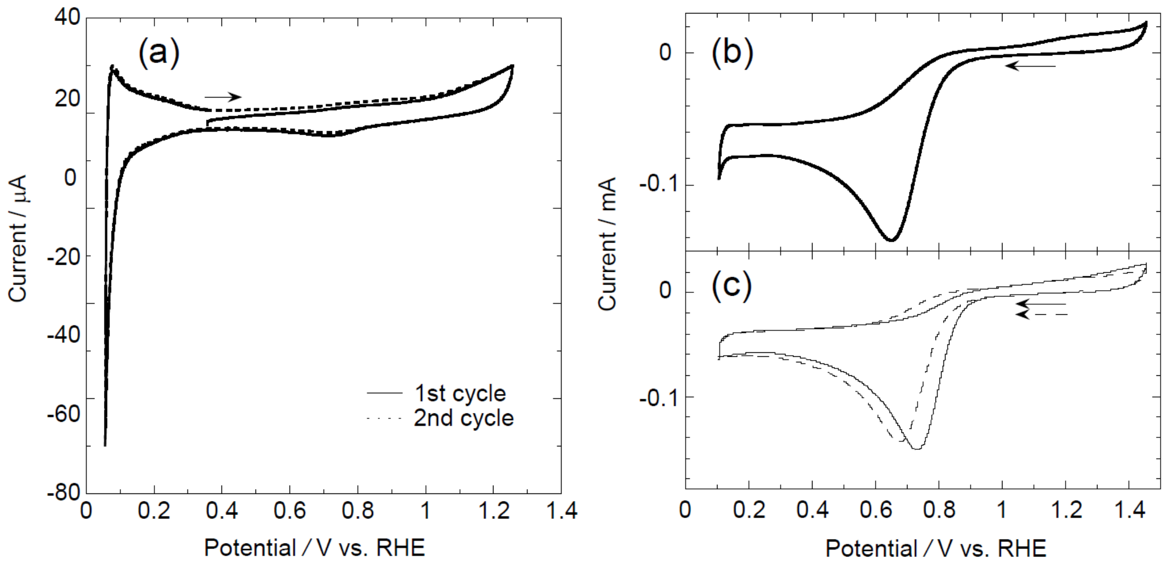

Figure 2-6. Cyclic voltammograms recorded at (a) a RTIL-modified Pt-GCE, on which CO monolayer was absorbed, (b). a RTIL-modified Pt-GCE with CO poisoning and (c) (—) a RTIL-modified Pt-GCE and (- - -) an original Pt-GCE under O_2-saturated atmosphere. The heat temperature for the Pt-GCE preparation was 573 K. The electrolyte was 0.5 M H_2SO_4 aqueous solution at 298 K. The scan rate was 10 mV s^{-1}.

2-3-3. Pt nanoparticle Immobilization onto SWCNT

The Pt nanoparticle-dispersed RTILs prepared by the ionic liquid–sputtering method were exploited for fabrication of Pt nanoparticle-immobilized SWCNT composite material. The fabrication process is depicted in Scheme 2-1. This approach never needs a laborious pretreatment of the SWCNT and any chemical reagents. One thing that we have to do is to agitate the mixture of the Pt nanoparticle-dispersed RTIL and SWCNT with heating. After completing the agitation process, the resulting mixture was rinsed in a dry acetonitrile several times to remove excess RTIL. Eventually I collected the target Pt-IL-SWCNT composite by a centrifuge separation method. The Pt-IL-SWCNT was dried in vacuum before use. As discussed below, I revealed that minuscule amounts of RTIL remains in the Pt-IL-SWCNT by XPS analysis. Fig. 2-7 represents TEM images of Pt-IL-SWCNT fabricated under different Pt-nanoparticle preparation conditions. If the Pt nanoparticles were prepared in $[N_{1,\ 1,\ 1,\ 3}][Tf_2N]$, many of them were readily immobilized on SWCNT by approach developed in this thesis. The amount of the Pt nanoparticles supported on the composite could be controlled by the sputtering time for the Pt nanoparticle preparation (Fig. 2-7a–c and Table 2-1). The mean particle size was ca. 3.2–3.5 nm independent of the sputtering time although it became larger than original Pt nanoparticle size during the agitating process at 573 K in the Scheme 2-1. EDX data and size distribution diagram of the Pt nanoparticles supported on the SWCNT are presented in Fig. 2-8. As given in Table 2-2, mean particle size of the Pt nanoparticles on the Pt-IL-SWCNT composite varied with RTIL species used for the Pt sputtering process (Fig. 2-8, 2-9, and 2-10). The value was ca. 2.3–3.5 nm except $[C_1C_2Im][Tf_2N]$. The amount of Pt nanoparticles was up to 32.0 wt%, but it was difficult to support Pt nanoparticles dispersed in imidazolium-based RTILs onto the SWCNT. The Pt content in the Pt-IL-SWCNT was quite low compared with other RTIL systems having alkylammonium cation and saturated heterocyclic cation. For example, there is no measureable Pt nanoparticle on the Pt-IL-SWCNT fabricated by using $[C_1C_2Im][Tf_2N]$ (Fig.

2-7), and the Pt content was 1.30 wt %. Considering that imidazolium cation-based RTILs can form an ordered layer-by-layer liquid structure on a solid interface,[144,145] this unexpected result may be caused by the ordered layer structure onto both Pt nanoparticle and SWCNT. Under such condition, a thick RTIL layer between Pt nanoparticle and SWCNT is likely formed, and then it seems to be hard to immobilize the Pt nanoparticle on the SWCNT because fluidity of RTIL inevitably increases with increasing the layer thickness. I believe this is the reason why the unexpected result was obtained in the imidazolium-based RTILs. However, as shown in Table 2-2, the Pt content in the Pt-IL-SWCNT composites produced by imidazolium-based RTILs tended to increase when the alkyl chain on the imidazolium cation became longer. It would be caused by increase in the molecular fluctuation in the cation leading to the destruction of the stable RTIL layer structure on the Pt nanoparticle and the SWCNT. These results support the discussion reported by Endres, *et al.*[146] What is interesting is that our procedure can readily change the amount of the Pt nanoparticle supported on the SWCNT composite and the particle size by just controlling the Pt sputtering condition and/or the RTIL species. The feature is a great advantage for this approach.

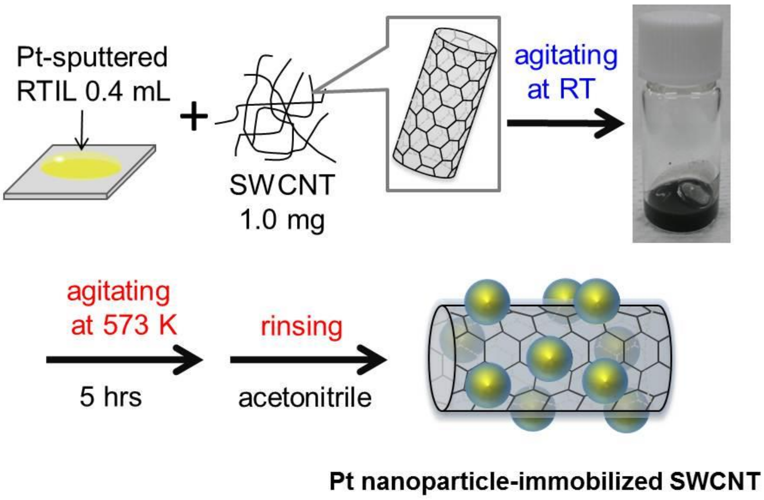

Scheme 2-1. Fabrication method for Pt nanoparticle-immobilized SWCNT composite material used in this investigation.

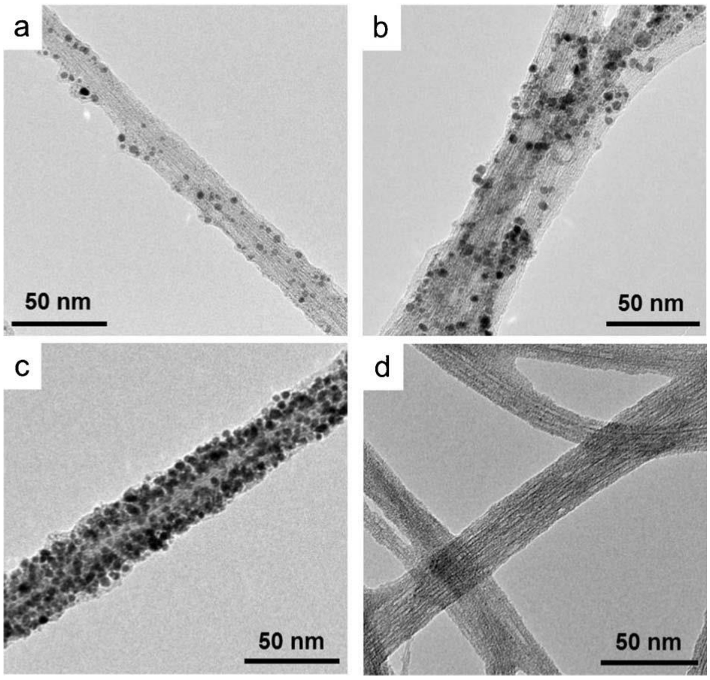

Figure 2-7. TEM images of Pt nanoparticle–SWCNT composite fabricated by Scheme 2-1. The RTIL was (a–c) $[N_{1,1,1,3}][Tf_2N]$ and (d) $[C_1C_2Im][Tf_2N]$. The sputtering time was (a) 300 sec, (b) 600 sec, and (c, d) 900 sec.

Table 2-1. Summary of Pt nanoparticle prepared in $[N_{1,1,1,3}][Tf_2N]$ by RTIL–magnetron sputtering method and the Pt–SWCNT fabricated from the Pt-dispersed RTILs

Sputtering time (sec)	Mean particle size in sputtered RTIL (nm)[a]	Pt concentration in sputtered RTIL (mmol L-1)[b]	Mean particle size on SWCNT (nm)[a]	Pt content in Pt–SWCNT (wt %)[b]
300	2.3	8.2	3.5	11.8
600	2.3	16.3	3.2	28.4
900	2.4	21.6	3.5	32.0

[a] Estimated by TEM observation. [b] Calculated from ICP-AES measurement.

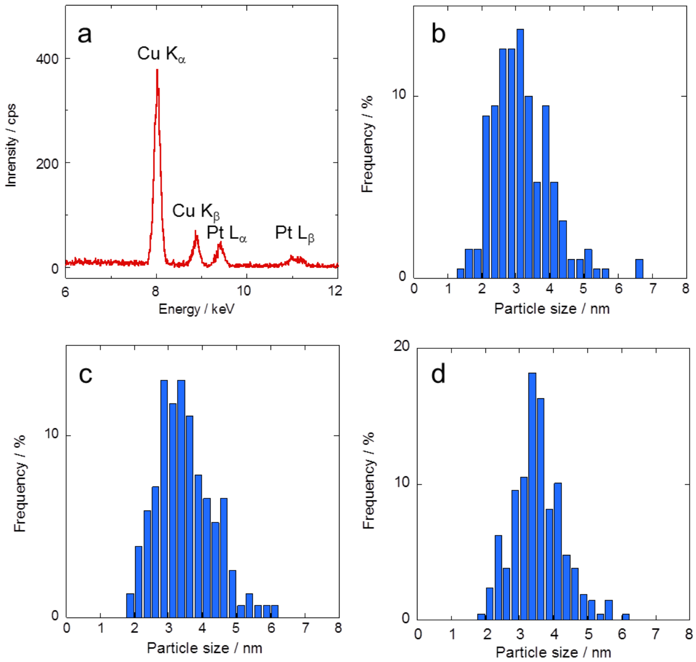

Figure 2-8. (a) EDX spectra of Pt-IL-SWCNT prepared by using Pt-sputtered $[N_{1,1,1,3}][Tf_2N]$. The Cu intensity is derived from a Cu grid used for TEM observation. (b-d) Size distribution diagrams of Pt nanoparticles on Pt-IL-SWCNT composite. The Pt-sputtered RTIL was $[N_{1,1,1,3}][Tf_2N]$. The sputtering time was (b) 300 sec, (c) 600 sec, and (d) 900 sec.

Table 2-2. Mean particle size of the Pt nanoparticles and the Pt loading amount on SWCNT[a]

RTILs	Particle size in sputtered RTIL (nm)[b]	Particle size on SWCNT (nm)[b]	Pt loading amount on SWCNT (wt%)[c]
$[N_{1,1,1,3}][Tf_2N]$	2.4	3.5	32.0
$[N_{2,2,2,5}][Tf_2N]$	1.4	2.6	23.6
$[N_{4,4,4,1}][Tf_2N]$	1.7	3.1	21.1
$[Pyr_{1,3}][Tf_2N]$	1.7	3.4	29.7
$[Pyr_{1,4}][Tf_2N]$	1.4	3.0	16.0
$[Pyr_{1,1o1}][Tf_2N]$	1.6	2.8	17.7
$[C_1C_2Im][Tf_2N]$	-[d]	-[d]	1.30
$[C_2C_{Allyl}Im][Tf_2N]$	1.8	2.3	2.89
$[C_6dimeIm][Tf_2N]$	1.9	3.1	5.01

[a] Sputtering time was 900 sec. [b] Estimated by TEM observation. [c] Calculated from ICP-AES measurement. [d] We could not estimate these values precisely, because they were very fine particles not exceeding 1.00 nm in diameter.

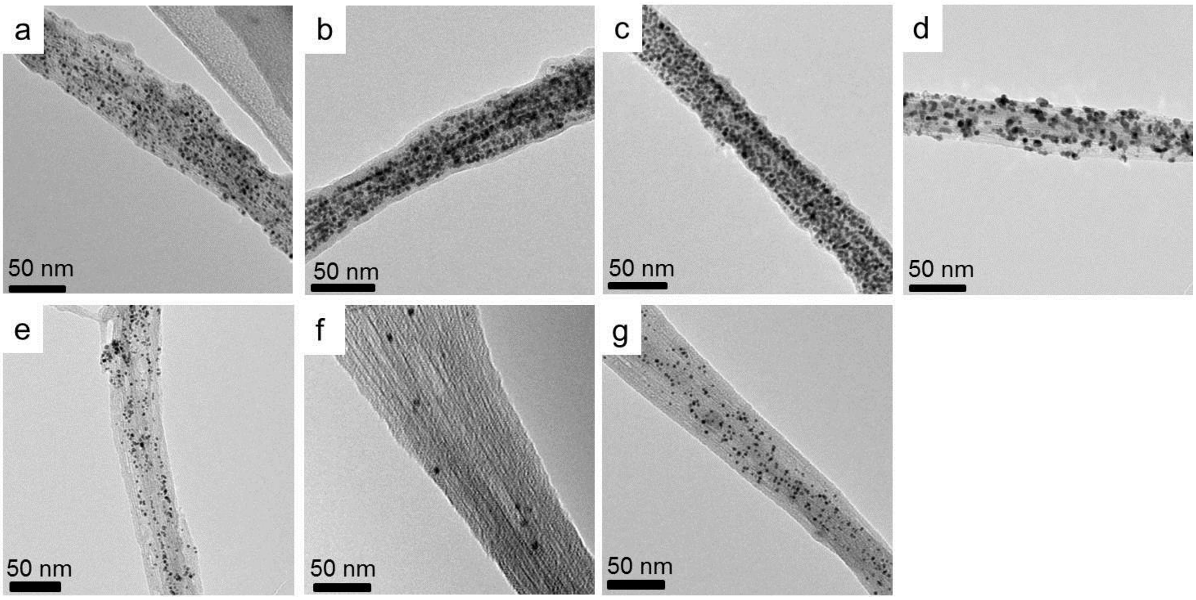

Figure 2-9. TEM images of Pt-IL-SWCNT composite prepared by using various RTILs. The RTILs were (a) [$N_{2,\,2,\,2,\,5}$][Tf_2N], (b) [$N_{4,\,4,\,4,\,1}$][Tf_2N], (c) [$Pyr_{1,\,3}$][Tf_2N], (d) [$Pyr_{1,\,4}$][Tf_2N], (e) [$Pyr_{1,\,1O1}$][Tf_2N], (f) [$C_2C_{Allyl}Im$][Tf_2N], and (g) [C_6dimIm][Tf_2N].

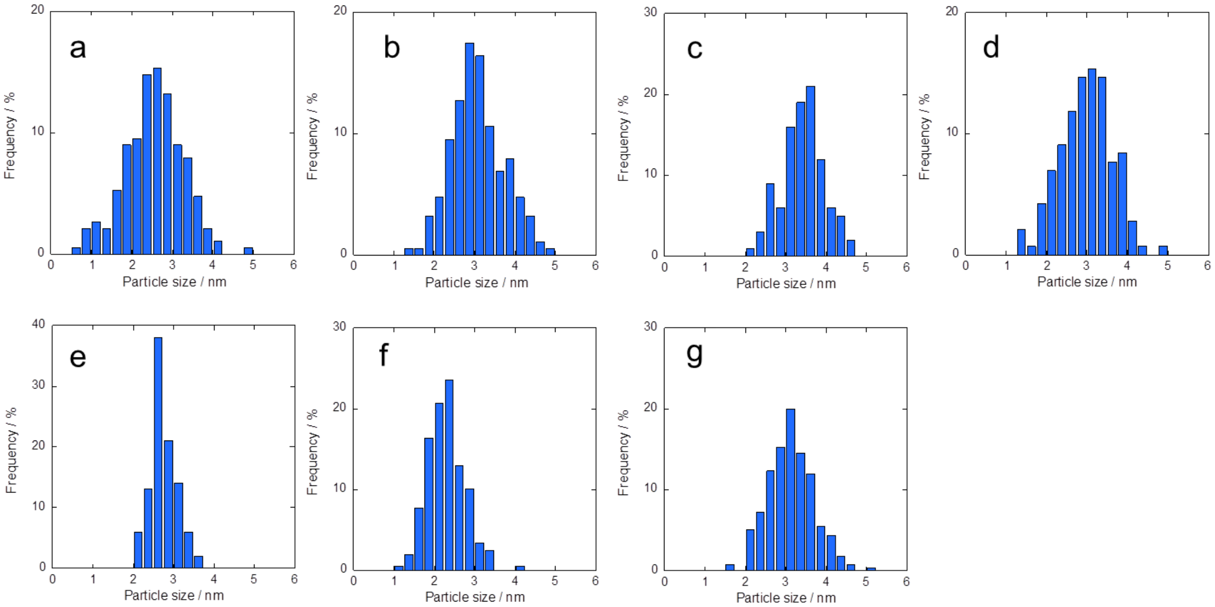

Figure 2-10. Size distribution diagrams of Pt nanoparticles on Pt-IL-SWCNT composite prepared by using various Pt-sputtered RTILs. The RTILs were The RTILs were (a) [$N_{2,\,2,\,2,\,5}$][Tf_2N], (b) [$N_{4,\,4,\,4,\,1}$][Tf_2N], (c) [$Pyr_{1,\,3}$][Tf_2N], (d) [$Pyr_{1,\,4}$][Tf_2N], (e) [$Pyr_{1,\,1O1}$][Tf_2N], (f) [$C_2C_{Allyl}Im$][Tf_2N], and (g) [C_6dimIm][Tf_2N].

Because a facile approach to immobilize metal nanoparticles onto sp^2 carbon nanomaterials including CNT and graphene is strongly required in various fields, it is considerably important to clarify the driving force for the Pt-IL-SWCNT composite material fabrication reported in this article, in terms of design for future functional materials composed of metal nanoparticle and sp^2 carbon nanomaterials. I utilized X-ray photoelectron spectroscopy to reveal the driving force and investigated the interactions in the Pt-IL-SWCNT composite material. Fig. 2-11 exhibits XPS spectra of neat $[N_{1,1,1,3}][Tf_2N]$, Pt nanoparticle-dispersed $[N_{1,1,1,3}][Tf_2N]$ prepared by the magnetron sputtering method, and Pt-IL-SWCNT fabricated from the Pt-dispersed RTIL. In the case of neat RTIL, there is no XPS valence band for Pt (Fig. 2-11a). As to the Pt nanoparticle-dispersed RTIL, XPS peaks related to platinum appeared at 73.3 (Pt $4f_{7/2}$) and 76.4 eV (Pt $4f_{5/2}$). These values were well accorded with the binding energies for Pt(II), not Pt(0). In fact, several research groups have already reported that Pt nanoparticles prepared in RTIL have a minimal positive charge on the nanoparticle surface and the charged Pt nanoparticle is stabilized with anions in the RTIL.[64,82,147] The anomalous spectrum obtained by our XPS analysis supports it. After fabrication of the Pt-IL-SWCNT, the peaks shifted to lower binding energy, 71.1 (Pt $4f_{7/2}$) and 74.4 eV (Pt $4f_{5/2}$). These peaks were attributed to Pt(0), suggesting that Pt nanoparticle exists on the SWCNT as a metal state. Fig. 2-11b and 2-11c show XPS spectra associated with N 1s and F 1s, respectively. The XPS spectra for N 1s and F 1s observed in neat $[Me_3PrN][Tf_2N]$ is confusingly similar to those in the Pt nanoparticle-dispersed RTIL. However, with regard to the Pt-IL-SWCNT composite, XPS peak for N 1s spectrum at 403 eV, which is due to cationic species in RTIL,[148] shifted to higher binding energy, and that for F 1s spectrum moved to lower binding energy relative to other two samples. It indicates that there is a strong interaction between N atom in $[N_{1,1,1,3}]^+$ and F atom in $[Tf_2N]^-$ although the Pt-IL-SWCNT was rinsed in dry acetonitrile thoroughly to remove RTIL. These results imply that the remaining RTIL plays a key role to immobilize Pt nanoparticle on SWCNT surface.[149,150] Given both the XPS results obtained in this study and the fact that cationic species in RTIL interact with π electron cloud on the SWCNT surface, I can give a plausible model on the Pt-IL-SWCNT fabrication as shown in Fig. 2-12. I believe that RTIL exists as nanoglue in between Pt nanoparticle and SWCNT. Thus, the Pt-IL-SWCNT composite would be fabricated without any pretreatment process for SWCNT.

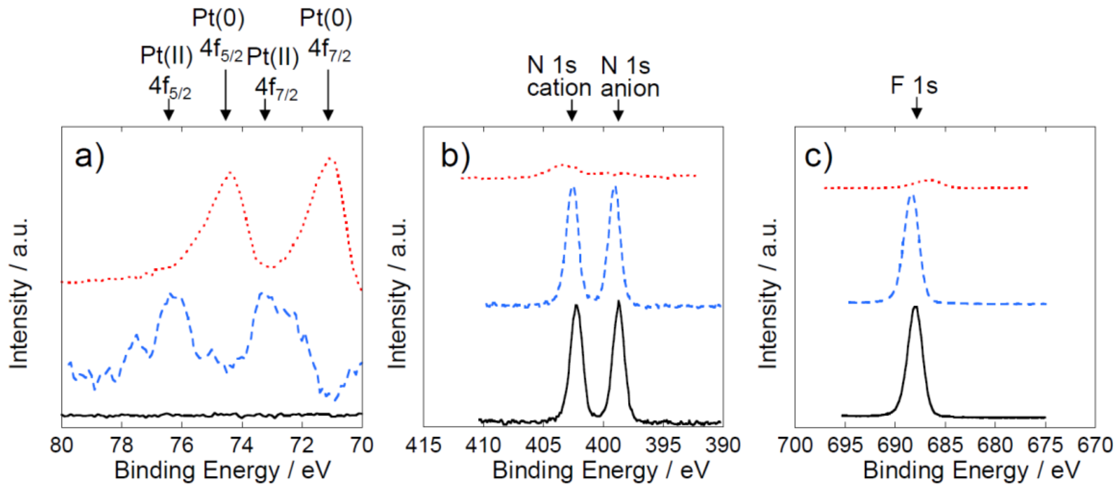

Figure 2-11. XPS spectra of (a) Pt 4f, (b) N 1s, (c) F 1s of (——) neat $[N_{1,1,1,3}][Tf_2N]$, (– – –) Pt-sputtered $[N_{1,1,1,3}][Tf_2N]$ and (•••) Pt-IL-SWCNT.

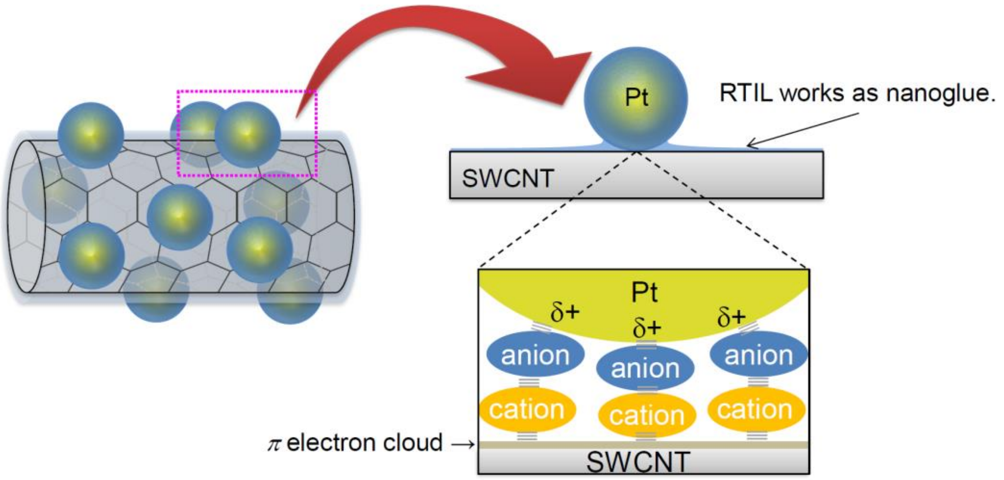

Figure 2-12. Schematic illustration of Pt-IL-SWCNT composite material fabricated in this study.

Metal nanoparticle–CNT composite material is expected to be a next-generation electrode catalyst for polymer electrolyte fuel cell (PEFC). There are many papers on electrocatalytic characteristics of metal nanoparticle–SWCNT composite.[151] I examined electrocatalytic activities of the Pt-IL-SWCNT prepared by the method depicted in Scheme 2-1 to oxygen reduction reaction (ORR). The loading amounts of Pt-SWCNT were 7.1 wt%, 16.0 wt%, 24.1 wt% and 32.9 wt%, respectively. The Pt–SWCNT modified GC disk (Pt-IL-SWCNT/GC) electrode was prepared by the method described in Experimental Details. The prepared Pt-IL-SWCNT working electrode was pretreated with multiple potential scans between 0.10 and +1.25 V (vs. RHE) in 0.1 M $HClO_4$ aqueous solution under dry N_2 condition before the electrochemical experiments. Fig. 2-13 shows cyclic voltammograms recorded at the Pt-IL-SWCNT (32.9 wt%)/GC electrode in 0.1 M $HClO_4$ aqueous solution saturated with N_2 or O_2 gas. Under N_2 atmosphere, several characteristic waves appeared at 0.65 to 1.25 V (vs. RHE) and 0.10 to 0.35 V. The former is attributable to oxidation/reduction of Pt atoms on the surface of Pt nanoparticle, and the latter is due to adsorption/desorption of hydrogen atoms onto the Pt nanoparticle. When the voltammetry was conducted in the O_2 atmosphere, a distinctive O_2 reduction wave appeared at negative potential than ca. 0.95 V. Other samples showed almost same electrochemical behavior. Further investigation was carried out by means of hydrodynamic voltammetry using a rotating ring-disk electrode in order to elucidate whether the O_2 reduction proceeds by a useful four-electron reduction process.[152] From the voltammograms shown in Fig. 2-14, the onset potential of ORR became positive with increasing the Pt loading amount on SWCNT. And also, the reaction is determined precisely by an appropriate electroanalytical chemistry technique. Fig. 2-15 presents a generation rate of H_2O_2 that was yielded by a two-electron ORR. Lower H_2O_2 generation rate means that the ORR predominantly proceeds via a four-electron O_2 reduction reaction. In the case of 24.1 wt% and 32.9 wt% Pt loading SWCNT, the estimated H_2O_2 generation rate was close to 0 % at ca. 0.68 to 0.85 V.

At potentials where O_2 reduction current was reached to the diffusion-limited current, H_2O_2 production was recognized, but the H_2O_2 generation rates maintained low values that were below 7% even at 0.15 V. This result shows that the Pt–SWCNT with high Pt loading amount has a favorable electrocatalytic activity for ORR.

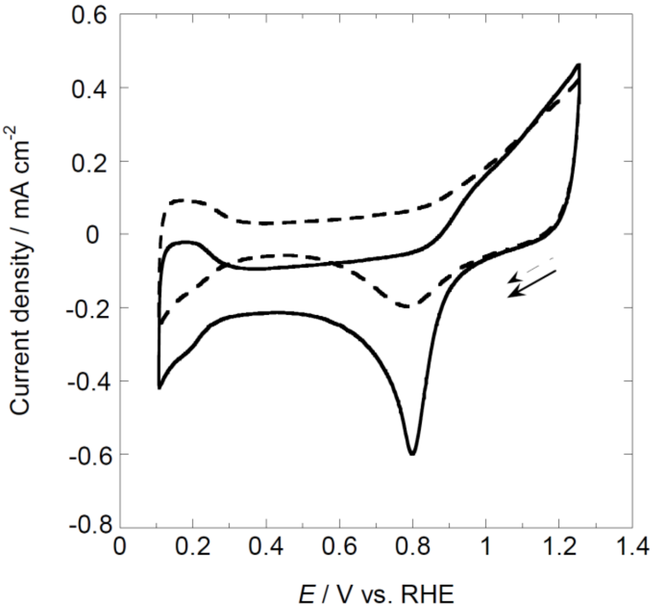

Figure 2-13. Cyclic voltammograms recorded at a Pt-IL-SWCNT modified GC electrode in 0.1 M $HClO_4$ aqueous solution under (- - -) N_2 and (—) O_2 atmosphere. The RTIL used for the Pt nanoparticle preparation was $[N_{1, 1, 1, 3}][Tf_2N]$. The scan rate was 10 mV sec^{-1}.

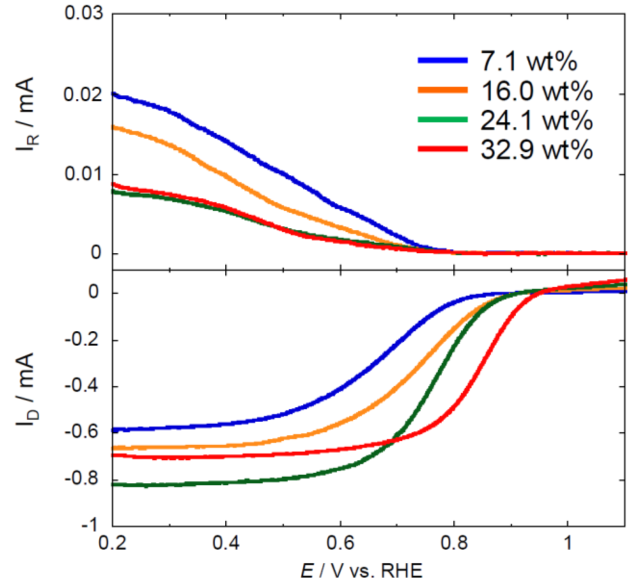

Figure 2-14. Hydrodynamic voltammograms for ORR recorded at a Pt-IL-SWCNT modified rotating ring-disk electrode in O_2-saturated 0.1 M $HClO_4$ aqueous solution at 298 K. The electrodes were (top) Pt ring and (bottom) Pt-IL-SWCNT modified GC disk. The RTIL used for Pt nanoparticle preparation was $[N_{1,1,1,3}][Tf_2N]$. The potential for the ring electrode was 1.20 V. The scan rate was 10 mV s^{-1}. The rotation rate was 1200 rpm. Pt loading amount was (—)7.1 wt%, (—)16.0 wt%, (—)24.1 wt% and (—)32.9 wt%.

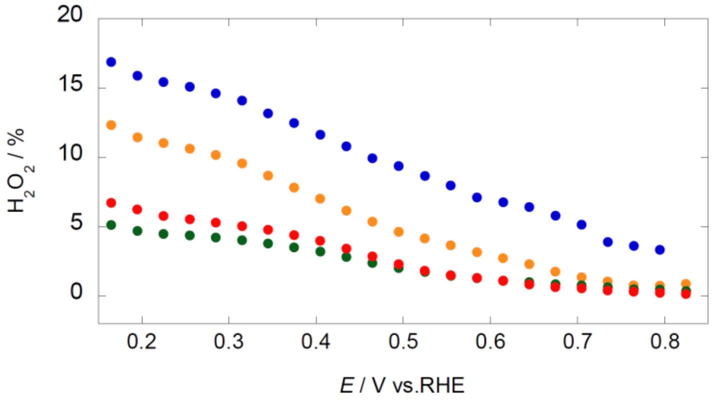

Figure 2-15. Hydrogen peroxide generation rate determined by hydrodynamic voltammetric method at different applied potentials. The data was constructed from Fig. S7. Pt loading amount was (●)7.1 wt%, (●)16.0 wt%, (●)24.1 wt% and (●)32.9 wt%.

2-4. Conclusions

The Pt nanoparticles obtained by the ionic liquid-sputtering method using $[N_{1,1,1,3}][Tf_2N]$ had mean particle size of ca. 2.3 ~ 2.4 nm independently of the sputtering time. The Pt-GCE prepared with the Pt-sputtered RTIL and a glassy carbon plate showed oxygen reduction activity but the activity varied with the preparation condition for the Pt-GCE. The $[N_{1,1,1,3}][Tf_2N]$ modified Pt-GCE had better catalytic ability to ORR than the original Pt-GCE and never showed CO poisoning behavior.

I also succeeded in the establishment of the facile Pt nanoparticle–SWCNT composite fabrication method. I found that RTIL can work as nanoglue for sticking Pt nanoparticle against SWCNT. Interestingly this approach enabled variations in the amount of Pt nanoparticle and Pt particle size supported on the Pt-IL-SWCNT composite by changing the sputtering time and/or RTIL species in the Pt sputtering process. These features are a great advantage for this approach. In addition, the Pt-IL-SWCNT composite had a promising catalytic activity for electrochemical ORR.

Chapter 3

Electrocatalytic Durability of Pt Nanoparticle-supported Carbon Composite Materials Prepared by Ionic Liquid-Sputtering Method

3-1. Introduction

Polymer electrolyte fuel cells (PEFCs) are attractive energy source for mobile and stationary applications because of their higher energy conversion efficiency and environmental friendliness.[153–155] Nevertheless, the cost and durability are big hurdles for practical applications and further improvement. In the PEFCs, fine Pt nanoparticles supported carbon black such as Ketjen Black EC and Vulcan XC-72 is used as the catalyst of the cathode layer due to their low cost and higher electronic conductivity.[156] Among various factors of PEFC degradation, the degradation of Pt catalysts due to the electrochemical corrosion of carbon support at the positive electrode is one of the most serious problems for continual operation.[157–160] The corrosion of carbon support is in particular accelerated during the start-up and shut-down operations because the local cathode potential can reach to as high as 1.5 V.[161] When the carbon is oxidized to carbon dioxide and carbon monoxide under the high voltage, it provokes the aggregation and migration of Pt nanoparticles as well as detachment from the carbon support.

To improve the durability of Pt catalyst, there has been considerable research in the past few decades.[156,159,162–169] Among them, novel carbon materials such as carbon nanotubes[163,164], carbon nanocages,[165] graphene,[166,167] and so on.[168,169] have been studied as the catalyst support. These are considered as attractive candidates because of the high surface area, corrosion resistance, and special electronic and mechanical properties. But it is difficult to support Pt nanoparticles onto them due to the inertness of their surface. In cases where adsorption of Pt nanoparticles are capable, the employed methods lose a part of the origin property of the carbon materials during their pretreatments.[134]

It was described that Pt nanoparticles prepared by ionic liquid-sputtering method are easily immobilized onto single-walled carbon nanotube (SWCNT) without laborious pretreatment or any chemical reagents, and that obtained Pt nanoparticle-supported SWCNT is electrochemically active. In this chapter, results obtained by the durability test of the Pt nanoparticle-supported carbon materials prepared ionic liquid-sputtering method are shown. The durability was mainly examined by accelerated potential cycling tests.

3-2. Experimental section

3-2-1. Materials

The RTIL, *N*,*N*,*N*-trimethyl-*N*-propylammonium bis(trifluoromethanesulfonyl)amide ($[N_{1,1,1,3}][Tf_2N]$), was in ultrapure grade purchased from Kanto Chemical Co., Inc. This RTIL was purified by washing with water several times and dried under vacuum condition prior to use. Single-walled carbon nanotube (SWCNT) and carbon black (CB) (Vulcan® XC-72) were purchased from Meijo Nano Carbon Co., Inc. and Cabot Co., respectively. Ethylene glycol (99.5 +%) and $NaBH_4$ (95.0 +%) were purchased from Wako Pure Chemical Industries, Ltd. $Na_2PtCl_6 \cdot 6H_2O$ (98.0%) and Nafion® solution (5 wt%) were purchased from Sigma-Aldrich Co. LLC. TEC10V30E, which is commercially available Pt nanoparticle-supported carbon catalyst, was purchased from Tanaka Kikinzoku Kogyo K. K. Except the RTIL, all chemicals were used as received.

3-2-2. Preparation of Pt nanoparticles-supported carbon materials

The soda glass (2.5 cm × 2.5 cm), on which $[N_{1,1,1,3}][Tf_2N]$ (0.4 mL) was spread, was put in a Cressington108 auto SE sputter coater. A polycrystalline Pt plate target (ϕ 5.7 cm, 99.98%) was placed on 4.5 cm above the glass plate. Sputter deposition onto $[N_{1,1,1,3}][Tf_2N]$ was conducted with sputter current of 40 mA in dry Ar (99.999%) atmosphere whose pressure did not exceed 7 ± 1 Pa. The sputtering was carried out by direct current (DC) mode at room temperature (298 ± 2 K).

Appropriate quantities of SWCNT or CB were mixed with 0.4 mL of Pt-sputtered $[N_{1,1,1,3}][Tf_2N]$ in a vial and agitated for 10 hrs to make homogeneous dispersion state. The resulting mixture was heated at 573 K for 5 hrs. Obtained products, Pt-IL-SWCNT and Pt-IL-CB, were washed with acetonitrile several times, followed by vacuum drying for a few hours in vacuo.

Chemical oxidation of SWCNT was conducted by immersing SWCNT in H_2SO_4/HNO_3 mixture (3:1 volumetric ratio) for 10 hrs at 338 K. The oxidized SWCNT was filtered, washed with deionized water several times, and dried. Ethylene glycol was used as a stabilizer for Pt nanoparticle. All reactions described below in this section were carried out under nitrogen atmosphere. Ethylene glycol (25 g) was mixed with $NaBH_4$ (0.6 g) slowly, followed by agitating for 2 hrs at room temperature. The mixed solution was gradually added to the suspension containing ethylene glycol (25 mL), $Na_2PtCl_6 \cdot 6H_2O$ (0.205 g), and the oxidized SWCNT (0.1 g), followed by agitating for 4 h at 338 K. To neutralize the solution, 0.2 M HCl aqueous solution (15 mL) was added slowly and agitated for 3 h. The obtained Pt nanoparticle-adsorbed oxidized SWCNT (Pt-SWCNT) was washed with ultrapure water and collected by centrifuge. After vacuum-freeze drying, Pt-SWCNT was used for measurements. The Pt loading was 30.3 wt%.

3-2-3. Characterization

Information of size distribution of Pt nanoparticles and the morphology of carbon support were obtained by observation of the prepared samples with a Hitachi H-7650 transmission electron microscope (TEM) operated at 100 kV. The sample grids for the TEM observation were prepared by placing one drop of *i*-propanol solution involving the sample onto a cupper grid coated with an amorphous carbon thin layer. Pt amount of the carbon composite was identified by a Shimadzu ICPS-7510 induced coupled plasma spectrometer (ICP-AES). The carbon composites were dissolved in a hot aqua regia and the obtained solution was used for the ICP-AES measurement.

3-2-4. Electrochemical experiments

Electrocatalytic activities of Pt nanoparticle-supported carbon materials prepared in this study was examined with a Hokuto Denko HZ-7000 potentiostat/galvanostat controlled with a laptop computer. The electrochemical experiments were conducted by a three-electrode cell at room temperature. A glassy carbon (GC) rotating disk electrode (surface area: 0.196 cm^2, Pine Instruments) was used as the working electrode. The GC electrode was polished to a mirror gloss with 0.06 μm alumina suspension before each measurement. The ink was produced by ultrasonically dispersing 1.0 mg of Pt-carbon (Pt-IL-SWCNT, Pt-IL-CB, Pt-SWCNT, and TEC10V30E) in *i*-propanol (0.2 mL) for 30 min. 5 μL of the ink was spread onto GC and the *i*-propanol in the ink was slowly evaporated in the air. Then, the GC disk was covered with 5 μL of Nafion® solution (0.2 wt%) diluted with *i*-propanol to fix the catalyst on GC robustly. The obtained working electrode was set in a Pine Instruments AFMSRCE electrode rotator for the measurements. A Pt mesh was used for counter electrode. The Ag/AgCl double-junction electrode immersed in saturated-KCl aqueous solution was used as a reference electrode. All potential values in this chapter are referred to reverse hydrogen electrode (RHE). 0.1 M $HClO_4$ aqueous solution was used as electrolyte. Before the measurement of their electrocatalytic activities, the working electrode was subjected to 50 cycles of potential sweep at 50 mV s^{-1} between 0.05 and 1.2 V vs. RHE under nitrogen atmosphere to get the stable and reproducible voltammogram. The electrochemical surface area (ECSA) of Pt was determined by hydrogen adsorption or desorption coulombic charge in the cyclic voltammogram under nitrogen atmosphere after subtracting double layer charge current,. The value of ECSA was calculated from the equation given by

$$\mathrm{ECSA} = \frac{Q_H \times 10^2}{210 \times M_{Pt}}$$

where Q_H (μC) is the charge of hydrogen adsorption/desorption. The value of 210 ($\mu\mathrm{Ccm}^{-2}$) is an average value for the charge associated with monolayer surface formation of hydrogen on a smooth polycrystalline platinum. M_{Pt} (μg) is the Pt amount on GC working electrode.

The degradation behavior of Pt nanoparticle-supported carbon materials was evaluated by employing the standard degradation test recommended by FCCJ.[170] The method simulates overload condition at start and stop of a fuel cell by applying potential sweep between 1.0 and 1.5 V vs. RHE at 500 mVs^{-1} and defined 2 s of operation as a 1 cycle. All the measurements were conducted under nitrogen atmosphere at room temperature.

3-3. Results and discussion

The morphologies of the prepared Pt-supported carbon and commercial catalyst were observed by TEM, as shown in Figure 3-1. Adsorption of lots of Pt nanoparticles was confirmed on the surface of the carbon support at each sample. The mean particle sizes of Pt nanoparticles adsorbed on the carbon support given in Figure 3-1(a) to (d) are, respectively, 3.4 nm, 2.8 nm, 3.6 nm and 2.6 nm.

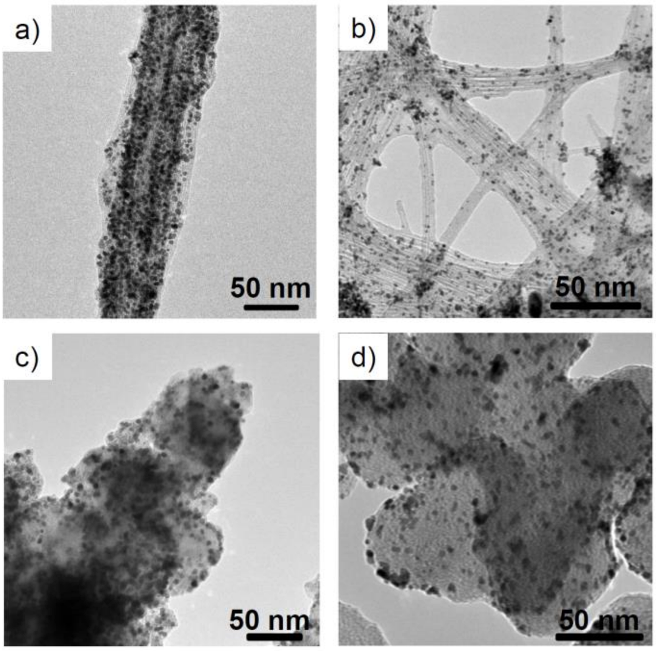

Figure 3-1. TEM images of (a) Pt-IL-SWCNT, (b) Pt-SWCNT, (c) Pt-IL-CB and (d) TEC10C30E freshly prepared.

Durability of Pt nanoparticle-supported carbon catalyst was examined by the potential cycle test between 1.0 and 1.5 V (vs. RHE). Figure 3-2 shows the changes in cyclic voltammograms (CVs) for four different catalysts taken in 0.1 M $HClO_4$ solution deaerated with N_2 at room temperature. All the catalysts showed the hydrogen adsorption and desorption peaks at potentials ranging between 0.10 and 0.35 V and Pt-oxide formation and reduction peaks at potentials ranging between 0.80 and 1.2 V. As well known, a couple of peaks appeared at around 0.6 V in CV for carbon materials is assignable to redox reaction of quinone and hydroquinone moiety, indicating generation of oxidized carbon on the carbon support during the potential cycling tests.[171] Although the peak derived from oxidized carbon were increased after the potential cycle test for each catalyst, significant decrease of the hydrogen adsorption and desorption peaks was not recognized for Pt-IL-SWCNT and Pt-IL-CB (Figure 3-2 (a) and (c)), which were contrast to the results obtained from

Pt-SWCNT and TEC10V30E (Figure 3-2 (b) and (d)) indicating large decrease of the peaks due to the hydrogen adsorption and desorption.

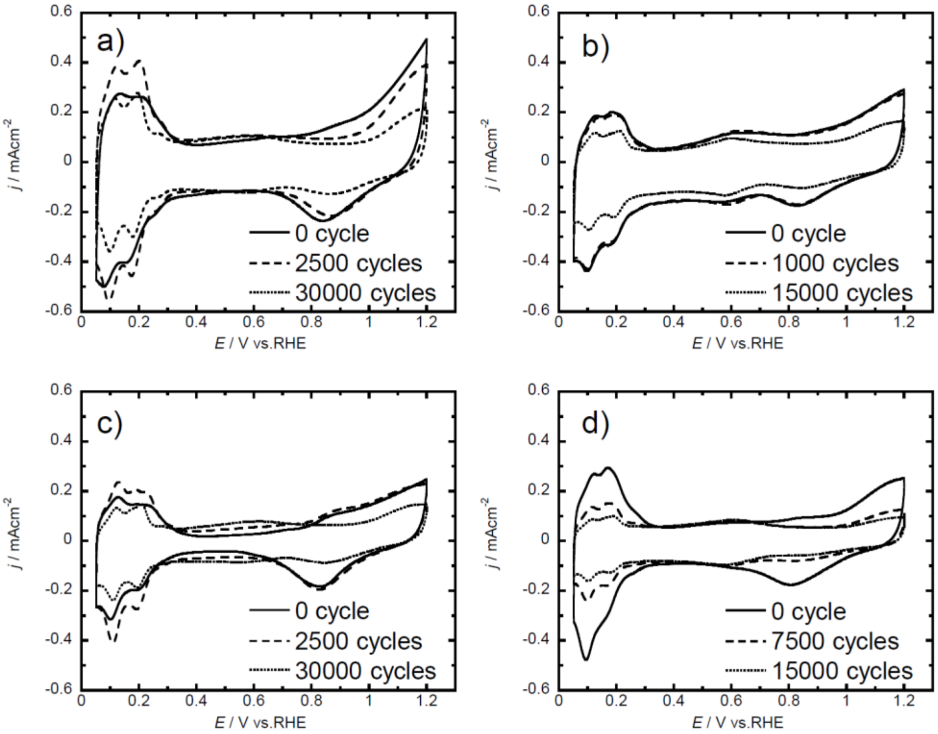

Figure 3-2. Cyclic voltammograms of (a) Pt-IL-SWCNT, (b) Pt-SWCNT, (c) Pt-IL-CB and (d) TEC10V30E during the potential cycle test. The cyclic voltammograms were recorded in N_2 saturated in 0.1 M $HClO_4$ solution at room temperature with the scan rate of 10 mV s^{-1}.

The changes in electrochemical surface areas (ECSAs) of different catalysts as a function of cycle number during the potential cycle test are shown in Figure 3-3(a). Pt-IL-SWCNT and Pt-IL-CB showed increase in ECSAs in initial several thousand cycles. Such the behavior is more obvious from Figure 3-3(b) which plots ECSAs that are normalized to each maximum value. This is probably due to the crystallization of Pt nanoparticles with ordering by sintering during the potential cycle test. Initial and maximum ECSA, ECSA after potential cycle test, and retention ratio were calculated for each catalyst and are summarized in Table 3-1. Retention ratio at after 15000 cycles decreased in the following order; Pt-IL-SWCNT > Pt-IL-CB > Pt-SWCNT > TEC10V30E. Pt-IL-SWCNT showed the highest maximum ECSA and better durability than Pt-SWCNT, suggesting that the oxidative treatment influences their property. As a matter of fact, the pristine SWCNT surface composed of only sp^2 carbon is known to be more chemically stable than the surface of the oxidized SWCNT. What makes the result even more interesting is that Pt-IL-CB showed the higher retention ratio compared with Pt-SWCNT. In general, the corrosion of CB is thought to take place easily during potential cycle test as seen in TEC10V30E because of the presence of functional groups at the carbon surfaces. It is then strongly suggested that RTILs existed at the catalyst prevent or delay the corrosion of carbon support. In comparison with the retention ratio after 30000 cycles, Pt-IL-SWCNT exhibits better value than Pt-IL-CB. This outcome is derived from the difference of origin nature between SWCNT and CB.

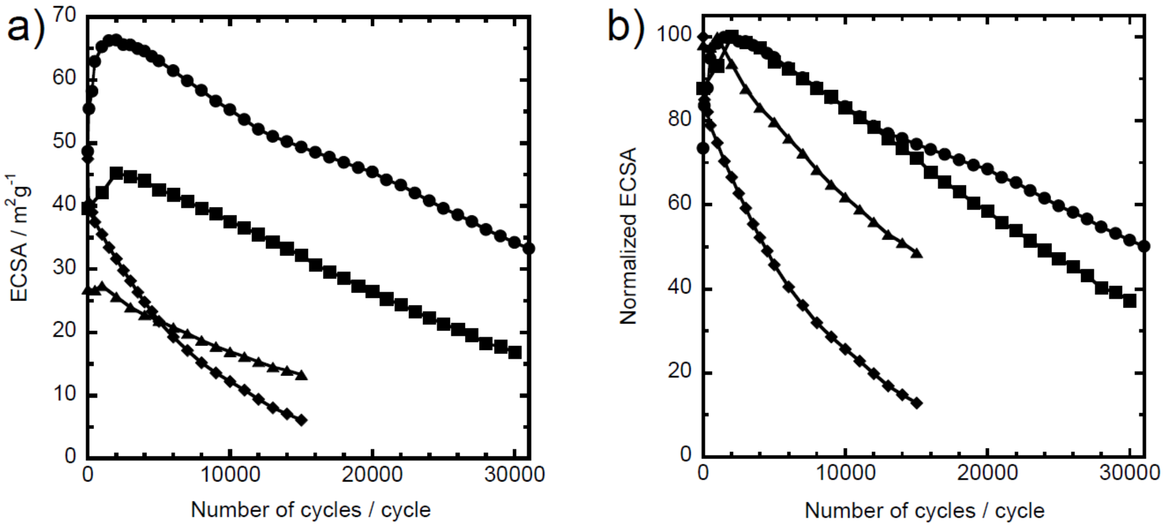

Figure 3-3. Change in (a) ECSA and (b) normalized ECSA during the potential cycle test for (●）Pt-IL-SWCNT, (▲) Pt-SWCNT, (■）Pt-IL-CB and (◆) TEC10V30E.

Table 3-1. The variation of electrochemical surface area (ECSA)

Catalyst	Initial ECSA (m^2g^{-1})	Max. ECSA (m^2g^{-1})	ECSA after durability test (m^2g^{-1})	Retention ratio of ECSA [a)]
Pt-IL-SWCNT	48.7	66.3	39.2[b)]	74.4 %[c)], 51.6% [b)]
Pt-SWCNT	26.8	27.4	13.3[c)]	48.6% [c)]
Pt-IL-CB	39.7	45.3	16.8[b)]	71.1% [c)], 37.2% [b)]
TEC10V30E	47.5	47.5	6.1[c)]	12.8% [c)]

a) The value was calculated using maximum ECSA listed in this table. b) The value after 30000 cycles and c) after 15000 cycles.

It is essential to analyze the changes in morphology of catalysts after the potential cycle test. Figure 3-4 shows TEM images for Pt-IL-SWCNT, Pt-SWCNT, Pt-IL-CB and TEC10V30E after the potential cycle test, indicating a big difference of morphology between the samples using RTILs or not. In TEM images of Pt-IL-SWCNT and Pt-IL-CB, it is clearly seen that Pt nanoparticles remain on the carbon support with small quantity of aggregation. The large aggregate of Pt nanoparticles is confirmed for Pt-SWCNT. Furthermore, the corrosion of carbon support and detachment of Pt nanoparticles are seen for TEC10V30E. Based on these results, it is considerable that RTILs exist at the catalyst play an important role for maintaining Pt nanoparticles onto carbon support during potential cycling test.

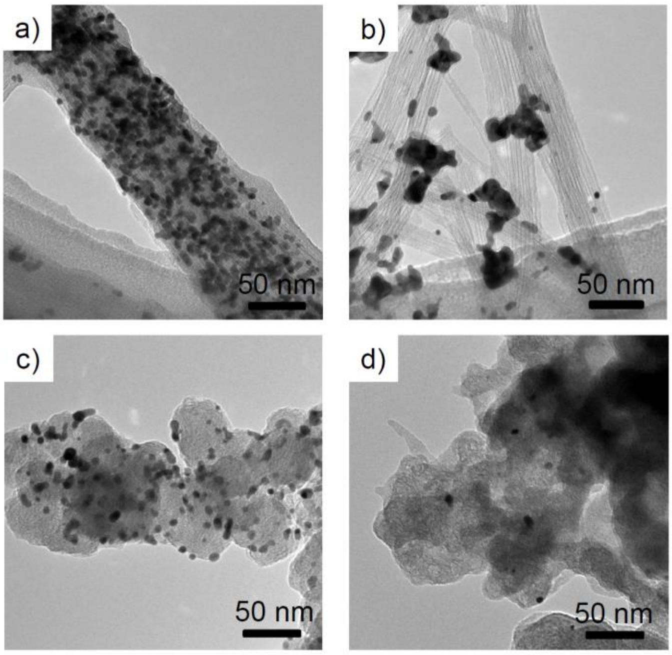

Figure 3-4. TEM images of (a) Pt-IL-SWCNT, (b) Pt-SWCNT, (c) Pt-IL-CB and (d) TEC10C30E after the potential cycle test.

To clarify the effect of RTILs on the carbon support, [$N_{1,\ 1,\ 1,\ 3}$][Tf_2N]-modified TEC10V30E (TEC10V30E-IL) was prepared by mixing the carbon catalyst and the RTIL with heating at 573 K, the way of which was similar to the preparation of Pt-IL-CB mentioned in the experimental section. The changes in CVs during the potential cycle test for TEC10V30E-IL and the changes in the normalized ECSA with that of TEC10V30E are shown in Figure 3-5(a) and (b), respectively. The hydrogen adsorption and desorption peaks decreased with an increase in the potential cycles. In comparison with TEC10V30E about the change of ECSA, the apparent difference of decrease rate is seen at initial hundred cycles but it showed almost the same tendency in the decrease of ECSA with TEC10V30E. This result indicates that mixing of RTIL with as-prepared Pt supported catalyst is ineffective to prevent the degradation of the catalyst. This result also supports the desirable effect of RTIL existed between Pt nanoparticles and carbon support in the catalyst prepared by ionic liquid-sputtering method.

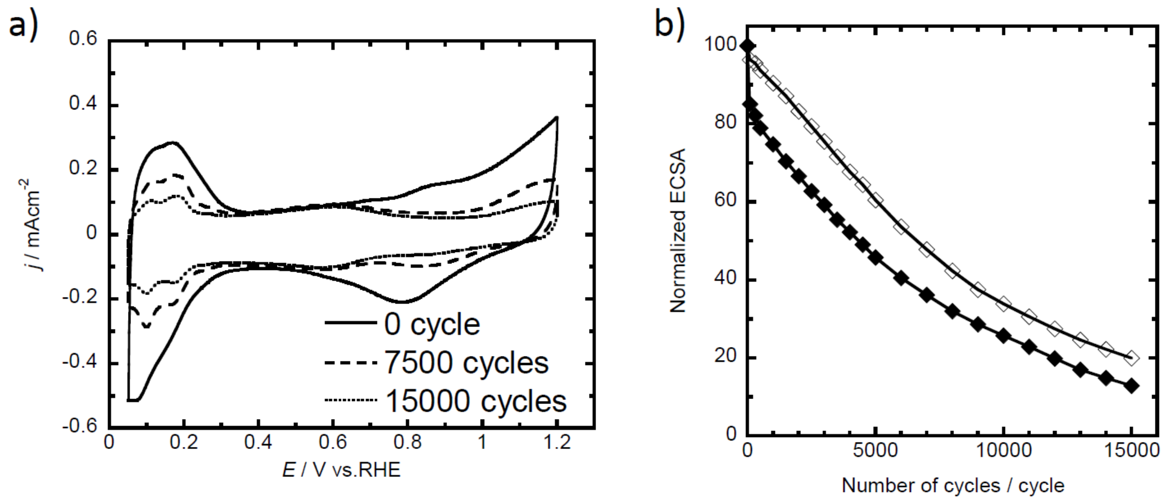

Figure 3-5. (a) Cyclic voltammograms of TEC10V30E-IL and (b) change in normalized ECSA during the potential cycle test for (◇) TEC10V30E-IL and (◆) TEC10V30E. The cyclic voltammograms were recorded in N_2 saturated in 0.1 M $HClO_4$ solution at room temperature with the scan rate of 10 mV s^{-1}.

3-4. Conclusion

I investigated the durability of Pt nanoparticle-supported carbon materials prepared by ionic liquid-sputtering method using the potential cycle test between 1.0 V and 1.5 V vs. RHE. Pt nanoparticle-supported single-walled carbon nanotube (Pt-IL-SWCNT) and carbon black (Pt-IL-CB) prepared using ionic liquid showed higher electrochemical durability as compared with catalyst prepared by chemical reduction method. TEM observations revealed that lots of Pt nanoparticles were retained on the carbon support after 30000 cycles of potential cycle test for Pt-IL-SWCNT and Pt-IL-CB. The reason for the high durability is attributable to existence of the RTILs between the carbon support and Pt nanoparticles, which prevents oxidation of the carbon support due to Pt nanoparticles as catalyst. Accordingly the RTIL plays an important role for preventing the corrosion of carbon support and the detachment of Pt nanoparticles.

Summary

In this dissertation, preparation of Pt and Au nanoparticles by ionic liquid-sputtering method and the application of Pt nanoparticles to electrocatalyst were investigated. The effect of room temperature ionic liquid (RTIL) component on the size of metal nanoparticles, electrocatalytic activity and durability of Pt nanoparticles supported carbon materials were discussed in each chapter of this thesis. The main results and conclusions obtained in this study are summarized as follows:

In chapter 1, the physicochemical properties of novel four n-tributylalkylphosphonium cation based RTIL and the effect of RTIL component on the size of Pt and Au metal nanoparticles prepared ionic liquid-sputtering method were described. Pt and Au nanoparticles were prepared in more than 20 types of RTIL including phosphonium cation-based RTILs. It is firstly demonstrated that phosphonium cation-based RTIL can apply for preparation of metal nanoparticles by ionic liquid-sputtering method. Although the particle size was too small to evaluate the correlativity in Pt-sputtered RTIL, the tendency with the viscosity and density was found at Au nanoparticle prepared in imidazolium, pyrrolidinium and ammonium cation-based RTILs with bis(trifluoromethylsulfonyl)amide anion. The formation mechanism of metal nanoparticles was discussed.

In chapter 2, preparation of Pt nanoparticle-supported glassy carbon (GC) and single-walled carbon nanotube (SWCNT) and their electrocatalytic activities in acidic solution have been discussed. Pt nanoparticles prepared by ionic liquid-sputtering method were easily immobilized on GC by heating process. Electrocatalytic activity toward oxygen reduction reaction (ORR) was changed by the temperature for immobilization. Pt

nanoparticle was also immobilized on SWCNT. It is found that RTIL can work as nanoglue for sticking Pt nanoparticle against SWCNT. The amount of Pt nanoparticles and particle size supported on SWCNT were changed by the sputtering time and/or RTIL species. Obtained Pt nanoparticle-supported SWCNT showed a favourable electrocatalytic activity toward ORR.

In chapter 3, the electrochemical durability of Pt nanoparticle-supported carbon catalysts prepared by ionic liquid-sputtering method were described. The durability was examined by potential cycle test between 1.0 V and 1.5 V vs. RHE. Pt nanoparticle-supported single-walled carbon nanotube and carbon black prepared using ionic liquid exhibited higher electrochemical durability as compared with the catalyst prepared by chemical deposition of Pt and commercially available one. TEM observations have clearly revealed that RTIL existed on the catalysts plays an important role for significant improvement of the durability.

List of Publications

1. Oxygen reduction catalytic activity of platinum nanoparticles prepared by room-temperature ionic liquid-sputtering method
   Tetsuya Tsuda, Kazuki Yoshii, Tsukasa Torimoto and Susumu Kuwabata
   Journal of Power Sources, **2010**, *195*, 5980-5985.

2. Platinum nanoparticle immobilization onto carbon nanotubes using Pt-sputtered room-temperature ionic liquid
   Kazuki Yoshii, Tetsuya Tsuda, Takashi Arimura, Akihito Imanishi, Tsukasa Torimoto and Susumu Kuwabata
   RSC Advances, **2012**, *2*, 8262-8264.

3. Physicochemical Properties of Tri-*n*-butylalkylphosphonium Cation-Based Room-Temperature Ionic Liquids
   Kazuki Yoshii, Keisuke Yamaji, Tetsuya Tsuda, Katsuhiko Tsunashima, Hiroyuki Yoshida, Masanori Ozaki and Susumu Kuwabata
   The Journal of Physical Chemistry B, **2013**, 117, 15051-15059.

4. Electrochemical durability of Pt-supported carbon electrocatalysts prepared by ionic liquid-sputtering method
   Kazuki Yoshii, Keisuke Yamaji, Tetsuya Tsuda, Tsukasa Torimoto and Susumu Kuwabata
   in preparation

5. The component effect of ionic liquid on the size of Pt or Au nanoparticles prepared by sputtering deposition
   Kazuki Yoshii, Keisuke Yamaji, Tetsuya Tsuda, Katsuhiko Tsunashima, Tsukasa Torimoto and Susumu Kuwabata
   in preparation

Supplementary Publication

1. Palladium Nanoparticles in Ionic Liquid by Sputter Deposition as Catalysts for Suzuki-Miyaura Coupling in Water
   Yoshiro Oda, Koji Hirano, Kazuki Yoshii, Susumu Kuwabata, Tsukasa Torimoto and Masahiro Miura
   Chemistry Letters, **2010**, *39*, 1069-1071.

References

[1] J. P. Wilcoxon, B. L. Abrams, *Chem. Soc. Rev.* **2006**, *35*, 1162–1194.

[2] L. D. Pachón, G. Rothenberg, *Appl. Organomet. Chem.* **2008**, *22*, 288–299.

[3] A. R. Tao, S. Habas, P. Yang, *Small* **2008**, *4*, 310–325.

[4] Y. Xia, Y. Xiong, B. Lim, S. E. Skrabalak, *Angew. Chem. Int. Ed.* **2009**, *48*, 60–103.

[5] G. Schmit, *Nanoparticles, 2nd edn*, Wiley-VHC, Weinheim, **2010**.

[6] Y. Lu, W. Chen, *Chem. Soc. Rev.* **2012**, *41*, 3594–3623.

[7] D. Astruc, F. Lu, J. R. Aranzaes, *Angew. Chem. Int. Ed.* **2005**, *44*, 7852–7872.

[8] R. Narayanan, M. A. El-Sayed, *J. Phys. Chem. B* **2005**, *109*, 12663–12676.

[9] L. S. Ott, R. G. Finke, *Coord. Chem. Rev.* **2007**, *251*, 1075–1100.

[10] C.-J. Jia, F. Schüth, *Phys. Chem. Chem. Phys.* **2011**, *13*, 2457–2487.

[11] A. Dhakshinamoorthy, H. Garcia, *Chem. Soc. Rev.* **2012**, *41*, 5262–5284.

[12] M. Haruta, *Catal. Today* **1997**, *36*, 153–166.

[13] A. Abad, P. Concepción, A. Corma, H. García, *Angew. Chem. Int. Ed.* **2005**, *44*, 4066–4069.

[14] A. A. Herzing, C. J. Kiely, A. F. Carley, P. Landon, G. J. Hutchings, *Science.* **2008**, *321*, 1331–1335.

[15] R. Sardar, A. M. Funston, P. Mulvaney, R. W. Murray, *Langmuir* **2009**, *25*, 13840–13851.

[16] U. Paulus, T. Schmidt, H. A. Gasteiger, R. J. Behm, *J. Electroanal.* **2001**, *495*, 134–145.

[17] J. Zhang, F. H. B. Lima, M. H. Shao, K. Sasaki, J. X. Wang, J. Hanson, R. R. Adzic, *J. Phys. Chem. B* **2005**, *109*, 22701–22704.

[18] H. A. Gasteiger, S. S. Kocha, B. Sompalli, F. T. Wagner, *Appl. Catal. B Environ.* **2005**, *56*, 9–35.

[19] J. Zhang, K. Sasaki, E. Sutter, R. R. Adzic, *Science.* **2007**, *315*, 220–222.

[20] Z. Peng, H. Yang, *Nano Today* **2009**, *4*, 143–164.

[21] M. Antonietti, D. Kuang, B. Smarsly, Y. Zhou, *Angew. Chem. Int. Ed.* **2004**, *43*, 4988–4992.

[22] P. Migowski, J. Dupont, *Chem. Eur. J.* **2007**, *13*, 32–39.

[23] C. Vollmer, C. Janiak, *Coord. Chem. Rev.* **2011**, *255*, 2039–2057.

[24] K. L. Luska, A. Moores, *ChemCatChem* **2012**, *4*, 1534–1546.

[25] G. Salas, P. S. Campbell, C. C. Santini, K. Philippot, M. F. Costa Gomes, A. A. H. Pádua, *Dalton Trans.* **2012**, *41*, 13919–13926.

[26] J. Dupont, M. R. Meneghetti, *Curr. Opin. Colloid Interface Sci.* **2013**, *18*, 54–60.

[27] P. Lara, K. Philippot, B. Chaudret, *ChemCatChem* **2013**, *5*, 28–45.

[28] C. Janiak, *Zeitschrift für Naturforsch. B* **2013**, *68b*, 1059–1089.

[29] H. Wender, P. Migowski, A. F. Feil, S. R. Teixeira, J. Dupont, *Coord. Chem. Rev.* **2013**, *257,* 2468–2483.

[30] M. Galinski, A. Lewandowski, I. Stepniak, *Electrochim. Acta* **2006**, *51,* 5567–5580.

[31] V. I. Pârvulescu, C. Hardacre, *Chem. Rev.* **2007**, *107,* 2615–2665.

[32] N. V. Plechkova, K. R. Seddon, *Chem. Soc. Rev.* **2008**, *37,* 123–150.

[33] P. Hapiot, C. Lagrost, *Chem. Rev.* **2008**, *108*, 2238–2264.

[34] F. Endres, A. P. Abbott, D. R. MacFarlane, *Electrodeposition from Ionic Liquids,* Wiley-VCH, Weinheim, **2008**.

[35] M. Armand, F. Endres, D. R. MacFarlane, H. Ohno, B. Scrosati, *Nat. Mater.* **2009**, *8*, 621–629.

[36] S. Kuwabata, T. Tsuda, T. Torimoto, *J. Phys. Chem. Lett.* **2010**, 3177–3188.

[37] T. Torimoto, T. Tsuda, K. Okazaki, S. Kuwabata, *Adv. Mater.* **2010**, *22*, 1196–1221.

[38] Z. Ma, J. Yu, S. Dai, *Adv. Mater.* **2010**, *22*, 261–285.

[39] H. Wang, G. Gurau, R. D. Rogers, *Chem. Soc. Rev.* **2012**, *41*, 1519–1537.

[40] X. Sun, H. Luo, S. Dai, *Chem. Rev.* **2012**, *112*, 2100–2128.

[41] T. Tsuda, C. L. Hussey, *Modern Aspects of Electrochemistry, Vol 45*; (Ed.: R. E. White). **2009**, springer Science+Bussiness Media: New York, p. 63.

[42] J. Dupont, G. S. Fonseca, A. P. Umpierre, P. F. P. Fichtner, S. R. Teixeira, *J. Am. Chem. Soc.* **2002**, *124*, 4228–4229.

[43] F. Endres, S. Zein El Abedin, *Phys. Chem. Chem. Phys.* **2002**, *4*, 1640–1648.

[44] E. F. Smith, I. J. V. Garcia, D. Briggs, P. Licence, *Chem. Commun.* **2005**, 5633–5635.

[45] S. Kuwabata, A. Kongkanand, D. Oyamatsu, T. Torimoto, *Chem. Lett.* **2006**, *35*, 600–601.

[46] S. Arimoto, H. Kageyama, T. Torimoto, S. Kuwabata, *Electrochem. Commun.* **2008**, *10*, 1901–1904.

[47] S. Arimoto, M. Sugimura, H. Kageyama, T. Torimoto, S. Kuwabata, *Electrochim. Acta* **2008**, *53*, 6228–6234.

[48] T. Torimoto, K. Okazaki, T. Kiyama, K. Hirahara, N. Tanaka, S. Kuwabata, *Appl. Phys. Lett.* **2006**, *89*, 243117.

[49] K. Okazaki, T. Kiyama, K. Hirahara, N. Tanaka, S. Kuwabata, T. Torimoto, *Chem. Commun.* **2008**, 691–693.

[50] O. P. Khatri, K. Adachi, K. Murase, K. Okazaki, T. Torimoto, N. Tanaka, S. Kuwabata, H. Sugimura, *Langmuir* **2008**, *24*, 7785–7792.

[51] K. Okazaki, T. Kiyama, T. Suzuki, S. Kuwabata, T. Torimoto, *Chem. Lett.* **2009**, *38*, 330–331.

[52] T. Suzuki, K. Okazaki, T. Kiyama, S. Kuwabata, T. Torimoto, *Electrochemistry* **2009**, 636–638.

[53] S. K. T. Tsuda, T. Kurihara, Y. Hoshino, T. Kiyama, K.-I . Okazaki, T. Torimoto, *Electrochemistry* **2009**, *77*, 693–695.

[54] T. Suzuki, K. Okazaki, S. Suzuki, T. Shibayama, S. Kuwabata, T. Torimoto, *Chem. Mater.* **2010**, 22, 5209-5215.

[55] T. Suzuki, S. Suzuki, Y. Tomita, K. Okazaki, T. Shibayama, S. Kuwabata, T. Torimoto, *Chem. Lett.* **2010**, *39*, 1072–1074.

[56] Y. Oda, K. Hirano, K. Yoshii, S. Kuwabata, T. Torimoto, M. Miura, *Chem. Lett.* **2010**, *39*, 1069–1071.

[57] S. Suzuki, Y. Ohta, T. Kurimoto, S. Kuwabata, T. Torimoto, *Phys. Chem. Chem. Phys.* **2011**, *13*, 13585–13593.

[58] S. Suzuki, T. Suzuki, Y. Tomita, M. Hirano, K. Okazaki, S. Kuwabata, T. Torimoto, *CrystEngComm* **2012**, *14*, 4922-4926.

[59] M. Hirano, K. Enokida, K. Okazaki, S. Kuwabata, H. Yoshida, T. Torimoto, *Phys. Chem. Chem. Phys.* **2013**, *15*, 7286–7294.

[60] Y. Hatakeyama, M. Okamoto, T. Torimoto, S. Kuwabata, K. Nishikawa, *J. Phys. Chem. C* **2009**, *113*, 3917–3922.

[61] Y. Hatakeyama, S. Takahashi, K. Nishikawa, *J. Phys. Chem. C* **2010**, *114*, 206–237.

[62] Y. Hatakeyama, K. Onishi, K. Nishikawa, *RSC Adv.* **2011**, *1*, 1815–1821.

[63] T. Iimori, Y. Hatakeyama, K. Nishikawa, M. Kato, N. Ohta, *Chem. Phys. Lett.* **2013**, *586*, 100–103.

[64] H. Wender, L. F. de Oliveira, P. Migowski, A. F. Feil, E. Lissner, M. H. G. Prechtl, S. R. Teixeira, J. Dupont, *J. Phys. Chem. C* **2010**, *114*, 11764–11768.

[65] H. Wender, P. Migowski, A. F. Feil, L. F. de Oliveira, M. H. G. Prechtl, R. Leal, G. Machado, S. R. Teixeira, J. Dupont, *Phys. Chem. Chem. Phys.* **2011**, *13*, 13552–13557.

[66] R. E. Del Sesto, C. Corley, A. Robertson, J. S. Wilkes, *J. Organomet. Chem.* **2005**, *690*, 2536–2542.

[67] C. J. Bradaric, A. Downard, C. Kennedy, A. J. Robertson, Y. Zhou, *Green Chem.* **2003**, *5*, 143–152.

[68] K. J. Fraser, E. I. Izgorodina, M. Forsyth, J. L. Scott, D. R. MacFarlane, *Chem. Commun.* **2007**, 3817–3819.

[69] M. D. Green, C. Schreiner, T. E. Long, *J. Phys. Chem. A* **2011**, *115*, 13829–13835.

[70] K. Fukumoto, H. Ohno, *Angew. Chem. Int. Ed.* **2007**, *46*, 1852–1855.

[71] Y. Tsuji, H. Ohno, *RSC Adv.* **2012**, *2*, 11279–11284.

[72] V. Armel, D. Velayutham, J. Sun, P. C. Howlett, M. Forsyth, D. R. MacFarlane, J. M. Pringle, *J. Mater. Chem.* **2011**, *21*, 7640–7650.

[73] L. Jin, K. M. Nairn, C. M. Forsyth, A. J. Seeber, D. R. MacFarlane, P. C. Howlett, M. Forsyth, J. M. Pringle, *J. Am. Chem. Soc.* **2012**, *134*, 9688–9697.

[74] K. Tsunashima, M. Sugiya, *Electrochemistry* **2007**, *75*, 734–736.

[75] K. Tsunashima, M. Sugiya, *Electrochem. Commun.* **2007**, *9*, 2353–2358.

[76] K. Tsunashima, E. Niwa, S. Kodama, M. Sugiya, Y. Ono, *J. Phys. Chem. B* **2009**, *113*, 15870–15874.

[77] K. Tsunashima, S. Kodama, M. Sugiya, Y. Kunugi, *Electrochim. Acta* **2010**, *56*, 762–766.

[78] K. Tsunashima, Y. Ono, M. Sugiya, *Electrochim. Acta* **2011**, *56*, 4351–4355.

[79] K. Tsunashima, A. Kawabata, M. Matsumiya, S. Kodama, R. Enomoto, M. Sugiya, Y. Kunugi, *Electrochem. Commun.* **2011**, *13*, 178–181.

[80] T. Enomoto, S. Kanematsu, K. Tsunashima, K. Matsumoto, R. Hagiwara, *Phys. Chem. Chem. Phys.* **2011**, *13*, 12536–12544.

[81] S. Kanematsu, K. Matsumoto, R. Hagiwara, *Electrochem. commun.* **2009**, *11*, 1312–1315.

[82] E. Redel, R. Thomann, C. Janiak, *Inorg. Chem.* **2008**, *47*, 14–16.

[83] J. A. Lazzús, *Fluid Phase Equilib.* **2012**, *313*, 1–6.

[84] T. J. Wooster, K. M. Johanson, K. J. Fraser, D. R. MacFarlane, J. L. Scott, *Green Chem.* **2006**, *8*, 691–696.

[85] H. Luo, G. a Baker, J. S. Lee, R. M. Pagni, S. Dai, *J. Phys. Chem. B* **2009**, *113*, 4181–4183.

[86] D. R. MacFarlane, P. Meakin, J. Sun, N. Amini, M. Forsyth, *J. Phys. Chem. B* **1999**, *103*, 4164–4170.

[87] Z.-B. Zhou, H. Matsumoto, *Electrochem. commun.* **2007**, *9*, 1017–1022.

[88] R. Taniki, K. Matsumoto, R. Hagiwara, K. Hachiya, T. Morinaga, T. Sato, *J. Phys. Chem. B* **2013**, *117*, 955–960.

[89] J. Timmermans, *J. Phys. Chem. Solids* **1961**, *18*, 1–8.

[90] Y. Abu-Lebdeh, A. Abouimrane, P.-J. Alarco, M. Armand, *J. Power Sources* **2006**, *154*, 255–261.

[91] Z. B. Zhou, H. Matsumoto, K. Tatsumi, *Chem. Eur. J.* **2006**, *12*, 2196–2212.

[92] J. Golding, S. Forsyth, D. R. MacFarlane, M. Forsyth, G. B. Deacon., *Green Chem.* **2002**, *4*, 223–229.

[93] M. J. Frisch, *et al. Gaussian 09*, Revision A. 02; Gasussian, Inc.; Wallingford, CT, 2009.

[94] H. D. B. Jenkins, H. K. Roobottom, J. Passmore, L. Glasser, *Inorg. Chem.* **1999**, *38*, 3609–3620.

[95] I. Krossing, J. M. Slattery, C. Daguenet, P. J. Dyson, A. Oleinikova, H. Weingärtner, *J. Am. Chem. Soc.* **2006**, *128*, 13427–13434.

[96] J. M. Slattery, C. Daguenet, P. J. Dyson, T. J. S. Schubert, I. Krossing, *Angew. Chem. Int. Ed.* **2007**, *46*, 5384–5388.

[97] N. V. Novozhilova, N. S. Magomedova, A. N. Sobolev, V. K. Bel'skii, *J. Struct. Chem.* **1989**, *30*, 515–518.

[98] D. Sun, R. Cao, Y. Sun, X. Li, W. Bi, M. Hong, Y. Zhao, *Eur. J. Inorg. Chem.* **2003**, *2003*, 94–98.

[99] C. A. Angell, C. T. Moynihan, *Molten Salts Characterization and Analysis*, Marcel Dekker, New York, **1969**, p. 315.

[100] C. A. Angell, *J. Phys. Chem.* **1964**, *68*, 1917–1929.

[101] C. T. Moynihan, C. A. Angell, *J. Phys. Chem.* **1970**, *74*, 736–742.

[102] T. Tsuda, K. Kondo, M. Baba, S. Suwa, Y. Ikeda, T. Sakamoto, S. Seino, H. Yoshida, M. Ozaki, A. Imanishi, et al., *Electrochim. Acta* **2013**, *100*, 285–292.

[103] P.-Y. Chen, C. L. Hussey, *Electrochim. Acta* **2004**, *49*, 5125–5138.

[104] T. Tsuda, L. E. Boyd, S. Kuwabata, C. L. Hussey, *J. Electrochem. Soc.* **2010**, *157*, F96-F103.

[105] H. Tokuda, K. Hayamizu, K. Ishii, M. A. B. H. Susan, M. Watanabe, *J. Phys. Chem. B* **2004**, *108*, 16593–16600.

[106] W. Xu, E. I. Cooper, C. A. Angell, *J. Phys. Chem. B* **2003**, *107*, 6170–6178.

[107] D. R. MacFarlane, M. Forsyth, E. I. Izgorodina, A. P. Abbott, G. Annat, K. Fraser, *Phys. Chem. Chem. Phys.* **2009**, *11*, 4962–4967.

[108] H. Matsumoto, M. Yanagida, K. Tanimoto, M. Nomura, Y. Kitagawa, Y. Miyazaki, *Chem. Lett.* **2000**, 922–923.

[109] J. Crosthwaite, M. Muldoon, J. Dixon, J. Anderson, J. Brennecke, *J. Chem. Thermodyn.* **2005**, *37*, 559–568.

[110] Z. Fei, D. Kuang, D. Zhao, C. Klein, W. H. Ang, S. M. Zakeeruddin, M. M. Grätzel, P. J. Dyson, *Inorg. Chem* **2006**, *45*, 10407–10409.

[111] J. a. Widegren, J. W. Magee, *J. Chem. Eng. Data* **2007**, *52*, 2331–2338.

[112] P. S. Kulkarni, L. C. Branco, J. G. Crespo, M. C. Nunes, A. Raymundo, C. A. M. Afonso, *Chem. Eur. J.* **2007**, *13*, 8478–8488.

[113] S. Zhang, X. Lu, Q. Zhou, X. Li, X. Zhang, S. Li, *Ionic Liquids*, Elsevier, Amsterdam, **2009**.

[114] S. Seki, K. Hayamizu, S. Tsuzuki, K. Fujii, Y. Umebayashi, T. Mitsugi, T. Kobayashi, Y. Ohno, Y. Kobayashi, Y. Mita, et al., *Phys. Chem. Chem. Phys.* **2009**, *11*, 3509–3514.

[115] S. Coleman, R. Byrne, N. Alhashimy, K. J. Fraser, D. R. Macfarlane, D. Diamond, *Phys. Chem. Chem. Phys.* **2010**, *12*, 7009–7017.

[116] A. Orita, K. Kamijima, M. Yoshida, *J. Power Sources* **2010**, *195*, 7471–7479.

[117] K. Nakamura, T. Shikata, *ChemPhysChem* **2010**, *11*, 285–294.

[118] K. Shimizu, M. Tariq, M. F. Costa Gomes, L. P. N. Rebelo, J. N. Canongia Lopes, *J. Phys. Chem. B* **2010**, *114*, 5831–5834.

[119] R. Ren, Y. Zuo, Q. Zhou, H. Zhang, S. Zhang, *J. Chem. Eng. Data* **2011**, *56*, 27–30.

[120] S. Berdzinski, J. Horst, P. Straßburg, V. Strehmel, *ChemPhysChem* **2013**, *14*, 1899–1908.

[121] P. Sigmund, *Phys. Rev.* **1969**, *184*, 383–416.

[122] C. S. Santos, S. Baldelli, *Chem. Soc. Rev.* **2010**, *39*, 2136–2145.

[123] C. Aliaga, G. A. Baker, S. Baldelli, *J. Phys. Chem. B* **2008**, *112*, 1676–1684.

[124] H. Tokuda, K. Hayamizu, K. Ishii, M. A. B. H. Susan, M. Watanabe, *J. Phys. Chem. B* **2005**, *109,* 6103–6110.

[125] H. S. Schrekker, M. A. Gelesky, M. P. Stracke, C. M. L. Schrekker, G. Machado, S. R. Teixeira, J. C. Rubim, J. Dupont, *J. Colloid Interface Sci.* **2007**, *316*, 189–195.

[126] K. R. J. Lovelock, C. Kolbeck, T. Cremer, N. Paape, P. S. Schulz, P. Wasserscheid, F. Maier, H.-P. Steinrück, *J. Phys. Chem. B* **2009**, *113,* 2854–2864.

[127] C. Kolbeck, T. Cremer, K. R. J. Lovelock, N. Paape, P. S. Schulz, P. Wasserscheid, F. Maier, H.-P. Steinrück, *J. Phys. Chem. B* **2009**, *113,* 8682–8688.

[128] Z. W. Zhao, Z. P. Guo, J. Ding, D. Wexler, Z. F. Ma, D. Y. Zhang, H. K. Liu, *Electrochem. Commun.* **2006**, *8*, 245–250.

[129] Z. Wang, Q. Zhang, D. Kuehner, A. Ivaska, L. Niu, *Green Chem.* **2008**, *10*, 907-909.

[130] P. Yu, J. Yan, H. Zhao, L. Su, J. Zhang, L. Mao, *J. Phys. Chem. C* **2008**, *112*, 2177–2182.

[131] F. Li, F. Li, J. Song, J. Song, D. Han, L. Niu, *Electrochem. commun.* **2009**, *11*, 351–354.

[132] B. Wu, D. Hu, Y. Kuang, B. Liu, X. Zhang, J. Chen, *Angew. Chem. Int. Ed.* **2009**, *121*, 4751–4754.

[133] D. Tasis, N. Tagmatarchis, A. Bianco, M. Prato, *Chem. Rev.* **2006**, *106*, 1105–1136.

[134] R. Yu, L. Chen, Q. Liu, J. Lin, K.-L. Tan, S. C. Ng, H. S. O. Chan, G.-Q. Xu, T. S. A. Hor, *Chem. Mater.* **1998**, *10*, 718–722.

[135] M. Okamoto, T. Fujigaya, N. Nakashima, *Small* **2009**, *5*, 735–740.

[136] Y. Takasu, T. Iwazaki, W. Sugimoto, Y. Murakami, *Electrochem. Commun.* **2000**, *2*, 671–674.

[137] T. Kawaguchi, W. Sugimoto, Y. Murakami, Y. Takasu, *Electrochem. Commun.* **2004**, *6*, 480–483.

[138] A. Sarapuu, A. Kasikov, T. Laaksonen, K. Kontturi, K. Tammeveski, *Electrochim. Acta* **2008**, *53*, 5873–5880.

[139] S. Mukerjee, *J. Appl. Electrochem.* **1990**, *20*, 537–548.

[140] E. Higuchi, H. Uchida, M. Watanabe, *J. Electroanal. Chem.* **2005**, *583*, 69–76.

[141] C. W. Scheeren, G. Machado, S. R. Teixeira, J. Morais, J. B. Domingos, J. Dupont, *J. Phys. Chem. B* **2006**, *110*, 13011–13020.

[142] L. S. Ott, M. L. Cline, M. Deetlefs, K. R. Seddon, R. G. Finke, *J. Am. Chem. Soc.* **2005**, *127*, 5758–5759.

[143] L. S. Ott, S. Campbell, K. R. Seddon, R. G. Finke, *Inorg. Chem.* **2007**, *46*, 10335–10344.

[144] R. Atkin, G. G. Warr, *J. Phys. Chem. C* **2007**, *111*, 5162–5168.

[145] R. Hayes, S. Z. El Abedin, R. Atkin, *J. Phys. Chem. B* **2009**, *113*, 7049–7052.

[146] F. Endres, O. Höfft, N. Borisenko, L. H. Gasparotto, A. Prowald, R. Al-Salman, T. Carstens, R. Atkin, A. Bund, S. Z. E. Abedin, *Phys. Chem. Chem. Phys.* **2010**, *12*, 1724–1732.

[147] C. W. Scheeren, G. Machado, S. R. Teixeira, J. Morais, J. B. Domingos, J. Dupont, *J. Phys. Chem. B* **2006**, *110*, 13011–13020.

[148] M. Shigeyasu, H. Murayama, H. Tanaka, *Chem. Phys. Lett.* **2008**, *463*, 373–377.

[149] T. Fukushima, A. Kosaka, Y. Ishimura, T. Yamamoto, T. Takigawa, N. Ishii, T. Aida, *Science.* **2003**, *300*, 2072–2074.

[150] Y. Shim, H. J. Kim, *ACS Nano* **2009**, *3*, 1693–1702.

[151] M. S. Saha, A. Kundu, *J. Power Sources* **2010**, *195*, 6255–6261.

[152] V. Stamenković, T. J. Schmidt, P. N. Ross, N. M. Marković, *J. Phys. Chem. B* **2002**, *106*, 11970–11979.

[153] E. Antolini, *J. Appl. Electrochem.* **2004**, *34*, 563–576.

[154] M. L. Perry, T. F. Fuller, *J. Electrochem. Soc.* **2002**, *149*, S59–S67.

[155] A. Rabis, P. Rodriguez, T. J. Schmidt, *ACS Catal.* **2012**, *2*, 864–890.

[156] X. Yu, S. Ye, *J. Power Sources* **2007**, *172*, 133–144.

[157] L. Roen, C. Paik, T. Jarvi, *Electrochem. Solid-State Lett.* **2004**, *7*, A19–A22.

[158] Y. Shao, G. Yin, Y. Gao, *J. Power Sources* **2007**, *171*, 558–566.

[159] X. Yu, S. Ye, *J. Power Sources* **2007**, *172*, 145–154.

[160] A. P. Young, V. Colbow, D. Harvey, E. Rogers, S. Wessel, *J. Electrochem. Soc.* **2013**, *160*, F381–F388.

[161] C. Reiser, L. Bregoli, T. Patterson, *Electrochem. Solid-State Lett.* **2005**, *8*, A273–A276.

[162] S. Chen, Z. Wei, X. Qi, L. Dong, Y.-G. Guo, L. Wan, Z. Shao, L. Li, *J. Am. Chem. Soc.* **2012**, *134*, 13252–13255.

[163] X. Wang, W. Li, Z. Chen, M. Waje, Y. Yan, *J. Power Sources* **2006**, *158*, 154–159.

[164] A. Kongkanand, K. Vinodgopal, S. Kuwabata, P. V Kamat, *J. Phys. Chem. B* **2006**, *110*, 16185–16188.

[165] B. Y. Xia, J. N. Wang, S. J. Teng, X. X. Wang, *Chemistry* **2010**, *16*, 8268–8274.

[166] S. Guo, S. Sun, *J. Am. Chem. Soc.* **2012**, *134*, 2492–2495.

[167] Y. Li, Y. Li, E. Zhu, T. McLouth, C.-Y. Chiu, X. Huang, Y. Huang, *J. Am. Chem. Soc.* **2012**, *134*, 12326–12329.

[168] X. Zhao, A. Hayashi, Z. Noda, K. Kimijima, I. Yagi, K. Sasaki, *Electrochim. Acta* **2013**, *97*, 33–41.

[169] H. Yano, T. Akiyama, M. Watanabe, H. Uchida, *J. Electroanal. Chem.* **2013**, *688*, 137–142.

[170] Fuel Cell Commerciallization Conference of Japan (FCCJ), Proposals of the development targets, research and development challenges and evaluation methods concerning PEFC, http://www.fccj.jp/pdf/23.01.kt.pdf

[171] K. H. Kangasniemi, D. A. Condit, T. D. Jarvi, *J. Electrochem. Soc.* **2004**, *151*, E125–E132.

Acknowledgement

First of all, the author would like to express his sincerest gratitude to Prof. Dr. Susumu Kuwabata, Department of Applied Chemistry, Graduate School of Engineering, Osaka University, for his continuous guidance, invaluable suggestions, and encouragement throughout the course of thesis.

The author would also like to thank to Prof. Dr. Ken-ichi Machida and Prof. Dr. Nobuhito Imanaka, Department of Applied Chemistry, Graduate School of Engineering, Osaka University, for their helpful comments and suggestion.

The author would like to express his special thanks to Associate Prof. Dr. Tetsuya Tsuda, Department of Applied Chemistry, Graduate School of Engineering, Osaka University, for his continuous guidance throughout these works, many helpful suggestion and fruitful discussion.

The author would like to express his special thanks to Assistant Prof. Dr. Taro Uematsu, Department of Applied Chemistry, Graduate School of Engineering, Osaka University, for helpful advices and fruitful discussion.

The author would like to express his special thanks to Dr. Eiko Mochizuki, Department of Applied Chemistry, Graduate School of Engineering, Osaka University, for her hearty encouragement and grateful help throughout the life in the laboratory.

The author would like to express his thanks to Prof. Dr. Tsukasa Torimoto, Department of Crystalline Materials Science, Graduate School of Engineering, Nagoya University, for expert comment and experimental help

The author would like to express his thanks to Associate Prof. Dr. Akihito Imanishi and Mr. Takashi Arimura, Department of Chemistry, Graduate School of Engineering Science, Osaka University, for the measurements of XPS and fruitful discussion.

The author would like to express his thanks to Associate Prof. Dr. Katsuhiko Tsunashima,

Department of Material Science, Wakayama National College of Technology, for the proffer of phosphonium cation-based RTILs and fruitful discussion.

The author would like to express his thanks to Prof. Dr. Mitsuru Akashi and Dr. Masahiro Matsumoto, Department of Applied Chemistry, Graduate School of Engineering, Osaka University, for the measurements of Reflective FT-IR spectra.

The author would like to express his thanks to Dr. Kyoko Inoue, Laboratory for Instrumental Analysis, Graduate School of Engineering, Osaka University, for the NMR experiments.

The author is grateful for financial support by the Japan Society of the Promotion Science (JSPS) and Global Center of Excellence (GCOE) program “Global Education and Research Center for Bio-Environmental Chemistry” of Osaka University.

The author is grateful acknowledgements to Mrs. Chia-Fen Tsai, Mr. Masakatsu Kawanabta, and Mr. Keisuke Yamaji for their active collaboration in the course of experiments.

The author is deeply indebted to Mr. Koshi Kawakami, Mr. Koshiro Kondo and Mr. Taiki Sakamoto as colleagues for the master’s course. The author is also grateful to Dr. Hiroshi Aoki, Dr. Dai Shirotani, Mrs. Shoko Kishida, Mr. Shigeo Maeda, Mr. Hiroshi Tenmyo, Dr. Shohei Taniguchi, Mr. Kosuke Inoue, Mr. Toshihiro Doi, Mr. Takahisa Higuchi, Mr. Satoshi Makuta, Mr. Hiro Minamimoto, Mr. Yuichi Ikeda, Mr. Akihisa Doko, Mr. Yoshitomo Nishimura, Mr. Jun-Tae Han, Mr. Rentaro Sakao, Mr. Yusuke Kaji, Mr. Tsukasa Kanetsuku, Mr. Masahiro Baba, Mr. Yuki Iwasaki, Mr. Masami Sasatani, Mr. Haruki Narikawa, Mr. Shotaro Suwa, Mr. Tomoki Tsumadori, Mr. Taisuke Asano, Mr. Kazuki Iwasaki, Mr. Itsuki Kokubo, Mr. Tsuyoshi Sakamoto, Mr. Ryota Yasutake, Mr. Haruyasu Irie, Mr. Sayaki Umemoto, Mr. Akihiro Konda, Mr. Teruki Sano, Mr. Eisuke Shimomura and all other

member of the laboratory of Prof. Susumu Kuwabata for hearty support and precious memories.

Finally, the author wishes to express his sincerest gratitude to his parents, Akimasa Yoshii and Yoko Yoshii, his younger brother, Takanori Yoshii, and his grandparents, Hiromu Yoshii and the late Michiyo Yoshii for their hearty encouragements and supports.

January 2014

Kazuki Yoshii